Investigation of Charge Carrier Dynamics in Novel Photovoltaic Materials

Hannes Hempel

2019

im Fachbereich Physik der Freien Universität Berlin eingereichte Dissertation

zur Erlangung des Dr. rer. nat.

Erstgutachter: Prof. Dr. Klaus Lips

Zweitgutachter: Prof. Dr. Tobias Kampfrath

Tag der Disputation: 15.01.2020

Table of Contents

1 Introduction: State of Photovoltaic Research

Photovoltaics is one of the keys to ecological, sustainable and decentralized power production.

Currently, silicon solar cells are close to achieving this goal as their levelized cost of electricity is competitive with conventional techniques of power generation. The 2018 photovoltaics report from the Fraunhofer Institute for Solar Energy Systems on the levelized cost of electricity shows that the cost of photovoltaic of 3.7-11.5 $€_{Cent}$/kWh is comparable with the cost for coal of 4.6-8.0 $€_{Cent}$/kWh, for gas of 7.8-10.0 $€_{Cent}$/kWh and for wind of 4.0-8.2 $€_{Cent}$/kWh even in a country with moderate sun irradiation as Germany. Therefore, photovoltaics are not only ecologically but also economically of large interest and the market volume reached 34 billion $ already in 2013.

Currently, silicon-based solar cells hold an overwhelming share in the photovoltaic market and have undergone an impressive drop in production costs in the past years. However, there are strong reasons, for which novel photovoltaic materials will finally beat the production cost of the silicon photovoltaics.

Firstly, silicon technology has a relatively large material usage. The silicon wafers are typically 100s of micrometer thick because of their relatively low and indirect light absorption as well as due to the wafer-cutting process. In contrast, direct semiconductors can be fabricated as thin films with a typical thickness of 1 µm and still absorb light equally well as silicon.

Secondly, the growth of silicon wafers consumes relatively much energy as the process requires the melting of silicon at temperatures above 1425 °C. Lower processing temperatures of alternative materials could lower production costs significantly. Such lower processing temperatures also would allow for new deposition techniques as ink printing and would allow full integration into roofing or on flexible substrates.

These issues with the silicon technology can (and partially have been) overcome by thin-film solar cells based on $Cu(In,Ga)(S,Se)_2$ and CdTe, which are commercially successful. They have achieved energy payback times of ca. 0.7 years for CdTe, which is significantly shorter than ca. 1.8 years for monocrystalline silicon [1]. On the downside, thin-film solar cells have their own drawbacks. For example, they are comprised of rare and toxic elements and have not reached the efficiencies of silicon solar cells jet. The deficiency in their power conversion efficiency may be overcome someday, but they will still face the issue of the abundance and toxicity of their constituting elements, which is of no concern for silicon. These drawbacks are one of the reasons for the decrease in the share of $Cu(In,Ga)(S,Se)_2$ and CdTe in the photovoltaic market from 17 % in 2009 to 5 % in 2017.

Also, other evolving shooting stars in photovoltaics, such as the lead-containing perovskites, face stability and toxicity issues and have not proven to be commercially successful.

Therefore, the endeavor to find the ideal photovoltaic material is still ongoing. Such ideal material should combine the non-toxicity and abundance of silicon, the simple synthesis and defect tolerance of hybrid perovskites and the high power conversion efficiency of gallium arsenide solar cells.

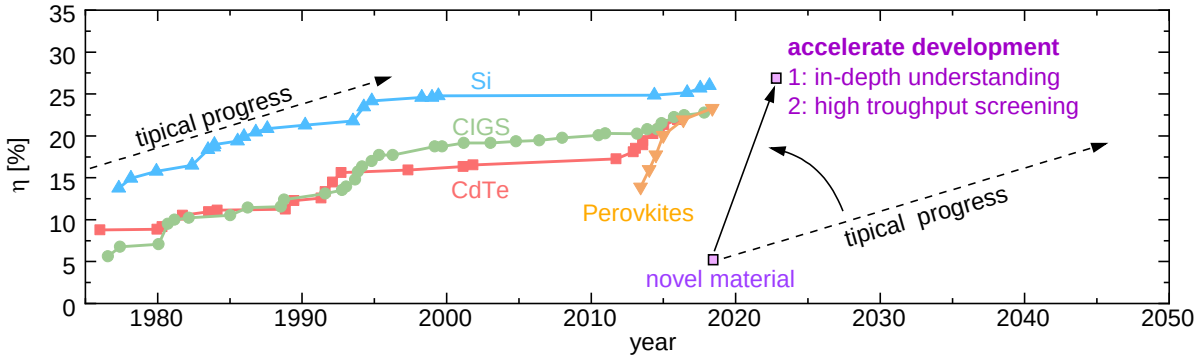

Figure 1.1 Record efficiencies of emerging photovoltaic materials. *The power conversion efficiency of the market-leading silicon photovoltaics and the main thin-film competitors (CdTe and CIGS) increased constantly but slowly over the decades. The novel materials as perovskites are developed much more rapidly and set the benchmark for development times in other novel photovoltaic materials. (Data adapted from the NREL efficiency chart.)*

However, it took Si, CdTe and Cu (In,Ga)(S,Se)$_2$ decades to reach their current efficiencies and these are still increasing further as shown in Figure 1.1. Such long development times are not feasible for novel photovoltaic materials. This situation is illustrated in Figure 1.1, in which the development of the efficiency of a novel material is extrapolated by the typical progress rate. In such a scenario the material would reach the current efficiency level of silicon in 2050. Therefore, the development of novel photovoltaic material has to be accelerated significantly. The rapid rise of halide-perovskite solar cells shows in Figure 1.1 that the learning curve in photovoltaic research becomes steeper and sets the benchmark for the development of novel photovoltaic materials.

Ideally, a novel material does not have to be processed into a solar cell. Instead, the bare absorber material should be probed contactless for key properties that predict its potential for photovoltaic application and guide its further engineering. The realization of this vision is the guideline for the presented work, which is structured as follows:

The theory of charge carrier dynamics will be introduced in Chapter 2 based on textbook physics and it will be the fundament for the interpretation of charge carrier dynamics that are measured in Chapter 6. It describes the energetic and spatial distribution of (photo-excited) charge carriers and their kinetics by a few key properties.

The key properties of photovoltaic materials are introduced in Chapter 3 to model the performance of such a material in a solar cell. To this end, two paths are followed: Firstly, the description by external properties that lead to the so-called “Shockley-Queisser limit” and it generalizations. Secondly, the description by internal properties that allow more complex modeling [2]. This theory will be applied in Chapter 7.

Two of these internal properties – the mobility and lifetime of charge carriers - can both be measured contactless by Time-Resolved Terahertz Spectroscopy (TRTS), which will be described in detail in Chapter 4. This chapter is intended to serve future doctoral researchers as tutorial and manual. Therefore, it explains in detail the TRTS setup, the calibration of the measurements, the analysis methods and the differences compared to alternative characterization techniques.

Following that, my scientific contributions as first author [3] [4] [5] [6], coauthor [7] [8] [9] [10] [11] [12] [13] [14] [15] [16] [17] [18] and unpublished supplementing work are arranged in three topics, which are the validation of TRTS on photovoltaic samples, the in-depth characterization of a $Cu_2ZnSnSe_4$ thin film and the estimation of its photovoltaic performance.

In Chapter 5 the TRTS method is validated on photovoltaic samples because TRTS is a relatively seldom used method by the photovoltaic community and sometimes meets reservations. Therefore, it will be shown that TRTS yields consistent results for different analysis and measurement modes; as well as for different sample geometries. In particular, it will be shown that TRTS can measure charge carrier mobilities in thin films on metal substrates, which is the common sample architecture for photovoltaic materials [3]. The relevance of the TRTS derived results will be further supported by comparison with alternative techniques that also derive charge carrier transients and mobilities.

The in-depth characterization of charge carrier dynamics is performed in Chapter 6 on a $Cu_2ZnSnSe_4$ kesterite-type thin film, which lead to several first-author publications [4] [5] [6] and co-author publications [18] [15]. This thin film was deposited by the group of Ingrid Repins during my stay at the national renewable energy laboratory (NREL) in the USA at conditions that lead to their certified record efficiency of 9.8 % for a $Cu_2ZnSnSe_4$ solar cell [19]. However, this record efficiency stagnated for the last years, which is often attributed to a fundamental limitation of kesterite solar cells by band tails. Here, this attribution and impact of band tails are probed by several complementary techniques. First, the well-studied absorption tails are shown. Then the ultrafast dynamics of photo-excited charge carriers are revealed including cooling, band tail trapping, localization and the transition from bipolar to ambipolar transport. Afterward, the dominant recombination channels and the limitations of charge transport on the nm-scale are identified [4] [5]. Thereby, the individual charge carrier mobilities of

electrons and holes are derived [5]. Additionally, the impact of the Cu-Zn disorder, which is a potential origin of the band tails in $Cu_2ZnSnSe_4$, on the charge carrier dynamics is probed [6].

In Chapter 7 these complex charge carrier dynamics in the thin film are compressed into a few key properties to estimate the performance of such a thin film in a finished solar cell. This estimation is compared to results derived by quantitative photoluminescence, by the Shockley-Queisser limit and to the performance of the finished solar cell. Thereby the loss due to the occupation of band tails is identified and compared to loss by non-radiative recombination.

2 The Theory of Charge Carrier Dynamics

The theory of charge carrier dynamics describes the energetic (section 2.1) and spatial (section 2.2) distribution of charge carriers as well as their kinetics. To this end, the dynamics in generation, recombination (section 2.3), and transport (section 2.4) of charge carriers are introduced.

This theory chapter is mostly based on textbook physics [20] [21]. It is the basis to interpret the frequency-depend charge carrier mobility and the photoconductivity transients which are measured in this work.

2.1 Energetic Distribution of Charge Carriers

The properties of a charge carrier depend on the states they occupy. Therefore, it is crucial to describe the distribution of charge carriers over the density of electronic states in a material.

Photovoltaic materials are semiconductors and the relevant states for charge carrier dynamics are the valance band, which is the highest completely occupied band at zero kelvin, and the conduction band, which is the lowest unoccupied band at zero kelvin. These bands are often described by parabolic dispersion relation between momentum k and energy $E(k) = \hbar^2k^2/(2m_{eff})$. Such a dispersion is an analog to the kinetic energy of free electrons but with an effective mass m_{eff} which differs from the free electron mass. It results in 3D in the following density of states (DOS) for the conduction band with an effective mass m_c (analogous for the valence band with an individual effective mass m_v):

$$DOS_C(E) \approx \frac{1}{2\pi^2}\left(\frac{2m_c}{\hbar^2}\right)\sqrt{E - E_C} \tag{2.1}$$

Additionally, defect states in the bandgap are important for the charge carrier dynamics in semiconductors. In low concentration, these defect states have discrete levels, but at higher concentrations, the levels broaden and form bands.

The density of states is occupied by electrons. An empty state can also be described as positively charge pseudo-particles, called “holes”. The energetic distribution of electrons $n(E)$ and of holes $p(E)$ are given by the occupation f of the density of states DOS in Equation (2.3). Electrons and holes are fermions and therefore obey the Fermi-Dirac occupation f, which is stated in Equation (2.2) for electrons f_e. For holes $f_h = 1 - f_e$ applies. Such an occupation is determined by the Fermi-level E_F and the temperature of the charge carriers T. For energies larger than approximately E_F+3k_BT, the Boltzmann approximation in the last part of Equation (2.2) can be used.

$$f_e(E) = \frac{1}{1 + exp\left(\frac{E - E_{Fe}}{k_BT}\right)} \approx exp\left(\frac{E_{Fe} - E}{k_BT}\right) \tag{2.2}$$

The concentration of electrons or holes in a certain band (or on a defect level) are given by the energy integral over the charge carrier distribution *n(E)* which occupies these specific states. Usually, the concentrations of electrons *n* and of holes *p* refer to their concentrations in the conduction band and in the valence band, respectively.

$$n(E) = f(E)DOS(E) \qquad n = \int n(E)dE \tag{2.3}$$

In the Boltzmann approximation, the charge carrier concentrations in the conduction band and valence band can be stated in equations (2.4-7) with respect to an effective density of states for electrons N_C and holes N_V.

$$n = N_C exp\left(\frac{E_{Fn} - E_C}{k_B T}\right) \tag{2.4}$$

$$p = N_V exp\left(\frac{E_V - E_{Fp}}{k_B T}\right) \tag{2.5}$$

$$N_C = \int exp\left(\frac{E_C - E}{k_B T}\right) DOS(E)dE = 2\left(\frac{2\pi m_c^* k_B T}{h^2}\right)^{3/2} \tag{2.6}$$

$$N_V = \int exp\left(\frac{E - E_V}{k_B T}\right) DOS(E)dE = 2\left(\frac{2\pi m_v^* k_B T}{h^2}\right)^{3/2} \tag{2.7}$$

At zero kelvin states below the Fermi level are completely occupied and unoccupied above. For higher temperatures, electrons are activated from states below the Fermi level to energetically higher states. Such activation across the band gap is relatively unlikely. Therefore, the carrier concentrations in the bands are usually dominated by the activation of charge carriers from defects in the bandgap that are relatively close to the band edges. Such defects are called donors for electrons that are activated into the conduction band and acceptors for holes that are activated into the valence band. The concentration of the activated charge carriers will be called “doping concentration” here and equals the concentration of the ionized donors or acceptors. It differs in general from the total concentration of the donors and acceptors N_D and N_A, which are usually only partially ionized.

For thermal excitation only, the electron and hole concentrations in the complete density of states is described by Equation (2.2) with the same Fermi level. However, after excitation of additional charge carriers by photo-excitation or injection, the Fermi levels for charge carriers in the conduction band and in the valence differ. The total concentrations n and p in a certain band is given in Equation (2.8)

by the dark carrier concentration n_0 and p_0 and the excited carrier concentration Δn and Δp. Semiconductors with an electron doping of the conduction band is called “n-type” and with a hole doping of the valence band is called “p-type”. In the following the equations will be stated for a p-type semiconductor and can be translated to n-type by interchanging the “p” and “n” labels. Further, it should be noted that equations will be stated preferentially with the hole concentration *p* to avoid the usage of the label “*n*” that will be also used for the refractive index.

$$p = \Delta p + p_0 \tag{2.8}$$

2.2 Spatial Distribution of Charge Carriers

The spatial distribution of a charge carrier concentration is determined by the interplay of charge carrier generation, transport, and recombination. These processes are connected by a continuity equation, which is stated in Equation (2.9) for electrons and can be stated analogous for holes. In general, the charge carrier concentration in each band or defect level is described by an individual continuity equation.

$$\frac{dn}{dt} = G_p - R_p - \frac{1}{q}\frac{dI_p}{dx} \tag{2.9}$$

To evaluate the spatial distribution of the charge carrier concentration *dn(x,t)* from the continuity equation the generation rate *G*, the recombination rate *R* and the charge carrier current *I* have to be determined.

The charge carrier generation rate *G* by photo-excitation is described by Lambert-Beers law in Equation (2.10). The photon flux θ_{ph} is absorbed with an absorption coefficient α and each absorbed photon generates pairs of electrons and holes. Therefore, the generation rate *G* decreases exponentially into the sample.

$$G(x) = \theta_{ph}\alpha exp(-\alpha x) \tag{2.10}$$

The charge carrier transport is caused by two processes which add up in Equation (2.11) to the total charge carrier current *I*. The first process is the drift of charge carriers in an electric field *E*, which is described in Ohm’s law by the mobility μ. The second process is the diffusion of charge carriers into regions of lower charge carrier concentration, which is described in Fick’s law with a diffusion coefficient D_n.

$$I = I_{diff} + I_{drift} = -qD_p\frac{dp}{dx} - q\mu pE \tag{2.11}$$

However, both processes can be characterized by the charge carrier mobility because the diffusion coefficient *D* is connected by the Einstein relation (2.12) to the charge carrier mobility μ.

$$D_p = \frac{k_B T}{e} \mu_p \tag{2.12}$$

The electric field *E = -dV/dx* which causes the drift current originates from an electrical potential *V*. This potential can be caused by external fields (for example a terahertz pulse), by the band edge energy of the respective band (for example band edge fluctuations or gradients) and by internal charges.

The electric potential from an internal charge distribution *ρ(x)* can be derived from the Poisson Equation (2.13). Such a charge distribution includes the distribution of lattice charges as ionized donors N_D^+ and acceptors N_A^-, the charges at the surfaces or interfaces and the charges of the electron *n(x)* and hole *p(x)* distributions.

$$\frac{d^2V}{dx^2} = -\rho = e(p - n + N_D^+ - + N_A^-) \tag{2.13}$$

Such a general description of the charge carrier dynamics can usually be simplified by several approximations to model charge carrier dynamics.

First, usually only the electrons in the conduction band and the holes in the valence band are regarded, which limits the number of continuity equation to two. Defect levels, defect bands or band tails are usually only implicitly included by an effective recombination rate and an effective charge carrier mobility, which will be discussed in the next sections. Examples for such models are Shockley-Read-Hall recombination through a defect level or multiple-trapping in a distribution of defects or band tails.

Second, space charges are often neglected for the un-excited sample and it is assumed that the charge distributions of the ionized donors and acceptors and the doping concentration of the charge carriers compensate each other. Therefore only the photo-excited charge carrier concentrations *Δn* and *Δp* have to be regarded in the Poisson equation.

$$\frac{d\Delta p}{dt} = G - R + D_{am} \frac{d\Delta p}{dx} \tag{2.14}$$

Third, often it is assumed that excited electrons and excited holes have the same distribution *Δn(x) = Δp(x)*, which reduces the modeling to a single ambipolar continuity Equation (2.14). Initially, electrons and holes are photo-excited at the same position and the equality of their distributions is obvious. After excitation, they will start to diffuse apart as electrons and holes usually have different mobilities. During this process, a polarization and subsequently an electrostatic potential and a coulomb force build-up. This Coulomb attraction between the electron distribution and hole distribution forces them back together. In consequence, the separation of electron and hole distribution is very small and in approximation, the same distributions *Δn(x) = Δp(x)* can be used for excited electrons and holes. This distribution diffuses with a common ambipolar diffusion coefficient which is given by Equation (2.15).

$$D_{am}(\Delta p) = \frac{k_B T}{e}\mu_{am} = \frac{k_B T}{e}\frac{2\Delta p + p_0}{\frac{\Delta p}{\mu_p} + \frac{\Delta p + p_0}{\mu_n}} \tag{2.15}$$

2.3 Charge Carrier Recombination

Charge carrier recombination is usually classified into bulk vs. surface recombination and by the order of its dependence on the charge carrier concentration, which is illustrated in Figure 2.1. The total recombination rate is given by the sum of the individual recombination channels.

During recombination, an electron relaxes from the conduction band into the valence band and recombines with a hole. During this process, it has to dissipate its energy and can transfers it to photons, phonons or other electrons/ holes.

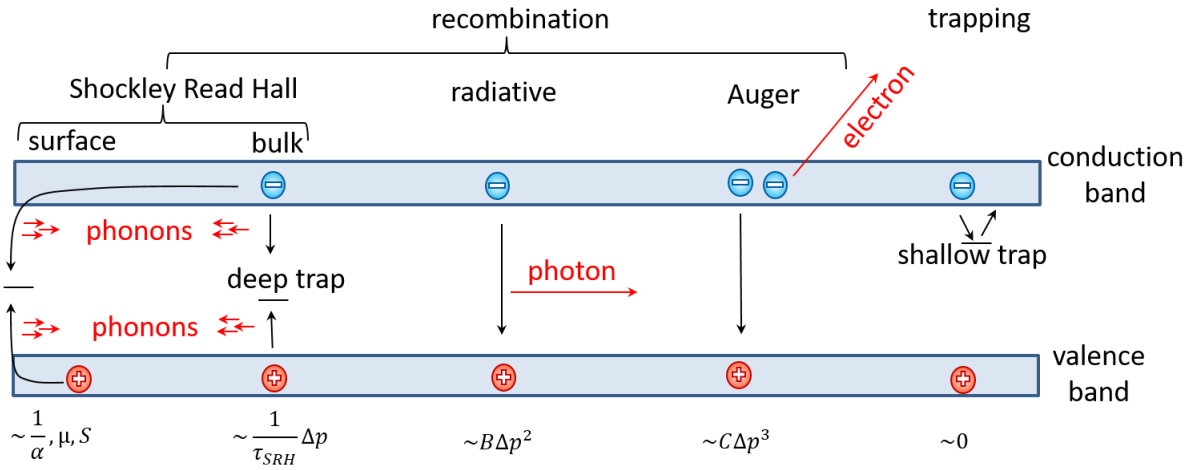

Figure 2.1: Recombination channels. *The recombination of an excited electron and hole pair involves either the emission of phonons (Shockley-Read-Hall recombination) or of photons (radiative recombination) or of charge carriers (Auger recombination). It can be further classified into bulk and surface recombination. A special case are shallow traps that do not allow recombination but release the charge carrier back into the band state.*

The recombination via the emission of phonons (lattice vibrations) dominates for low and moderate excitation levels in most semiconductors. Such lattice vibrations typically have an energy of tens of meV. If the excited electron-hole pair is separated by the bandgap energy of typically ~1eV, multiple phonons have to be emitted simultaneously and the recombination via such a many-body-process is relatively unlikely and slow.

However, if a defect causes a state with a trap level in the bandgap, then the recombination process splits into two steps: the relaxation from the conduction band into the trap level and from the trap level into the valence band. The number of emitted phonons for the individual sub-transitions is smaller than for direct recombination from the conduction band to the valence band. Therefore, such

traps largely can increase the recombination rate if they are situated close to the center of the bandgap.

2.3.1 Deep Traps and Shockley-Read-Hall Recombination

Trap mediated recombination is often described by the Shockley-Read-Hall model [22]. The recombination model established by Shockley, Read and Hall describes the dynamics in a three-level system: conduction band, trap and valence band. Therefore, it regards 4 processes: the relaxation of an electron from the conduction band into the trap, the emission of an electron from the trap back into the conduction band; the relaxation of a hole from the valence band into the trap; and the emission of a hole from the trap back into the valence band.

The Shockley-Read-Hall recombination rate R_{SRH} can be written as the product of an effective charge carrier lifetime τ_{SRH} and the excited charge carrier concentrations Δn and Δp. Therefore, it is in approximation a first-order process, which means that it depends linear on the excited-charge carrier concentration Δp.

$$R_{SRH} = \frac{1}{\tau_{SRH}}\Delta p \qquad with \quad \tau_{SRH}(\Delta n) = \tau_h \frac{\Delta p}{p_0 + p_t + \Delta p} + \tau_e \tag{2.16}$$

However, the effective lifetime can depend on the excited-charge carrier concentration and then the recombination rate will be of a higher order. The effective lifetime is given by the capture times of τ_p of holes and τ_e of electrons for their relaxation into the trap. The parameter p_t in Equation (2.16) connected to the reemission of charge carriers from the trap level and p_0 is the doping (dark carrier) concentration [1].

2.3.2 Surface Recombination

The surface of a semiconductor can be viewed as a huge defect. Often the broken bonds at the surface cause trap levels in the bandgap which increase charge carrier recombination. Such recombination is often described by a surface recombination velocity S. In Equation (2.17), it determines a virtual charge current I_R that flows out of the sample surface and vanishes. As a result, it defines the boundary condition for the continuity equation (2.14).

$$I|_{x=0} = D_{am}\frac{d}{dx}\Delta p|_{x=0} = -S\Delta p \tag{2.17}$$

The surface recombination velocity S_{SHR} can be modeled by SRH recombination, which yields Equation (2.18) and is an analog to the bulk recombination in Equation (2.16).

$$\frac{1}{S(\Delta n)} = \frac{1}{S_h}\frac{\Delta p}{p_0 + p_t{}' + \Delta p} + \frac{1}{S_e} \tag{2.18}$$

2.3.3 Shallow Traps

A trap can have two natures: it may be a deep trap, which increases the recombination rate as discussed by the SRH-model, or it may be a shallow trap, which "temporal imprisons" a charge carrier and releases it back into a state with higher energy in which it can transport or recombine. Charge carriers in shallow traps can in approximation neither transport nor recombine.

Often, shallow traps and the corresponding band states are combined to a common effective density of states which is occupied by a common electron or hole concentration. Then, the average charge carrier mobility μ_{eff} is reduced compared to the mobility μ_{band} of the free charge carriers in the band states by the fraction *x* of charge carriers in the free (band) states [23].

$$\mu_{eff} = \mu_{band} x \tag{2.19}$$

The average lifetime τ_{eff} of all charge carriers is increased by trapping into shallow traps as only the fraction *x* of the charge carrier that are not in the trap can recombine with the lifetime τ_{band} of the free charge carriers in the band states. The free carrier lifetime can, for example, be given the Shockley-Read-Hall lifetime of another trap which is situated in the middle of the bandgap and therefore acts as a recombination center.

$$\tau_{eff} = \frac{\tau_{band}}{x} \tag{2.20}$$

2.3.4 Radiative Recombination

Radiative recombination of an electron and a hole emits a photon. At low photon fluxes, which are common in photovoltaics, spontaneous photon emission dominates. For high photon fluxes as in light-emitting diodes and in particular, in lasers stimulated emission dominates.

The spontaneous radiative recombination rate R_{rad} is given by the radiative coefficient B_{rad} and the electron and hole concentration.

$$R_{rad} = B\Delta p(\Delta p + p_0) \tag{2.21}$$

It depends on the product of the electron and hole concentration as two charge carriers - an electron and a hole - are involved in the recombination process. The minority charge carrier concentration is usually dominated by the photo-excited charge carrier concentration Δp. The majority charge carrier can be dominated by photo-excited charge carriers concentration Δp or by the doping p_0. Therefore, radiative recombination is of first-order for low injection levels $(\Delta p \ll p_0)$, or of second-order for high injection levels $(\Delta p \gg p_0)$.

2.3.5 Auger Recombination

In Auger recombination, the energy of the recombining electron and hole pair is transferred to a third excited charge carrier. Thereby this charge carrier is usually excited from a band edge into states deeply within the band.

The Auger combination rate R_{Auger} is given by the individual rates for the Auger excitation of holes with an Auger coefficient C_h and for the Auger excitation of electrons with an Auger coefficient C_e. Usually, Auger recombination only has a significant contribution to the overall recombination if the excited charge carrier concentration is much larger than the doping concentration. Under such conditions, it is a third-order process.

$$R_{Auger} = C_n nnp + C_p ppn \approx \left(C_n + C_p\right)\Delta p^3 \tag{2.22}$$

2.4 Charge Carrier Transport

The charge carrier transport and the evolution of the spatial distribution of charge carriers were described in Section 2.2 based on the charge carrier mobility μ. In the present section, the charge carrier mobility and its frequency-dependence will be derived from the classical motion of a single charge carrier. Other approaches as the Boltzmann-transport equation, the Kubo equation and Monte Carlo simulations [24] will not be discussed here to limit the extent of this work.

The frequency-dependence of the mobility is indicative for the nature and for the limitations of the charge transport. In particular, the frequencies around 1 THz are characteristic for the individual transport mechanisms and will be measured experimentally by time-resolved terahertz spectroscopy in Chapter 6.

Recommended reviews on transport models at terahertz frequencies are: [25] [26] [27].

2.4.1 Classical Motion of a Single Charge Carrier

The frequency-dependent mobility of free or bound charge carriers can be derived from the classical motion of a single charge carrier.

To this end, the displacement $r(t)$ of a charge carrier can be described with Equation (2.23) by a driven harmonic oscillator. Within this model charge carriers with an effective mass m_{eff} and charge q are accelerated by an electric field E (of the terahertz pulse). Additionally, they experience damping due to scattering with a momentum relaxation time τ_{scat}, which randomized their momentum (sets the average velocity to zero). Further, a restoring force $m_{eff}\omega_0^2 r$ of a parabolic potential may act on the charge carriers.

$$m_{eff}\frac{d^2}{dt^2}r + \frac{m_{eff}}{\tau_{scat}}\frac{d}{dt}r + m_{eff}\omega_0^2 r = qE \tag{2.23}$$

The displacement of the charge carrier causes an electric current *I = q*n*dr/dt*. This current can also be stated by Ohm's law in Equation (2.11) by the mobility μ and the concentration of the charge carriers *n*. The combination of both equations leads to:

$$\frac{d}{dt}r = \mu E \tag{2.24}$$

The combination of equations (2.23-24) with an oscillating electric field *E(t,f)*, which is described by Equation (2.25), yields the frequency-dependent mobility *μ(f)*. For brevity, the following equations are stated with the angular frequency $\omega = 2\pi f$.

$$E(t) = E_0\, exp(-i\omega t) \tag{2.25}$$

The mobility of charge carriers at direct currents μ_{DC} (zero frequency) can be stated as single and real value. This value is of particular importance for the charge transport in a solar cell, which operates at direct currents. However, for alternating currents, the mobility becomes complex-valued and depends on the frequency of the alternating current. Its phase states the delay of the oscillation of the charge carriers with respect to the oscillation of the electric field.

2.4.2 Drude Model of Free Charge Transport

The Drude model describes the transport of free charge carriers, which move in accordance with Equation (2.23) but without the influence of a restoring force or a potential ($\omega_0 = 0$). It is determined by the effective mass m_{eff} of the charge carrier and the scattering time τ_{scat} with which the momentum of the charge carrier is randomized, which is illustrated in Figure 2.2a. At room temperature, this scattering is usually dominated by optical phonon scattering. At lower temperatures, acoustical phonon scattering and ionized impurity scattering dominate [24].

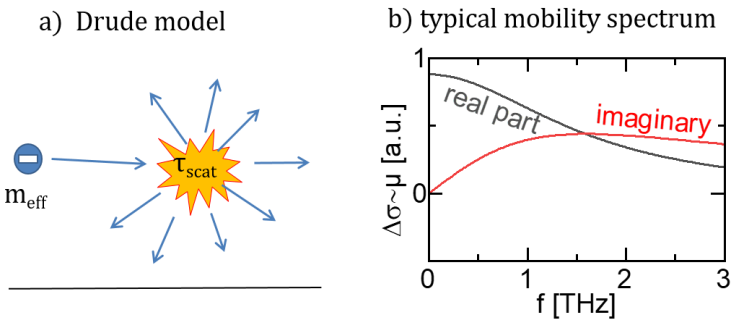

Figure 2.2: Drude model. *a) A charge carrier has an effective mass m_{eff} and scattering randomizes its momentum after a scatting time τ_{scat}. b) Drude mobility modeled for τ_{scat} = 100 fs.*

The combination of equations (2.23-25) yields the frequency-dependence of the charge carrier mobility μ_D in the Drude model, which is shown in Figure 2.2.

$$\mu_D = \frac{e\tau_{scat}}{m}\frac{1}{1 - i\omega\tau_{scat}} \tag{2.26}$$

Characteristics for the Drude mobility are a positive real part that decreases with frequency and a positive imaginary part as shown in Figure 2.2b. The Drude mobility usually decreases with temperature due to an increasing phonon density and the corresponding scattering of the charge carriers with these phonons.

2.2.3 Lorentz Model of Localization

The Lorentz model adds a parabolic potential $V(r) = \omega_0^2 r^2/2$ to the Drude model, which results in a restoring force ($\omega_0 \neq 0$) and localizes the charge carrier in the potential. The charge carrier mobility μ_L in the Lorentz model is described by Equation (2.27) and is shown exemplarily in Figure 2.3b.

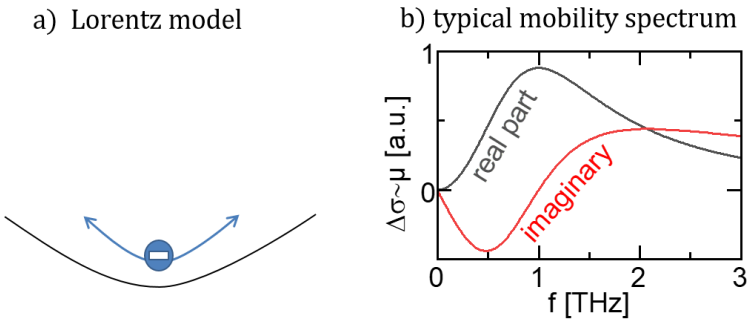

Figure 2.3: Lorentz model. *a) A parabolic potential with resonance frequency f_0 is added to the Drude-model. b) Lorentz mobility modeled for τ_{scat} = 100 fs and f_0 = 1 THz.*

$$\mu_L = \frac{q}{m_{eff}}\frac{\omega}{\frac{\omega}{\tau_{scat}} - i(\omega^2 - \omega_0^2)} \tag{2.27}$$

For low frequencies, the real part increases with frequency and the imaginary part adapts negative values. Such behavior is in strict contrast with the Drude mobility of free charge carriers and indicates some kind of localization of the charge carriers. It will be shown later on that such a frequency-dependence can also be described in alternative localization models such as the hopping model or the Drude-smith model. However, a unique feature of the Lorentz model is that the DC-mobility is zero.

Additionally, Lorentz-like mobilities do not only describe electrons or holes in a parabolic potential. It also describes oscillations of charges in general as the vibration of lattice ions or as vibrations of polar molecules. Further, transitions between states with an energy difference $\Delta E = hf_0$ can be described by a Lorentz-like dielectric function $\varepsilon = \varepsilon_0 + ie\mu n/\omega$ and the corresponding optical mobility μ.

2.2.4 Tunneling & Hopping Transport

The tunneling model is another model for localized transport. It was developed for disordered semiconductors but has also been applied to other materials. In general, it describes the tunneling (or hopping) between states that are separated by energetic barriers, which is illustrated in Figure 2.4a.

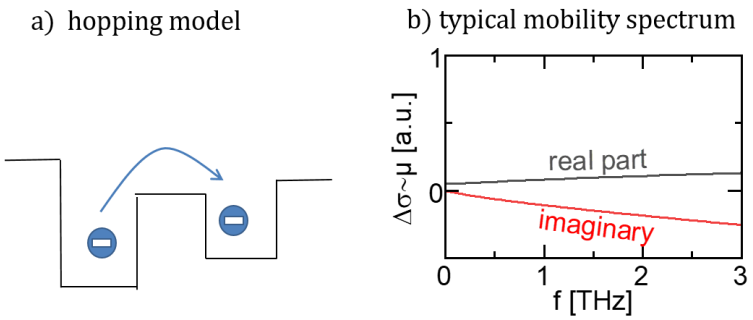

Figure 2.4: Hopping and tunneling model. *a) Hopping or tunneling between localized states. b) Hopping mobility modeled for hopping/tunneling time τ_t = 1 ps.*

The charge carrier mobility in the hopping/tunneling model μ_t is described by Equation (2.28) [27-29] and is shown exemplarily in Figure 2.4b.

$$\mu_t = \mu_0 \frac{i\omega\tau_t}{ln(1 - i\omega\tau_t)} \quad with \quad \sigma_t = \frac{N_t q^2 d^2}{6 k_B T \tau_T} \tag{2.28}$$

The tunneling mobility depends on the tunneling (or hopping) time τ_t, the density of hopping states N_T and the average distance between these states d.

Indications for tunneling transport are negative imaginary mobilities that decrease with frequency and a positive real part that increases with frequency. The transport is thermally activated and therefore, the mobility increases with temperature.

2.2.5 Drude-Smith model of Partial Localization

The Drude-Smith model is very common for the description of frequency-dependent mobilities in the terahertz range [30]. The charge carrier mobility in the Drude-Smith model μ_{DS} is described by Equation (2.28) and is shown exemplarily in Figure 2.5.

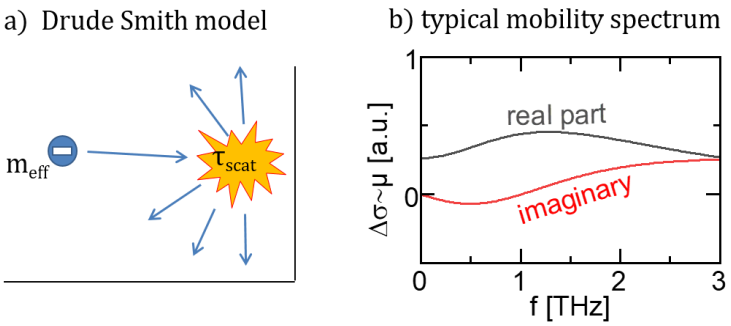

Figure 2.5: Drude-Smith model. *a) Charge carrier transport with preferential back scattering probability c_1. b) Drude-Smith mobility modelled for hopping time τ_{scat} = 100 fs* and *c_1=-0.7.*

$$\mu_{DS} = \frac{e\tau_{scat}}{m_{eff}} \frac{1}{1 - i\omega\tau_{scat}} \left(1 + \frac{c_1}{1 - i\omega\tau_{scat}}\right) \tag{2.29}$$

It was originally derived from the preferential back-scattering of charge carriers, which compares to a random scattering in the Drude-model. However, the original deviation of Equation (2.28) is somewhat unphysical. It assumes that only the first scattering event preferentially scatters backward with a probability of c_1, which is illustrated in Figure 2.5a. It spans from 0 for random scattering to -1 for total backscattering. The following scattering events again randomize the momentum. Therefore, concerns were raised whether the model has a physical meaning. Monte Carlo simulations of charge carrier transport through energetic barriers with preferential backscattering resulted in a similar frequency-dependence of the mobility and are in support of the model [31]. However, an analytic deviation of Equation (2.28) is still missing. To highlight the phenomenological nature of the Drude-Smith model here the term “localization parameter” will be used for c_1, which quantifies the degree of charge carrier localization regardless of the underlying origin of the localization.

Regardless of these concerns, the Drude-Smith model is widely applied because it models the frequency dependence of measured mobilities very well. The frequency-dependence of the Drude-model and of the Lorentz-model are reproduced for localization parameters c_1 of 0, -1, respectively. Intermediate values model partially localized charge carriers.

Another advantage of the phenomenological Drude-Smith model description is that a reasonable DC-mobility can be modeled by the Drude-Smith model that fulfills the Kramers-Kronig relation between the imaginary and the real part of the mobility and can be applied if the origin of the localization is unclear.

2.2.6 Plasmons

The plasmon model describes the localization of a cloud of charge carriers due to barriers or inhomogeneity. This effect is different from the localization by back-scattering at the boundary, which

was discussed in the section on the Drude-Smith model. The boundaries can be to spare that a significant amount of charge carriers directly interact with them. However, an external field for example, a terahertz pulse as illustrated in Figure 2.6a, can shift the charge carriers. A few charge carriers accumulate at the boundaries and build up a polarization potential in Figure 2.6b. These polarization fields are long-ranged and as restoring force, which even localizes charge carriers that are far away for the boundary as illustrated in Figure 2.6c.

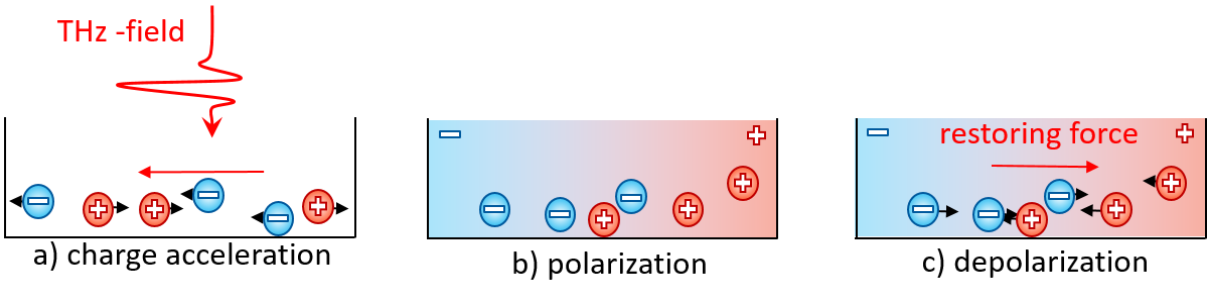

Figure 2.6: Plasmon model for carrier localization. *a) An electric field induces a charge current. b) At boundaries, charges accumulate and build up a polarization. c) The potential of the polarization acts as a restoring force and results in Lorentz-like mobilities.*

Such a plasmonic effect can be modeled by the Continuity equation (2.9), Ohm's law (2.11) and the Poisson equation (2.13). In approximation, the amplitude of the restoring force increases with the charge carrier concentration. Therefore, such a plasmonic resonance can be identified by its injection dependence. For an increasing charge carrier concentration the charge carrier mobility decreases and the resonance frequency is shifted to higher frequencies, which is described by [32]:

$$\omega_{0p} = \sqrt{\frac{fpq^2}{m_{eff}\varepsilon_r\varepsilon_0}} \tag{2.29}$$

3 Limits of Photovoltaic Materials

A solar cell converts the irradiation of the sun into electric power. The efficiency of this conversion is the main criterion for the performance of a solar cell and is given by the current-voltage curve of the solar cell.

In this chapter, the short circuit current and the open-circuit voltage are derived from the internal and from the external properties of the absorber layer. The external properties view the absorber as a black box and regard only the quantities that enter and leave the absorber: namely the photon current from the sun, the reemitted photoluminescence from the absorber, and the electric current, which is collected in the solar cell. In contrast, the internal properties describe the charge carrier dynamics within the absorber layer.

3.1 Principle of a Solar Cell

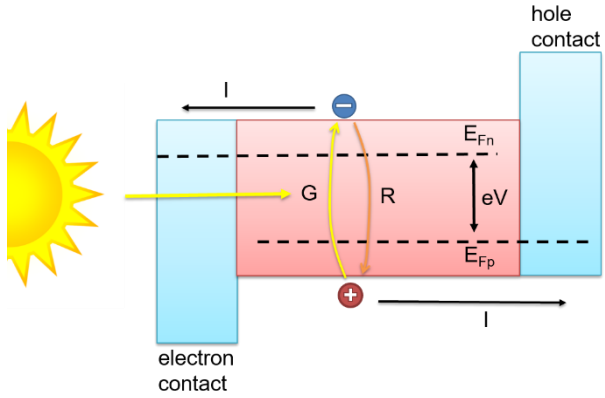

Figure 3.1 Principle of a solar cell. *The sunlight is absorbed and excites charge carrier with a generation current G. This current is balanced by the recombination current R and extractions as electric current I. The splitting of the quasi-Fermi levels E_F generates the voltage V of the solar cell.*

The basic processes in a solar cell are illustrated in Figure 3.1. The sunlight is absorbed in a layer made of the photovoltaic material and photo-excites electron and holes at a generation current *G*. Consequently, a concentration of photo-excited electrons Δn and holes Δp builds up until the generation current *G* of charge carriers is balanced by their recombination current *R* and by their extraction as an electric current *I*. The concentration of photo-excited electrons and holes determines the splitting between the quasi-Fermi levels of electrons in the conduction band E_{Fn} and of holes in the valence band E_{Fp}. This splitting $\Delta E_F = eV$ determines the external voltage *V* of a solar cell with ideal contacts.

In solar cells, electrons and holes have to flow into opposite directions and the quasi-Fermi levels of electrons and holes have to extend into opposite contact layers, which is illustrated in Figure 3.1. Therefore, the solar cell has selective contacts that prefer either electron or hole transport and enforces opposite currents of electrons and holes. A p-n junction between a p-doped and an n-doped

semiconductor is the prevalent realization of such a selective contact. However, bandgap gradients such as in $Cu(In,Ga)(Se,S)_2$ or the appropriate band off-set at the interfaces such as in dye solar cells can also be used [33].

The performance of a solar cell depends not only on the absorber layer but also on the properties of the contact layers and of their interfaces. However, here we concentrate exclusively on the absorber properties to guide the selection of suitable materials as solar cell absorber.

3.2 External Properties and the Shockley-Queisser Limit

The estimation of the performance of a photovoltaic material by its external properties is a powerful concept. Most prominently it was applied by Shockley and Queisser to derive the ultimate limit of solar cell [34] and to measure the quasi-Fermi level splitting (QFLS) inside a photovoltaic material [35].

The so-called "Shockley-Queisser limit" is a very powerful and simple approach. In the original paper from Shockley and Queisser, it is called the "ultimate limit" [34]. It allows estimating the whole current-voltage characteristic of a solar exclusively from the bandgap energy of the absorber materials. Here, the short circuit current will be addressed first, which is followed by the open-circuit voltage and the efficiency.

3.2.1 The Short Circuit Current

In the external approach, the short circuit current equals the absorbed photon current. To calculate the absorbed photons, Shockley and Queisser approximated the absorption *a* by a step-like onset from zero to unity at the bandgap energy E_G. This situation is visualized in Figure 3.2a on the example of a $Cu_2ZnSnSe_4$ thin film which will be probed in the following chapter and has a bandgap energy of 0.97 eV. Above this bandgap energy all photons are absorbed and generate charge carriers.

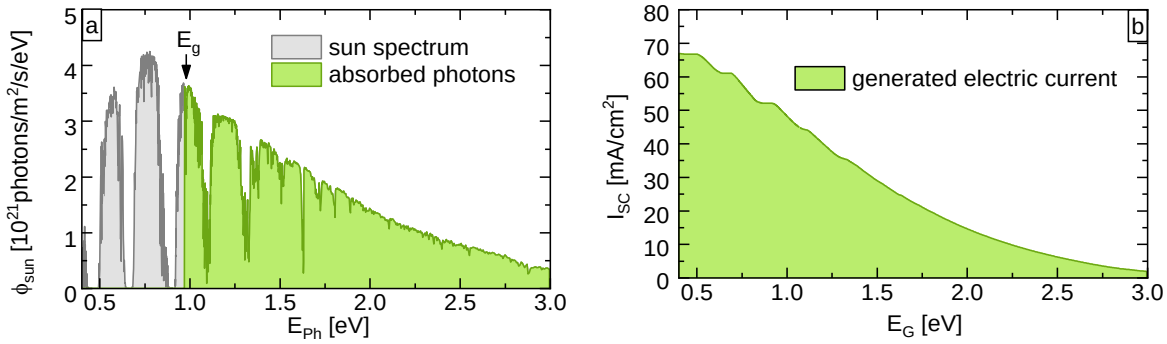

Figure 3.2 Absorption of photons and generation of charge carriers. *a) The incident photon spectrum of the sun is absorbed above the bandgap energy E_G and generates a charge carrier current. b) The generated electric current in short circuit conditions I_{SC} decreases with the bandgap energy.*

Therefore, the short circuit current in the Shockley-Queisser limit depends exclusively on the bandgap energy of the photovoltaic material and on the spectrum of the sun. The photon spectrum of the sun ϕ_{sun} was approximated by Shockley and Queisser by a black body spectrum at 6000 K [34]. However, here the more realistic AM1.5G sun spectrum will be used because it is the prevalent standard in photovoltaics [36] and takes the absorption of the atmosphere and the angle of the sun into account [37]. This sun spectrum can be seen in Figure 3.2a.

The current of absorbed photons equals the current of generated charge carriers *G,* which is defined in Equation (3.1) in units of particles per area and time.

$$G_{sun} = \int \phi_{sun}(E_{Ph}) a(E_{Ph})\, dE_{Ph} \tag{3.1}$$

The short cut current $I_{sc} = q * G_{sun}$ can be directly calculated from the absorbed photon current G_{sun} and the elementary charge q. It decreases with the bandgap energy E_G of the absorber material as shown in Figure 3.2b. For example, for the bandgap energy of 0.97 eV a photon current of $3.1*10^{17}$ cm^2/s is absorbed, which translates into a short circuit current of 49.8 mA/cm^2.

However, the short circuit current can also be calculated from the measured absorption a instead of the step-like onset, which was assumed in the Shockley-Queisser limit. This approach has the advantage that the generated current is derived more precisely. On the downside, the absorption $a = 1-exp(-\alpha d)$ depends on the thickness d of the absorber layer. In contrast to the absorption coefficient α, such absorption and the derived generation current are not entirely material specific. However, for samples with a sufficient thickness the generation current in the radiative limit barely differs from the Shockley-Queisser limit.

3.2.2 The Open Circuit Voltage

The voltage $V = \Delta E_F/e$ of a solar cell is approximated in the Shockley-Queisser limit with the quasi-Fermi level splitting (QFLS) ΔE_F inside the absorber layer. This Approximation assumes the absence of any transport resistance that could cause a drop between external voltage and internal QFLS. Therefore, the Shockley-Queisser limit implicitly assumes that the charge carrier mobility is infinite.

The QFLS is derived in the Shockley-Queisser limit based on the detailed balance of charge carrier generation, recombination, and extraction as an electric current.

Charge carriers recombine in the Shockley-Queisser limit exclusively via radiative recombination. This implies that all absorbed photons are reemitted as photon current or extracted as an electric current. The radiative recombination current R_{rad} is given by the integral of the emitted photon spectrum ϕ_{PL}:

$$R = R_{rad} = \int \phi_{PL}(E_{Ph}) dE_{Ph} \tag{3.2}$$

$$\phi_{PL}(E_{Ph}) = \frac{2\pi {E_{Ph}}^2}{h^3 c^2} \frac{1}{exp\left(\frac{\Delta E_F - E_{Ph}}{k_B T}\right) - 1} a(E_{Ph}) \approx \frac{2\pi {E_{Ph}}^2}{h^3 c^2} exp\left(\frac{qV - E_{Ph}}{k_B T}\right) a(E_{Ph}) \tag{3.3}$$

This emitted photon spectrum ϕ_{PL} (or photoluminescence) is determined by the so-called Planks generalized law in Equation (3.3) [38]. It states the photoluminescence spectrum for a certain the quasi-Fermi level splitting ΔE_F and for a certain absorption a of the sample. This Equation (3.3) is based on the fact that the absorption and emission are reverse processes and that the transition coefficients between the involved states are equal for both processes. For a quasi-Fermi level splitting ΔE_F that is much smaller than the emitted photon energies Plank's generalized law can be approximated by the right half of Equation (3.3).

The absorption a of the material is given in the Shockley-Queisser limit by the step-like onset at the bandgap energy E_G. Therefore, also the luminescence spectrum (described by Equation 3.3) has an abrupt onset at the bandgap energy, which is shown exemplarily in Figure 3.3a for a bandgap energy of 0.97 eV.

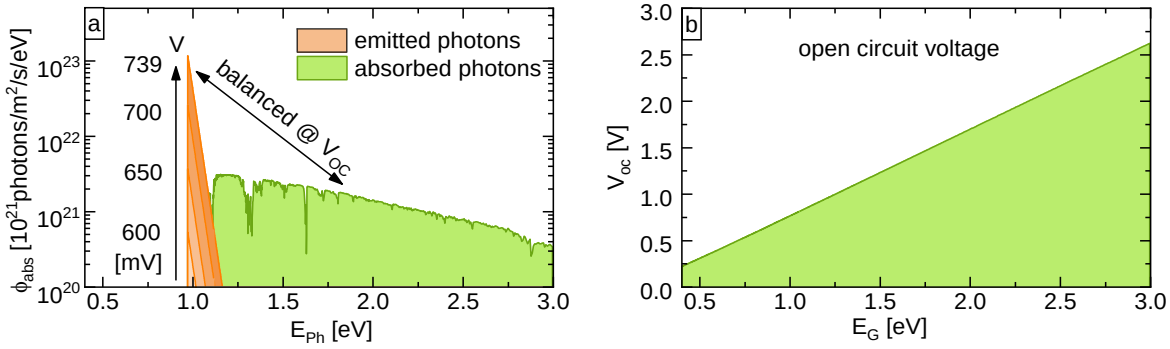

Figure 3.3: Recombination by photoluminescence. *a) The amplitude of the emitted photon spectrum increases with applied voltage or quasi-Fermi level splitting. The overall emitted photon current balances the absorbed photon current from the sunlight at the open-circuit voltage (V_{OC}). b) The open-circuit voltage increases approximately linearly with the bandgap energy of the material.*

Plank's generalized law in Equation (3.3) states that the amplitude of the emitted photon spectrum ϕ_{PL} increases with the applied voltage V. This behavior is also shown in Figure 3.3a for a series of different voltages. In the same way the overall radiative recombination current R_{rad} increases with the applied voltage. At a certain voltage the radiative recombination current R_{rad} balances the generation current from the absorption of sunlight G_{sun}. This voltage is the so-called "open circuit" voltage V_{OC} because for an open circuit no electric current flows into or out of the solar cell and the generation of charge

carriers has to be balanced by the recombination of charge carriers in the steady-state. For instance, a bandgap of 970 meV results in a V_{OC} of 739 mV in the Shockley-Queisser limit.

This behavior can also be expressed analytically. Under open-circuit conditions, the absorption photon current G is balanced by the radiative recombination current R_{rad}. This balance $G = R_{rad}$ yields in combination with Equations (3.1-3) the open-circuit voltage:

$$V_{OC} = \frac{E_G}{q} + \frac{k_B T}{q} ln\left(\frac{G_{sun}}{\int \frac{2\pi {E_{Ph}}^2}{h^3 c^2} exp\left(\frac{E_G - E_{Ph}}{k_B T}\right) a(E_{Ph}) dE_{Ph}}\right) \tag{3.4}$$

The step-like absorption onset at the bandgap energy of the Shockley-Queisser limit yields under the assumption $k_B T << E_G$ an open circuit voltage $V_{OC\text{-}SQ}$ of:

$$V_{OC-SQ} = \frac{E_G}{q} + \frac{k_B T}{q} ln\left(\frac{G_{sun}}{\frac{2\pi {E_G}^2}{h^3 c^2} k_B T}\right) \quad for\ E_G \gg k_B T \tag{3.5}$$

Plank's generalized law (3.3) can also be used to derive the quasi-Fermi level splitting inside a photovoltaic material from the absorption a and from the emitted photon current ϕ_{PL}. To this end, the sample is excited by 1 sun equivalent photon current and the photoluminescence spectrum is measured by a spectrometer that is calibrated to absolute photon numbers.

3.2.3 The Efficiency

The full current-voltage curve of a solar cell in the Shockley-Queisser limit is derived in Equation (3.6) from the detailed balance $I = qG\text{-}qR$ of the recombination current R, the generation current G and the extracted electric current I. The generation current G is given by the absorption of the sunlight in Equation (3.1) and the recombination current R is given exclusively by the radiative recombination R_{rad} in Equation (3.2). The voltage dependence of the current in Equation (3.6) originates from the radiative recombination, which increases exponentially with the applied voltage in Equation (3.3). Interestingly, no junction between a p-doped and an n-doped semiconductor had to be assumed to derive such a diode like behavior.

$$I = qG - qR = eG_{sun} - q\frac{2\pi {E_G}^2}{h^3 c^2} k_B T * exp\left(\frac{-E_G}{k_B T}\right)\left[1 - exp\left(\frac{qV}{k_B T}\right)\right] \tag{3.6}$$

The comparison with the I-V curve of a usual diode equation for p-n junction solar cells in Equation (3.7) derives the short circuit current I_{SC} and the saturation current I_0.

$$I = I_{sc} - I_0 \left[exp\left(\frac{eV}{k_B T}\right) - 1 \right] \tag{3.7}$$

Such a current-voltage curve is shown in Figure 3.4a for a material with a bandgap of 0.97 eV. The maximum electric power P_{el} is generated at the maximum power point by the product of the voltage V_{MP} and the current I_{MP}. These values define the power conversion efficiency η of a solar cell in Equation (3.8).

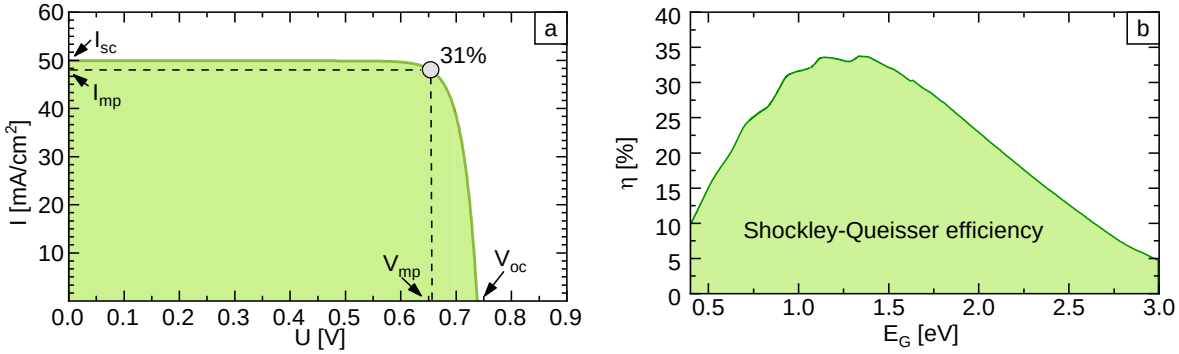

Figure 3.4: Photovoltaic efficiency in the Shockley-Queisser limit. *a) The current-voltage curve in the Shockley-Queisser limit for a absorber with a bandgap energy of 0.97 eV. Current I_{MP} and voltage V_{MP} at the maximum power point as well as the open-circuit voltage V_{OC} and short circuit current I_{SC} are indicated. b) Power conversion efficiency η of the Shockley-Queisser limit depends exclusively on the bandgap energy E_G.*

$$\eta = \frac{P_{el}}{P_{sun}} = \frac{I_{MP} V_{MP}}{P_{sun}} = \frac{I_{SC} V_{OC} FF}{P_{sun}} \tag{3.8}$$

However, the fill-factor *FF,* which connects the product of the current and the voltage at the maximum power point with the open-circuit voltage and the short circuit current could not be derived analytically here. Therefore, the power conversion efficiency was evaluated numerically by finding the maximum power point in the I-V curve and comparing the generated electrical power density to the power density of the sunlight. For a bandgap of 0.97 eV a maximum power conversion efficiency of 31.4 % was derived.

The full dependence of the "Shockley-Queisser efficiency" on the bandgap energy is shown in Figure 3.4b. It states the range of suitable band gaps for the application as single-junction solar cells.

3.3 Internal Properties

The estimation of the performance of a photovoltaic material by its internal properties is more complex than the estimation from the external properties. Here such an estimation is limited to the properties of the absorber layer and therefore assumes ideal contacts.

3.3.1 The Short Circuit Current

The short circuit current will be estimated here in a limit which will be called the “diffusive limit”. It regards the limited mobility of charge carriers in the absorber of the solar cell and the competition of charge carrier extraction and recombination. Therefore, the short circuit current will not be exclusively determined by the absorbed photons as in the “Shockley Queisser limit” but also by their collection efficiency. However within the “diffusive limit”, it will be assumed that the transport to the contacts is exclusively diffusive and that no drift in a space charged region occurs.

If the transport of charge carriers is considered, the sample cannot be assumed homogeneous anymore and the depth dependence has to be included. To this end, the continuity equation of transport and recombination - which was discussed in Chapter 2 - can be evaluated. In addition, the carrier transport can be affected by electric potentials such as the space charge region of solar cells. In this case, also the Poisson equation has to be incorporated into the model [33]. However, such a model is very complex and depends also on the properties of the contact layer. It is for example implemented in numerical programs such as SCAPS [39].

However, to limit the complexity here, we will regard a relatively simple model for the diffusive collection of the electric current of a solar cell illustrated in Figure 3.4. An incident photon has to fulfill two criteria to contribute to the electric current. First, it has to be absorbed and second, the generated charge carriers have to be collected at the contacts.

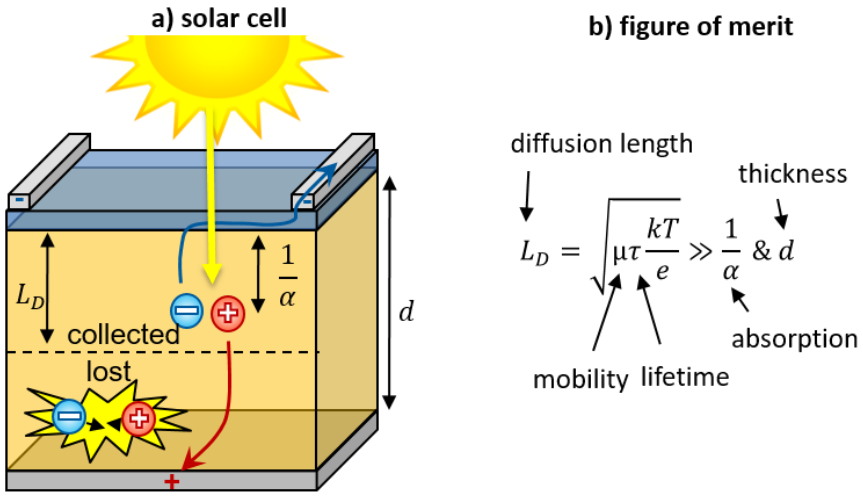

Figure 3.4: Current collection in a solar cell. *a) Illustration of the collection of charge carriers which are absorbed within the diffusion length L_D. b) A figure of merit for the charge carrier collection in a solar cell.*

The efficiency of charge carrier collection depends on the competition of recombination of charge carriers and their diffusive transport to the contacts as illustrated in Figure 3.4a. The charge carriers are generated in a certain depth which is characterized by the absorption depth 1/α – the inverse of

the absorption coefficient α. These generated charge carriers have a certain mobility μ and lifetime τ which define their diffusion length L_D in equation (2.25).

$$L_D = \sqrt{\frac{k_B T}{e} \mu\tau} \tag{3.2}$$

This diffusion length quantifies how fare excited carriers can diffuse before they recombine. In a simple model, carriers are collected if their absorption depth 1/α is within the diffusion length. Carriers that are excited beyond the diffusion length are lost. This condition $1/\alpha > L_D$ was used to define a figure of merit *FM* in [40]:

$$FM = \frac{k_B T}{e} \mu\tau\alpha^2 \tag{3.3}$$

However, to evaluate this figure of merit a somewhat arbitrary value form the spectrum of the absorption coefficient has to be chosen.

Instead, the collected charge carrier current can be analytically calculated in the "diffusive limit" from the same quantities that are included in the figure of merit. It was shown in [41] that the internal quantum efficiency *IQE* of the collection of a photo-excited charge carrier per photon that enters the absorber is given by:

$$IQE = \frac{\alpha L_D}{\alpha^2 L_D^2 - 1} \left\{ \alpha L_D - \frac{sinh\left(\frac{d}{L_D}\right) + \alpha L_D \exp(-\alpha d)}{cosh\left(\frac{d}{L_D}\right)} \right\} \tag{3.4}$$

Similar equations were derived in [42] and [43]. The external quantum efficiency $EQE = (1-R_F)\, A_F\, IQE$ is derived by including optical losses from the reflection R_F of sunlight at the front contact and from parasitic absorption A_F in the front.

The short circuit current can be calculated in the "diffusive limit" from the EQE by:

$$I_{SC} = e \int \phi_{sun}(E_{Ph}) EQE(E_{Ph})\, dE_{Ph} \tag{3.5}$$

3.3.2 The Open Circuit Voltage

The quasi-Fermi level splitting (ΔE_F) inside the absorber layer and the corresponding voltage of a solar cell can also be derived from the internal properties of the absorber layer. This approach is based on the equations of the charge carrier occupation of the density of states that were introduced in Section 2.1.

The quasi-Fermi levels of electrons in the conduction band $E_{F,e}$ and of the holes in the valence band $E_{F,h}$ can be stated in equations (3.6-7) with respect to an effective density of states of the conduction band N_C and of the valence band N_V.

$$E_{Fn} = E_C + k_B T ln\left(\frac{n}{N_C}\right) \tag{3.6}$$

$$E_{Fp} = E_V - k_B T ln\left(\frac{p}{N_V}\right) \tag{3.7}$$

The combination of the equations (3.6-7) yields the splitting of the quasi-Fermi levels of electrons and holes ΔE_F and the corresponding voltage of $V = \Delta E_F/q$:

$$V_{OC} \approx \frac{\Delta E_F}{q} = \frac{E_G}{q} + \frac{k_B T}{q} ln\left(\frac{n}{N_C}\frac{p}{N_V}\right) \tag{3.8}$$

The carrier concentration of electrons n and of holes p are given by the sum of their doping concentration p_0 *(or* n_0*),* and by the excited carrier concentration $\Delta p = \Delta n$. The concentrations of excited electron and holes are assumed to be equal because both are generated and recombine at the same rate. In the following, the equations will be stated for a p-type semiconductor. For an n-type semiconductor n and p have to be interchanged.

$$p = p_0 + \Delta p \tag{3.9}$$

The excited charge carrier concentration Δp can be estimated from the balance of charge carrier generation rate g and recombination rate r. The recombination rate can be described by a carrier concentration Δp which decays with a lifetime τ. The generation rate g is the generation current G as defined in Equation (2.1) divided by the absorber thickness d if a homogeneously excited absorber is assumed. It should be noted that the rates r and g are defined in units of particles per volume and time whereas the currents R and G are defined in units of particles per area and time. The former ones are internal quantities and the later ones are external quantities.

$$r = g \;\rightarrow\; \Delta p = \frac{G\tau}{d} \tag{3.10}$$

Finally, the open-circuit voltage (or ΔE_F) is given:

$$V_{OC} q \approx \Delta E = E_G + k_B T * ln\left(\frac{\frac{G\tau}{d}\left[\frac{G\tau}{d} + p_0\right]}{N_C N_V}\right) \tag{3.11}$$

Therefore, the open-circuit voltage of a solar cell is determined by the bandgap energy E_G, the temperature T, the charge carrier lifetime τ, the effective density of states N_V and N_C, the doping p_0 and the absorber thickness d.

4 Time-resolved Terahertz Spectroscopy

Time-resolved terahertz spectroscopy (TRTS) is also known as "optical-pump terahertz-probe", "transient terahertz absorption" or "terahertz conductivity" spectroscopy. This chapter is based on several excellent reviews [26], [44], [45] and [46] and describes the technique in-depth.

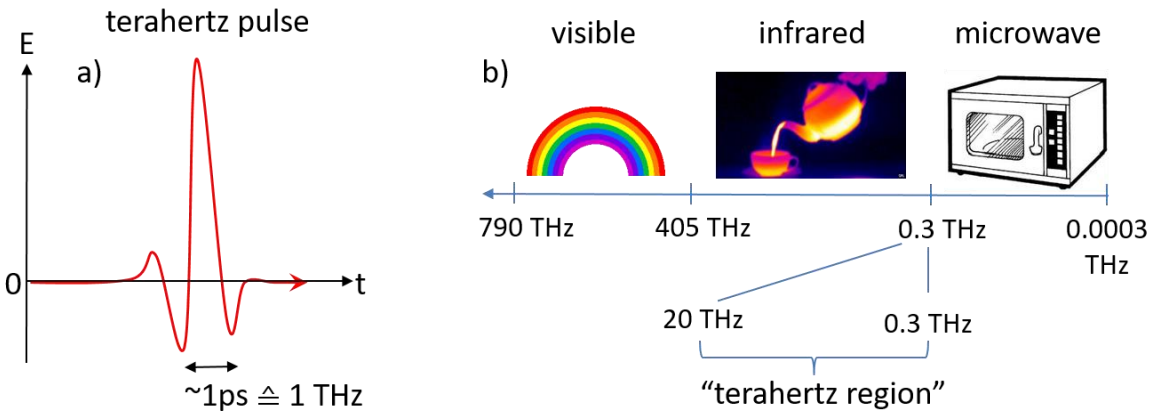

Figure 4.1: Illustration of terahertz light. *a) The electric field (E) of a terahertz pulse in time-domain. b) Electromagnetic spectrum with an indication of the "terahertz region".*

TRTS is a unique tool that probes photo-excited matter via its interaction with far-infrared light. It distinguishes itself from other time-resolved techniques by the usage of terahertz radiation as a probe pulse.

A terahertz pulse is illustrated in Figure 4.1a and is a pulse of light with an electric field that oscillates at terahertz frequencies which correspond to an oscillation period in the order of 1 ps. One of the beauties of the method is that it shows directly that light is a wave of an electric field.

Instead of its oscillation frequency light is often characterized by alternative quantities that correspond to each other: 1THz (oscillation frequency) ≙ 1ps (oscillation period) ≙ 4.1 meV (photon energy) ≙ 30 cm^{-1} (wavenumber) ≙ 300 µm (wavelength) ≙ 48 K (black body radiation). The so-called "THz region" roughly includes the range from 0.3-20 THz which is the far-infrared region of the spectrum of light.

Such terahertz radiation is in the sweet spot for many applications and makes TRTS outstanding from other time-resolved pump-probe techniques such as near infra-red transient absorption spectroscopy on the shorter wavelength side and from time-resolved microwave conductivity spectroscopy on the longer wavelength side. Its advantages include the following:

A): Its typical frequency of 1 THz is in the frequency-range where the scattering and localization of charge carriers on the nm-scale leaves fingerprints in the conductivity and mobility, which allows probing these transport properties by TRTS.

B): Its typical oscillation period of 1 ps is long enough for electro-optical sampling of the electric field and allows to measure not only the intensity but the time-resolved electric field of the terahertz pulse with the full information on amplitude and phase.

C): Its typical photon energy of 4.1 meV is in the range of the ground state energies of excitons [47] and quantum wells. Therefore, TRTS allows probing of their behavior under photo-excitation.

D): Its typical wave number of 33 cm^{-1} is the range of phonons and molecular oscillation. It allows studying their behavior under photo-excitation.

E): Its typical wavelength of 300 µm is small enough for reasonable spatial resolution and free space propagation in a tabletop system. This property allows the contact-less mapping of samples by TRTS.

Here, we will concentrate on the characterization of photo-excited charge carriers and in particular on their recombination kinetics and on their transport properties.

4.1 Principle of TRTS

The principle of TRTS is shown in Figure 4.2.

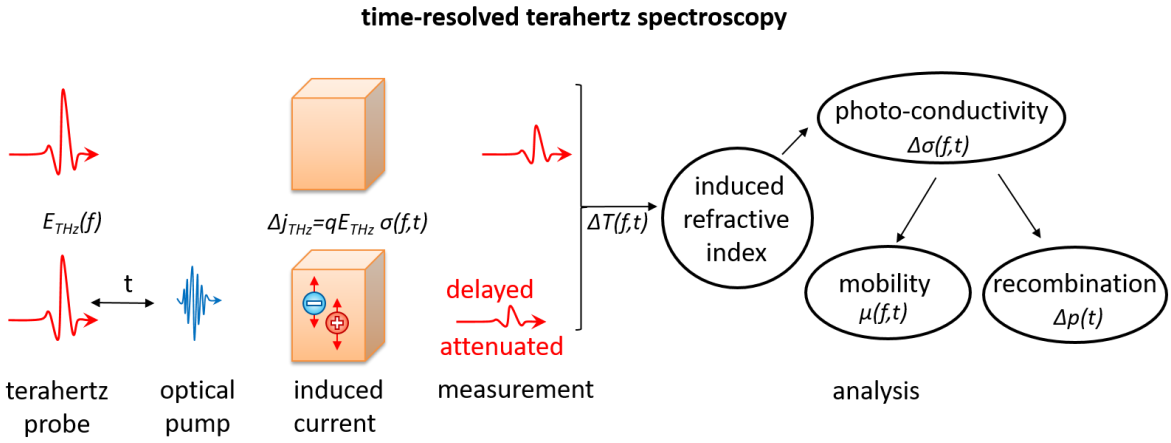

Figure 4.2: Time-resolved terahertz spectroscopy in a nutshell. *An optical pump pulse photo-excites a charge carrier concentration Δp. The terahertz probe pulse has an electric field E(f) that oscillates at terahertz frequencies f and induces a current Δj_{THz} that is described by the photo-induced conductivity Δσ(f). The photo-induced change in the terahertz transmission ΔT is measured in the TRTS setup and can be analyzed for Δσ and subsequently for the mobility µ and recombination kinetics in Δp(t).*

First, a terahertz-probe pulse is measured after it is transmitted through (or reflected from) the sample. Then, charge carriers are photo-excited by an optical-pump pulse in the sample and the terahertz pulse is transmitted through (or reflected from) the sample again. Thereby, the electric field

of a terahertz pulse accelerates the photo-excited charge carriers and induces a current $j = q\Delta\sigma E$, which is proportional the electric field strength of the terahertz pulse E, to the pump-induced photoconductivity $\Delta\sigma$ and to the charge q of the charge carrier. The terahertz probe-pulse itself loses a part of its energy to the accelerated current and is attenuated and delayed. This pump-induced change in the terahertz transmission ΔT (or reflection) is measured in the TRTS setup.

It can be analyzed for the pump-induced refractive index, which can be attributed to the photoconductivity of the photo-excited charge carriers $\Delta\sigma(t,f) = e\mu(t,f)\Delta p(t)$ and subsequently for the charge carrier mobility μ and the photo-excited charge carrier concentration Δp. It should be noted that in this chapter the charge carrier concentration is labeled p and the refractive index by n.

The photoconductivity $\Delta\sigma(f)$ and mobility $\mu(f)$ are derived as a function of the frequencies that constitute the terahertz pulse (typically 0.5-3 THz) and the TRTS measurement can be viewed as an impedance measurement at such terahertz frequencies. This frequency-dependence is characteristic for the nature of charge carrier transport and can be analyzed for additional transport parameters such as the transport effective mass, the scattering time and the localization strength, which were discussed in Section 2.4.

Additionally, the transient photoconductivity $\Delta\sigma(t)$ is derived as a function of the delay time t between the optical-pump and the terahertz-probe pulse and therefore measures the kinetics in the transport properties and the recombination of the photo-induced charge carriers.

4.2 Setup

In TRTS setups a terahertz pulse has to be generated, a pump pulse has to excite the sample and the terahertz pulse has to be detected. These three steps define the main components of a TRTS setup as illustrated in Figure 4.3. The terahertz generation and detection parts are similar to a terahertz time-domain spectrometer (TDTS) [48] which is used to probe the steady-state absorption and refractive index, and the layer thickness of a sample. The TRTS setup is additionally constituted of an optical pump pulse to photo-excite charge carriers and to measure the photo-induced kinetics of the sample.

4.2.1 Terahertz Time Domain Spectrometer

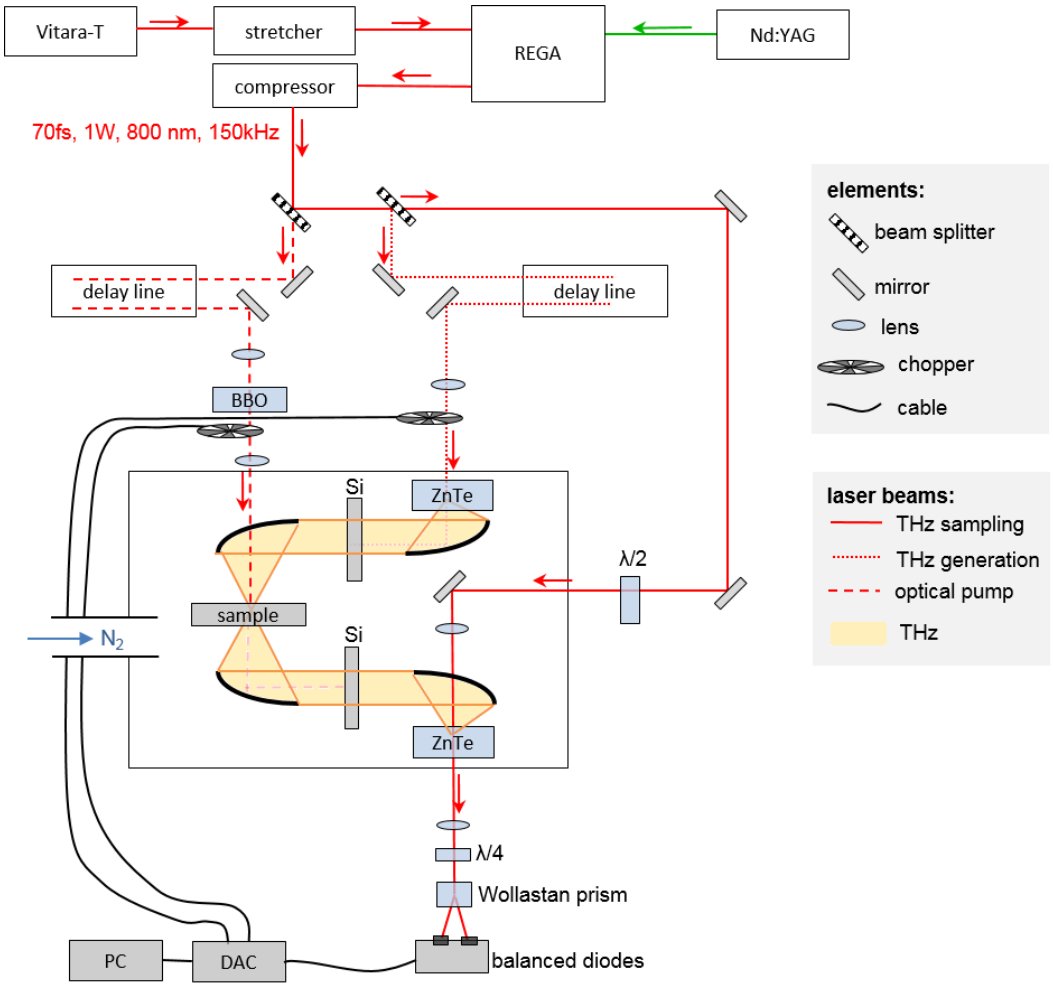

Figure 4.3: Illustration of a time-resolved terahertz spectroscopy (TRTS) setup. *The TRTS-setup consists of a terahertz generation part and a terahertz sampling part which constitute a steady-state time-domain terahertz setup. Additionally, a TRTS setup includes a pump beam to photo-excite the sample.*

Our particular setup is based on a titanium-sapphire laser (Vitara-T from Coherent) which generates laser pulses at a repetition rate of 80 MHz, with a typical average power of 600 mW, a center wavelength of 800 nm and a spectral full width half maximum (FWHM) of 36 nm. These laser pulses are dispersed and stretched by a reflective grading and amplified in a titanium-sapphire based regenerative amplifier (REGA from Coherent). To this end, the repetition rate is picked down by an acousto-optical modulator to 150 kHz and the average power is amplified to ca. 1.4 W, which corresponds to a pulse energy of ca. 10 µJ. These pulses are compressed by a refractive grading to a temporal FWHM of ca. 70 fs.

Afterward, the laser pulses are split into three beams which are used for: terahertz generation, sample excitation and terahertz sampling.

The terahertz generation is achieved by optical rectification of the first laser beam in a ZnTe crystal. Optical rectification is a non-linear optical process and can be viewed as difference frequency generation of the different spectral components in the laser pulse. Alternatively, a terahertz pulse can also be generated by exciting a photo-conductive switch with a femtosecond laser pulse, by focusing a high energy laser pulse in the air which generates a plasma or by exciting a spin-tonic terahertz emitter [49].

The output of the optical-rectification is a terahertz pulse that carries the polarization and divergence of the 800 nm beam from which it was generated. It is collimated with an off-axis parabolic gold mirror and passes a silicon wafer, which absorbs the residual light from the 800 nm laser pulse. A second parabolic mirror focusses the terahertz beam onto the sample. In its focus the terahertz beam has a spatial FWHM of ca. 1 mm.

The terahertz sampling is conducted in a second ZnTe crystal of 0.5 mm thickness by electro-optical sampling. To this end, the terahertz beam is re-collimated after passing the sample by a third parabolic mirror. Again, it passes a second silicon wafer which absorbs and suppresses residual pump light. Finally, the terahertz beam is focused on the ZnTe crystal in which it induces a birefringence. This birefringence is proportional to the amplitude of the electric field of the terahertz pulse.

The sampling beam is the third beam component of the REGA output. Its polarization is turned by a lambda half plate to be vertical compared to the polarization of the terahertz pulse. It is focused collinear with the terahertz beam onto the same spot of the ZnTe crystal.

In the absence of the terahertz beam, the ZnTe crystal is not birefringent and the sampling beam maintains its linear polarization. The sampling beam is collimated with a lens and its polarization is turned into a circular polarization in a lambda quarter-wave plate. Afterward, a Wollastan prism splits this circular polarization into two linear polarized beams with equal intensity and perpendicular polarization to each other. These two beams propagate into different directions. They are guided onto two photodiodes that are balanced and yield the difference-signal of the two of them. In the absence of a terahertz beam, the diodes are exactly balanced and no signal (but noise) is detected.

In the presence of the terahertz beam a birefringence is induced in the ZnTe crystal. This birefringence turns the linear polarization of the sampling pulse and after the lambda quarter plate, it is not completely circular polarized anymore. Hence, the two linear components which are separated in the Wollastan prism have different intensities. This difference is measured by the photodiodes which are off-balanced now. The difference-signal is proportional to the electric field strength of the terahertz pulse that spatially and temporally overlaps with the sampling pulse in the ZnTe crystal.

To sample the full temporal shape of the terahertz pulse it can be shifted by an optical delay stage. While the terahertz pulse shifts, different parts of it overlap with the sampling pulse in the ZnTe crystal and the full temporal shape of it can be scanned.

Alternatively, the terahertz pulse could also be detected by a photoconductive switch or by the ABCD-technique in a gas plasma.

Terahertz radiation is absorbed and dispersed by moisture. Therefore, terahertz propagation in humid air leads to attenuation and stretching of the terahertz pulse. This issue is overcome by housing the Terahertz beam path and purging it with dry nitrogen, which maintains original terahertz amplitude and limits the pulse length which has to be scanned.

To increase the signal-to-noise-ratio the terahertz beam is chopped and a digital locking is used for signal analysis.

4.2.2 Time-resolved Terahertz Spectrometer

The TRTS setup also contains an additional pump beam. The photo-excitation of the sample is achieved in our setup either by using directly the 800 nm laser pulses of the REGA-system or by generating its second harmonic in a 0.3 mm thick BBO crystal. The pump beam is focused on a hole in the second parabolic mirror and excites the sample, where it has been diverged to a spatial FWHM of ca. 3 mm. This spot size is significantly larger than the terahertz spot size with an FWHM of a 1 mm, which is important as our analysis assumes a laterally homogeneous photo-excitation.

The terahertz beam hits the sample with a certain delay with respect to the pump pulse. This delay can be changed by shifting the pump pulse with a delay stage. A scan of this delay stage yields the kinetics of the photo-excitation of the sample.

Alternatively, the pump beam can also be generated by a second laser, which is synchronized to the terahertz pulses for example by q-switching. This approach has the advantage that the delay is not limited by the length of a mechanical delay stage.

The optical pump beam is also chopped but at a different frequency than the terahertz beam. This allows to simultaneously analyze the recorded signal by lock-in technique for the terahertz signal and its pump induced change, which will be detailed in Section 5.4.

4.2.3 Reflection Mode

TRTS in transmission mode is only possible for transparent samples. However many samples or their substrates strongly absorb terahertz radiation. Even 1 mm of glass significantly absorbs terahertz radiation above 1 THz. Such samples can be measured in reflection mode [50] [51] [52] [53] [3].

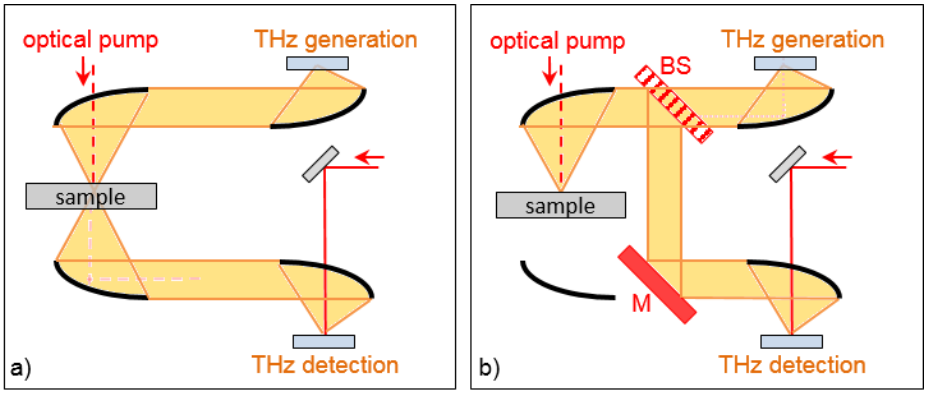

Figure 4.4: Illustration of a convertible TRTS setup. *a) Transmission mode. b) Reflection mode with an additional beam splitter (BS) and mirror (M).*

To this end, the TRTS setup in transmission mode can relatively easily be converted into reflection mode by placing a silicon beam splitter (BS) and a mirror (M) as illustrated in Figure 4.4a/b.

The terahertz beam transmits through the beam splitter and is focused on the sample. A fraction of the terahertz beam is reflected at the sample surface and is collimated by the parabolic mirror that also focused it onto the sample. For good collimation, it is important that the sample is in the focus of the terahertz beam and that it is oriented perpendicular to the direction of the incident terahertz beam.

After collimation, the reflected terahertz beam is reflected at the beam splitter (BS) and guided by an additional mirror (M) onto the same path as in the transmission setup.

With such a reflection TRTS setup the photo-conductivity and mobility of thin film can be derived even for highly conductive substrates such as metals, which is detailed in Section 5.2.

4.3 Measurement and Data Transformation

The aim of a TRTS measurement is to derive the relative change $\Delta E/E_{un} = (E_{ex}-E_{un})/E_{un}$ between the electric field E_{un} of the terahertz pulse, which propagates through (reflects from) the un-excited sample and the electric field E_{ex} of the terahertz pulse which propagates through (reflects from) the pump-excited sample.

Here, it will be detailed how this quantity $\Delta E/E_{un}$ is derived from the lock-in technique from the current of the photodiodes. Then it will be shown how the transient and the pulse shape are derived by scanning the pump delay time t_{pump} and the terahertz delay time t_{THz}, respectively.

4.3.1 Double-modulation Lock-in Detection

A TRTS measurement is based on the current of the balanced photo-diodes, which is proportional to the electric field of the terahertz pulse that overlaps in the ZnTe crystal with the sampling pulse. This electric current is digitalized in our setup by a data acquisition card.

To reduce the noise in the TRTS measurement the terahertz beam is modulated by an optical chopper. The digitalized signal of the photo-diodes is analyzed in a digital lock-in for the modulation frequency of the terahertz beam and yields the signals X_{THz}. This measured signal X_{THz} is also proportional to the electric field E of the terahertz pulse. The exact amplitude of E in units of V/cm does not have to be determined because in the desired ratio ΔE/E the unknown factor in E and ΔE cancels out.

The pump induced change ΔE can be retrieved by measuring the signals X_{THz} for the pump-excited sample and for the non-excited sample. Such a measurement is shown in Figure 4.5.

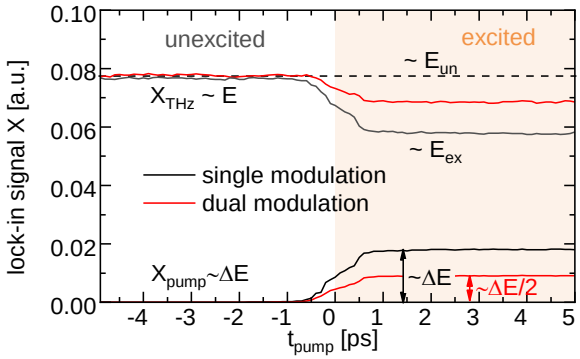

***Figure 4.5: Lock-in detection and signal restoration**. The lock-in signal at the modulation frequency of the pump beam X_{pump} and at the modulation frequency of the pump beam X_{THz} for the unexcited sample (negative pump delays $t_{pump}<0$) and for the photo-excited sample ($t_{pump}>0$). The electric field for the unexcited sample E_{un} is derived by adding X_{THz} and X_{pump}. The pump-induced change ΔE in the electric field is derived from X_{pump} for exclusive modulation of the pump beam and from twice X_{pump} for dual modulation of the pump beam and the terahertz beam. Data was measured on a compensated InP wafer excited with $9x10^{12}$ photons/cm^2/pulse at 800 nm.*

For negative pump delay times t_{pump} the pump pulse arrives after the terahertz pulse at the sample and the terahertz pulse probes a non-excited sample. At such times, X_{THz} is proportional to the electric field E_{un} of the terahertz pulse that interacted with the un-excited sample.

For positive pump delay times t_{pump} the pump pulse arrives before the terahertz pulse at the sample and the terahertz pulse probes an excited sample. At such times X_{THz} is proportional to the electric field E_{ex} of the terahertz pulse that interacted with the photo-excited sample.

The pump-induced change ΔE is proportional to change in X_{THz} between both regimes.

However, the pump induced change ΔE can be measured directly for positive pump delay times without shifting the delay time t_{pump} if the pump beam is modulated. Then, the signal of the balanced photo-diode is analyzed by the digital lock-in at the modulation frequency of the pump beam and yields the signals X_{pump}. This signal is proportional to ΔE.

However, deriving ΔE by pump modulation contains an ambiguity. Due to the nature of the lock-in technique, it is not always obvious whether ΔE is positive or negative. Usually, the phase between measured photo-diode signal and reference signal of the modulator is locked at the beginning of the measurement in such a way that the pump-induced signal X_{pump} is by default positive (or negative). The true sign of the ΔE can be revealed by the increase or decrease of the terahertz signal X_{THz}. Usually, ΔE is negative for transmission measurements and positive for reflection measurements.

In our setup, the terahertz beam and the pump beam are usually modulated simultaneously. This dual modulation approach [54] allows to simultaneously measure both signals X_{THz} and X_{pump} at the same delay times and therefore, reduces the impact of laser drift or other pink noise.

However, the double modulation alters the derived signals X_{THz} and X_{pump} which has to be corrected as shown in Figure 4.5.

The measured pump-induced signal X_{pump} has only half of the amplitude (other factors are possible [54]) compared to the situation where only the pump beam is modulated. Also, the measured terahertz signal X_{THz} exhibits only half the signal reduction between the un-excited and the excited regime.

From these considerations follows that for dual modulation $E_{un} \sim X_{THz} + X_{pump}$ and $\Delta E \sim 2X_{pump}$. The desired relative change $\Delta E/E_{un}$ is derived by:

$$\frac{\Delta E}{E} = \frac{2X_{pump}}{X_{pump} + X_{THz}} \tag{4.1}$$

4.3.2 Time Transformation of 2D Data

The electric fields E_{un} and ΔE are measured by TRTS for a specific terahertz delay time t_{THz} and pump delay time t_{pump}. These delays define which temporal part of the terahertz pulse is sampled in the ZnTe crystal and at which time the sample is probed with respect to its photo-excitation. A scan of these delay times yields the shape of the terahertz pulse and the transient behavior of the photo-excitation, respectively.

Such a full 2D data set of ΔE is shown in Figure 4.6a/b on the example of a $Cu_2ZnSnSe_4$ thin film measured by transmission TRTS. A 1D transient cut and a 1D pulse cut are shown in Figure 4.6c/d.

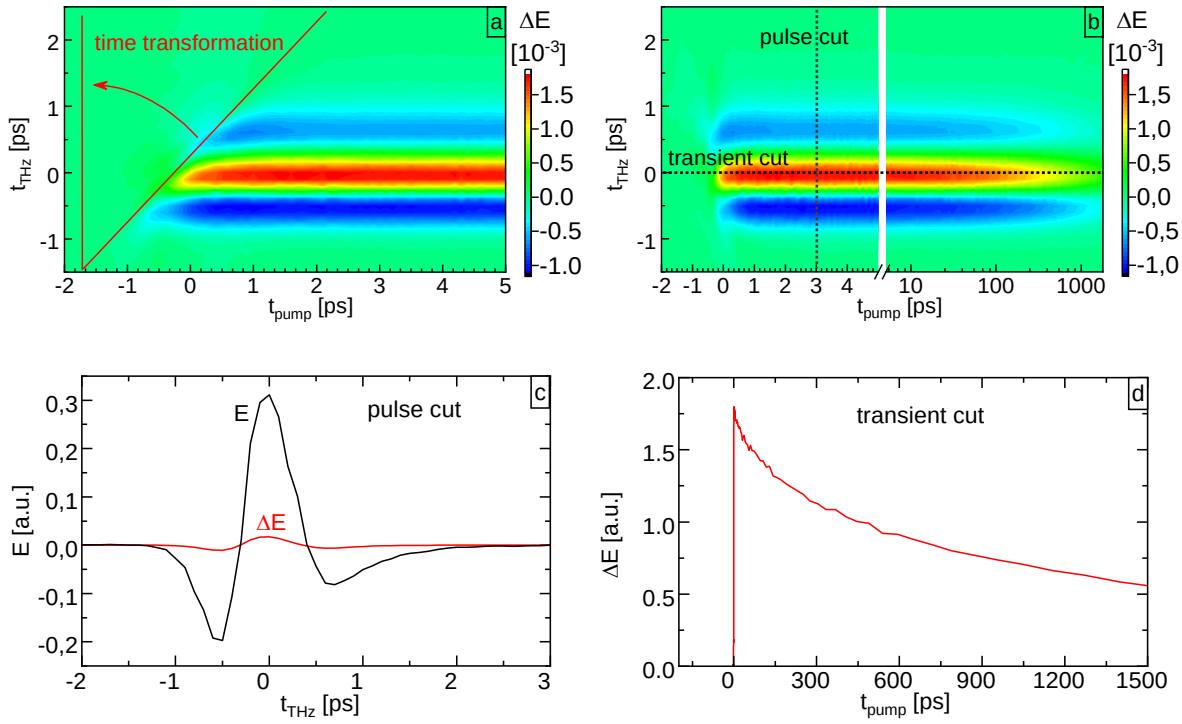

Figure 4.6: Time transformation of 2D data. *a) The pump-induced change in the electric field of the terahertz pulse ΔE is measured as a function of terahertz delay t_{THz} and of the pump delay t_{pump}. A time transformation is performed to minimize the effect of different sample excitation for the front and the back of the terahertz probe pulse. b) Data has been transformed by t_{pump}=t_{pump}-t_{THz}. c) The pulse cut along a constant pump delay can be analyzed for the frequency-dependent photo-conductivity. d) The transient-cut yields the transient of the photo-conductivity. The data was measured by transmission TRTS on a $Cu_2ZnSnSe_4$ thin film.*

The time-axis of the 2D data set depends on which of the three pulses – terahertz, sampling, and pump – are scanned by the TRTS setup. In our case, where the pump and the terahertz pulse are delayed, the data needs some further processing before the pulse cut can be analyzed.

For very short delays between the terahertz pulse and the pump pulse, the situation arises that the pump pulse excites the sample while already half of the terahertz pulse has passed the sample. Hence, the front of the terahertz pulse probes an unexcited sample and the back of it probes a photo-excited sample. This effect can be seen in Figure 4.6a where the front (negative t_{THz}) shows an earlier pump induced signal ΔE (at negative t_{pump}) than the back of the terahertz pulse (positive t_{THz}). To some degree, this issue can be overcome by a time transformation $t_{pump} \rightarrow t_{pump}$-$t_{Thz}$ [55]. Such a transformation leads to Figure 4.6b and corresponds to a simultaneous delay of the terahertz pulse and the pump pulse when the terahertz pulse is sampled. Another approach is the double Fourier analysis, which will not be applied in this work [56].

However, such a transformation is only required if the pulse cut is analyzed for pump delays smaller than the terahertz pulse length of ca. 3 ps or if the pulse cut is analyzed for very fast pump-induced

kinetics. The data measured in Figure 4.6a/b yields essentially the same pulse cut with and without time-transformation for pump delays larger than 3 ps.

A full scan of the pump delay and of the terahertz delay are relative time intensive. For example, the measurement of the data of Figure 4.6a took 6 hours. Therefore, measurements are usually taken along the “transient cut” or the “pulse cut”.

The “pulse scan” is recorded at a fixed pump delay t_{pump} which is usually chosen in this work to be at 10 ps after excitation. At such a delay time the “pulse cut” can be taken without the time-transformation and the initially photo-excitation of the sample has usually not decayed so far. In the next section, it will be shown how such a “pulse cut” can be analyzed for fundamental transport properties such as the transport effective mass, the effective scattering time of charge carriers and the localization parameter. The full data set in Figure 4.6 allows to analyze the kinetics of these properties and can reveal for example the thermalization and localization of charge carriers on the picosecond time scale, which will be shown in Section 6.2.

The “transient scan” is recorded at a fixed terahertz delay t_{THz}, which is usually chosen to correspond to the maximum of the pump-induced signal ΔE. In the next section, we will show that such a “kinetics cut” corresponds to the transient of the pump-induced photo-conductivity.

4.3.3 Pulse Scan and its Fourier Transformation

The TRTS setup measures the shape of the terahertz pulse the same way as a static time-domain terahertz spectrometer. It scans the electric field E of a terahertz pulse while the terahertz pulse is delayed with a delay stage by a time t_{THz}. Thereby the sampling pulse samples the electric field of the terahertz pulse and the temporal shape of the terahertz pulse is derived. Simultaneously its pump induced change ΔE is recorded as shown for the example of an InP wafer in Figure 4.7a.

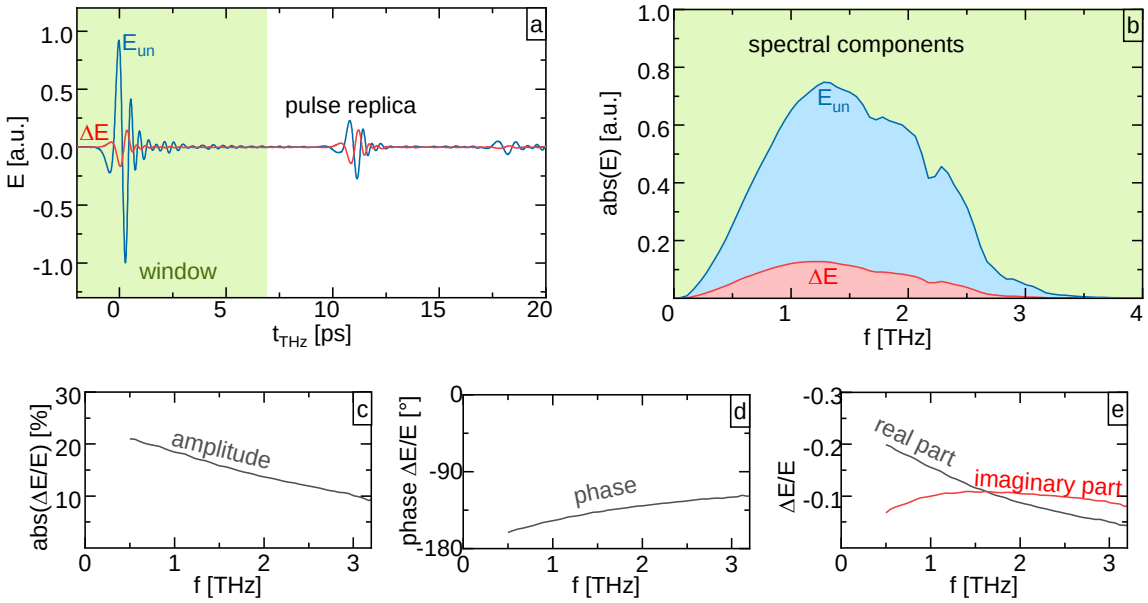

Figure 4.7: Sampled terahertz pulse. *a) The main terahertz pulse E and its pump-induced change ΔE are followed by replicas, which are cut off by a window function. b) The spectrum of the main terahertz pulse within the window function. c) Amplitude of the relative pump-induced change ΔE/E. d) Phases of the relative pump-induced change ΔE/E. e) Real and imaginary part of the relative pump-induced change ΔE/E. Measured with transmission TRTS on an InP wafer.*

The main terahertz pulse is followed by a train of replicas. These replicas originate from reflections in the ZnTe crystals, or in the silicon plates or in the sample. For data analysis, a window function is applied to neglect these pulse replica. A larger thickness of the optical elements can increase the time spacing between the main pulse and its replica and allows to use larger windows.

The terahertz pulse in the time window can be Fourier-transformed in $t_{THz} \rightarrow f$, which yields the spectral components of the terahertz pulse shown in Figure 4.7b. For our setup frequencies between ca. 0.5 and 3 THz are present in the terahertz probe pulse. The application of a window function is also beneficial for the Fourier transformation as it reduces artifacts due to the non-periodicity of the pulse.

For the analysis the relative change *ΔE/E* is desired, which is shown in Figure 4.7c-e.

Its amplitude in Figure 4.7c shows that low-frequency terahertz radiation is more affected by the optical-excitation of the InP sample than high-frequency terahertz radiation. Such behavior is often observed and can be explained by free carrier absorption, which is more effective at lower frequencies. This dependency also explains the superiority of terahertz spectroscopy over near infra-red spectroscopy which uses light with much higher frequencies and yields much lower signals from free carrier absorption.

The phase of *ΔE/E* in Figure 4.7d is close to -180° at low frequencies, which shows that the signal is dominated by a pump-induced reduction of the terahertz pulse. For higher frequencies, the phase

increases towards -90°, which corresponds to a delay of the terahertz pulse and can be explained by the pump-induced increase in the refractive index.

However, in the TRTS community, it is prevalent to state the pump-induced change as real and imaginary part instead of the amplitude and phase, which are shown in Figure 4.7e and contain the same information.

4.3.4 Transient Scan and its Correction

The TRTS setup can measure the transient of the pump-induced change in the measured terahertz pulse ΔE. To this end, the pump pulse is delayed with a delay stage by the time t_{pump}. However, before it can be analyzed for the kinetics in the photoconductivity, it has to be correct for two artifacts that are connected to the divergence or movements of the pump spot and to the emission of terahertz radiation.

A divergence or a movement of the pump spot causes a change in its intensity at the location of the overlap with the terahertz probe pulse. Subsequently, also the pump-induced signal ΔE changes. Even after careful alignment of the pump beam, these effects cannot always be completely overcome.

However, this issue can be overcome by using a reference sample that has a charge carrier lifetime far beyond the time window of the TRTS measurement (1.8 ns for our setup). For such a sample the transient signal ΔE should be constant over time. However, Figure 4.8a shows that the measured transient of a passivated silicon wafer can even increases over time due to the movement of the pump spot. However, this transient can be used as a reference for a constant signal and other transients can be calibrated by that transient as shown in Figure 4.8a.

Additionally, a pump-induced signal ΔE can also be detected when the sample is not probed by a terahertz pulse. This terahertz signal originates from the terahertz emission of the sample. Such emission can be caused by the photo-Dember effect, charge carrier acceleration electric fields or by non-linear optical effects [57]. The terahertz emission allows to probe these processes and in Section 6.2 the terahertz emission will be used to reveal the transition from bipolar to ambipolar diffusion of charge carriers.

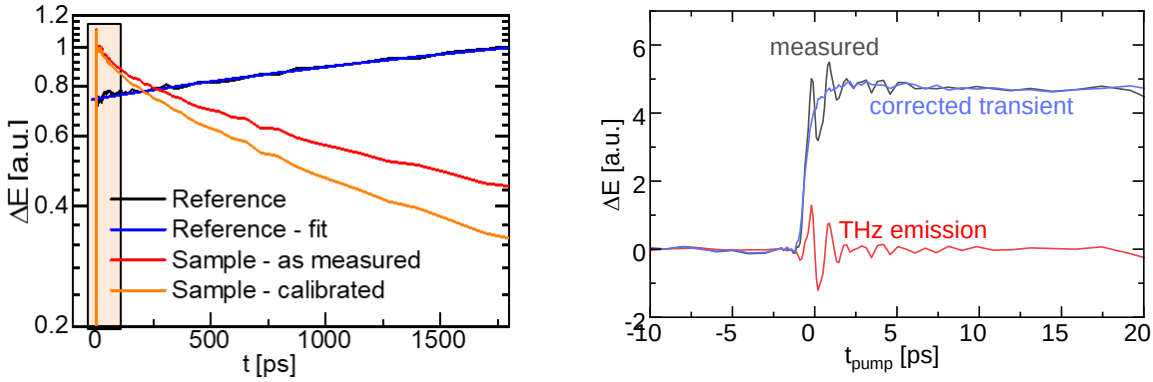

Figure 4.8 Correction of the TRTS-transient. *a) TRTS-transient measured on a reference sample (passivated silicon wafer) that should exhibit a constant signal but increases due to miss alignment of the pump pulse. This transient is used as a reference for a constant signal and is used to correct other transients ($Cu_2ZnSnSe_4$ thin film) b) Pump-induced THz emission is measured with a blocked THz probe pulse and superimposes on the measured TRTS-transient ($CsPbI_3$ thin film). The corrected transient is derived by subtracting the THz emission.*

However, the terahertz emission superimposes on the ΔE signal that originates from the transient photoconductivity. If the later one is of interest the terahertz emission should be removed by subtracting the ΔE signal that is measured without the terahertz probed pulse as shown in Figure 4.8b.

Further, it will be shown that the photoconductivity is only directly proportional to ΔE for relatively small changes. Otherwise, $\Delta E/E$ should be used and its precise dependency on the photoconductivity, which will be derived by the transfer matrix method in Section 4.4.3 or by the corresponding thin-film approximations in Section 4.4.4.

4.4 Analysis

The relative pump-induced change $\Delta E/E$ of the transmitted or reflected terahertz pulse contains the information about the pump-induced photoconductivity and subsequently about the change carrier mobility μ and the transient photo-excited charge carrier concentration Δp. In the following, the relation between $\Delta E/E$ and these properties will be derived.

To this end, one can either use the rather complex transfer matrix approach or its simple thin-film approximations (TFA) which are illustrated in Figure 4.9. The great advantage of the TFA is that they are analytical equations, which efficiently yield the mobility or the photoconductivity. Usually, the approximations, which are a homogeneous photo-excitation of the thin film and a film thickness fare below the wavelength of the terahertz pulse, introduce an error of less than 5 %. However, the limitations of the TFA are not always clear and in Section 5.2 it will be shown that they are not valid for thin films on conductive substrates.

In such a case the transfer matrix method has to be used, which can model very complex sample geometries, the excitation profile and the yields the “exact” results. On the downside it is a rather complex numerical approach. However, once the transfer matrix approach is efficiently implemented in a software it analyzes a full TRTS pulse cut typically within a second.

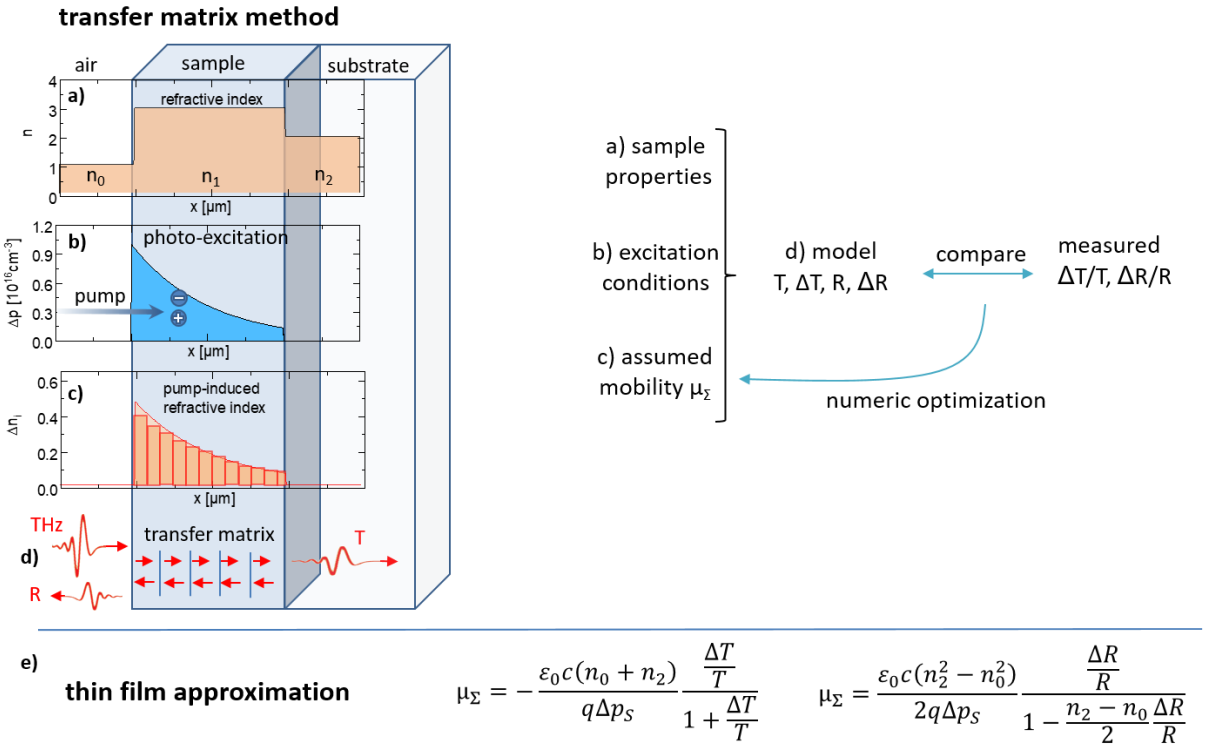

Figure 4.9: Analysis modes of TRTS. *Numerical transfer-matrix-approach in .a-d) vs. simple thin-film-approximation in e). a) The thicknesses and the refractive indices n of the sample layers define the transmission T and reflection R of the non-excited sample. b) The pump pulse excites a charge carrier distribution Δp(x), which leads in c) to a pump-induced change in the refractive index Δn. This spatial distribution is discretized into several homogeneous layers. d) Modeling of the transmission T and reflection R with the transfer matrix method.*

Figures 4.9a-d show the main steps of the transfer matrix approach for the example of a typical thin film on an optically thick substrate.

To model the pump-induced change in the transmission coefficient *ΔT/T* (or in the reflection coefficient *ΔR/R*) of the terahertz pulse, the transmission coefficient (or reflection coefficient) of the non-excited sample as well as on the photo-excited sample have to be derived. It should be noted, that here the transmission and reflection coefficients are label by “R” and “T” instead of the prevalent “r” and “t” to distinguish them from the time t.

To this end, the refractive indices and thicknesses of the individual layers have to be known. Figure 4.9a shows exemplary the refractive indices of the non-excited sample layers. This refractive indices at terahertz frequencies will be discussed in Section 4.4.1.

The photo-excitation of the sample is modeled in Figure 4.9b. The initial photo-excited charge carrier concentration Δp decreases with its absorption coefficient into the bulk of the sample.

The photo-excited charge carriers induce an absorption and a changed refractive index Δn of the sample. This photo-induced refractive index can be calculated based on the mobility of the photo-induced charge carriers, which will be detailed in Section 4.4.2. In the transfer matrix approach, this mobility is initially guessed. The spatial variation of the refractive index is modeled by a step-like decay of multiple-layers as shown in Figure 4.9c.

Based on the non-excited and on the photo-excited refractive indices the transmission and reflection of the terahertz pulse can be modeled by the transfer matrix method, which accounts for all internal reflections as illustrated in Figure 4.9d and will be detailed in Section 4.4.3.

Finally, the modeled photo-induced change in transmission coefficient $\Delta T/T_{un}$ (or reflection coefficient $\Delta R/R_{ex}$) can be compared to the values that were measured by TRTS. Numerical minimization of their deviation for instance by a simplex-algorithm optimizes the value of the assumed charge carrier mobility.

4.4.1 Refractive Indices at Terahertz Frequencies

The first step to analyze TRTS data quantitatively is to model the transmission (or reflection) of the terahertz probe pulse of the un-excited sample, which is given by the geometry of the sample and the refractive indices of the layer.

The complex refractive indices n or dielectric functions $\varepsilon = n^2$ can be measured by time-domain terahertz spectroscopy, which can be performed with the TRTS setup [44]. To this end, the terahertz pulse with and without the sample is measured. Its attenuation and delay due to the presence of the sample can be modeled by the transfer matrix method which derives the reactive index of the probed material.

The refractive indices n_{THz} and absorption coefficients α_{THz} in the terahertz regime for common substrates such as glass, quartz, silicon, Al_2O_3, and molybdenum are shown in Figure 4.10a/b. These were measured together with InP by time-domain terahertz spectroscopy.

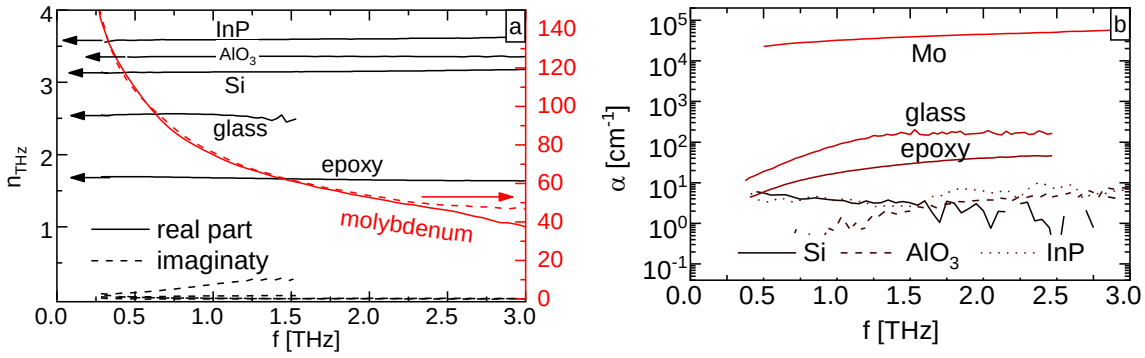

Figure 4.10: Refractive index in the terahertz regime. *a) The real and imaginary part of the refractive index for some common substrates and thin-film materials. b) Corresponding absorption coefficient in the terahertz regime.*

However, in Section 4.4.3 it will be shown that the refractive index of a thin film has no impact on the results within the so-called thin-film approximation. Therefore, often it is sufficient to know the refractive index of the substrate and of the surrounding medium, which in our setup is nitrogen with a refractive index of 1.

4.4.2 Photo-induced Terahertz Absorption

The photo-excitation of the sample changes the reflection and transmission of a terahertz pulse. The physical explanation for this phenomenon is a change in the complex refractive index due to the pump-induced photoconductivity. This dependency will be detailed in the following.

The photon flux ϕ_{Ph} of the pump-pulse is absorbed in the sample and photo-excites electrons and holes in the probed sample. The photo-excited charge carrier concentration Δp follows the Lambert-Beer absorption law and decays exponentially with the absorption coefficient α into the bulk of the sample.

$$\Delta p(x) = \phi_{ph}(1-R)\alpha\, exp(-\alpha x) \tag{4.2}$$

These photo-excited electrons and holes have a certain mobility μ_e and μ_h, respectively, and induce a photoconductivity $\Delta\sigma$ in the sample. The photo-excited charge carriers can be divided into more categories for example for trapped and free. Therefore, the mobility μ_Σ is an effective value averaged over all pump induced charge carrier species and corresponds to the sum of the average electron mobility and of the average hole mobility.

$$\Delta\sigma(x) = e(\mu_e + \mu_h)\Delta n(x) = e\mu_\Sigma \Delta n(x) \tag{4.3}$$

From the Maxwell equations follows that the dielectric function ε of a material has a contribution from its conductivity. The dielectric function ε_{un} of the non-excited material is altered to the dielectric function ε_{ex} of the photo-excited material by the photo-excited conductivity $\Delta\sigma$:

$$\varepsilon_{ex} = \varepsilon_{un} + i\frac{\Delta\sigma}{\omega\varepsilon_0} \tag{4.4}$$

The pump-induced change in the dielectric function is inversely proportional to the angular frequency $\omega = 2\pi f$.

Equation (4.4) can also be expressed in terms of the complex refractive index $n = \varepsilon^{0.5}$ of the non-excited materials n_{un} and of the photo-excited material n_{ex} in Equation (4.5). For example, the increase of the refractive index with the conductivity of the material is responsible for the high reflection of metals and their application as mirrors. This behavior can be seen in Figure 4.10a on the example of molybdenum.

$$n_{ex} = \sqrt{{n_{un}}^2 + i\frac{\Delta\sigma}{\omega\varepsilon_0}} \approx n_{un} + i\frac{1}{2\omega\varepsilon_0 n_{un}}\Delta\sigma \tag{4.5}$$

For minor changes in the refractive index, a Taylor expansion yields the right side of Equation (4.5), which states that the photo-conductivity mostly induces an imaginary refractive index n_i. It corresponds to the absorption coefficient $\alpha = 2\omega n_i/c$ and therefore the signal is dominated by an induced absorption for small pump-induced conductivities.

$$\Delta\alpha \approx \frac{\Delta\sigma}{c\varepsilon_0 n_{un}} \tag{4.6}$$

4.4.3 Transfer Matrix Method

Now the measured quantity, the relative pump-induced change $\Delta E/E$ in the transmitted or reflected terahertz pulse, can be connected to the pump-induced change in the complex refractive index.

To this end, the transmission and reflection of a terahertz pulse (or light in general) can be computed by the transfer matrix method [58] [26]. This method is based on the Fresnel equation and is capable of modeling the coherent interferences of multi-layer systems.

The method connects the electric fields (or intensities for non-coherent light) of the right going wave E and the left going wave E' at the interfaces of the sample. For each layer and interface of the sample a matrix A_i can be defined that connects the electric field before it E_0 and after it E_{end}. If the beam passes through many elements the overall transfer matrix is the product of the individual matrixes. Thereby it accounts for all internal reflections.

$$\begin{pmatrix} E_0 \\ E'_0 \end{pmatrix} = A \begin{pmatrix} E_{end} \\ E'_{end} \end{pmatrix} = \prod_{i=1}^{end} A_i \begin{pmatrix} E_{end} \\ E'_{end} \end{pmatrix} = \begin{pmatrix} a_{11} & a_{12} \\ a_{21} & a_{22} \end{pmatrix} \begin{pmatrix} E_{end} \\ E'_{end} \end{pmatrix} \tag{4.7}$$

Relevant transfer matrixes are on one hand side the propagation matrix *P* through a homogenous medium:

$$P = \begin{pmatrix} exp\left(-i\frac{n_1\omega}{c}z\right) & 0 \\ 0 & exp\left(i\frac{n_1\omega}{c}z\right) \end{pmatrix} \tag{4.8}$$

On the other hand side, it is the interface matrix *I* that connects the fields before the interface to the field after it. This matrix is based in Equation (4.9) on the Fresnel equations for normal incidence.

$$I = \frac{1}{2n_0}\begin{pmatrix} (n_0 + n_1) & (n_0 - n_1) \\ (n_0 - n_1) & (n_0 + n_1) \end{pmatrix} \tag{4.9}$$

The overall matrix of a layer-system is the alternating product of interface and propagation matrixes.

The transmission coefficient *T* and reflection coefficient *R* of a layer-system that is described by a transfer matrix *A* can be derived from Equation (4.10). To this end, it is assumed that no radiation is incident from the backside of the sample: $E'_{end} = 0$.

$$t = \frac{E_{end}}{E_0} = \frac{1}{a_{11}} \qquad\qquad r = \frac{E_0'}{E_0} = \frac{a_{21}}{a_{11}} \tag{4.10}$$

The transmission (or reflection) can be calculated for the un-excited sample T_{un} (R_{un}) and for the photo-excited sample T_{ex} (R_{ex}). In combination, they yield the relative pump-induced change $\Delta E/E_{un}$ in the transmitted or in the reflected terahertz pulse.

$$\frac{\Delta E}{E_{un}} = \frac{R_{ex}}{R_{un}} - 1 \qquad or \qquad \frac{\Delta E}{E_{un}} = \frac{T_{ex}}{T_{un}} - 1 \tag{4.11}$$

These values are based on an assumed photoconductivity (or mobility) and can be compared to the measured relative pump-induced change $\Delta E/E_{un}$ in the transmitted or reflected terahertz pulse. The "real" photoconductivity (or mobility) is derived when the difference between computed and the measured relative pump-induced change $\Delta E/E_{un}$ is minimized. To this end, a Neader-Mead simplex algorithm is used.

The advantage of the transfer matrix method is that it can analyze samples with a complicated layer structure.

It also offers the possibility to model inhomogeneous layers such as photo-excited layers with a spatial distribution of the photo-excited change in the refractive index. An inhomogeneous layer can be divided into a series of very thin homogenous layers as was shown in Figure 4.9d. Therefore, the photo-

induced refractive index which decays into the depth of the sample can be modeled. Also other inhomogeneous carrier distributions such as diffusion and surface recombination could be included in the model.

4.4.4 Thin Film Approximations

For simple sample geometries, the relation between the pump-induced photoconductivity $\Delta\sigma$ and the pump-induced signal $\Delta E/E_{un}$ can be approximated analytically. Such a common geometry is a surrounding medium, the semiconductor thin film under probe and an optically thick substrate.

The transfer matrix of such a system contains the air-to-sample interface, propagation through the sample thin film and the thin film-substrate interface. The substrate is assumed to be thick enough such that reflections at the substrate-air interface can be cut off by a window function.

Two approximations are required to derive analytical equations from such a transfer matrix analysis. First, the distribution of excited charge carriers is approximated by a homogeneously excited layer. Second, the exponential terms in the propagation matrixes are approximated by a second-order Taylor expansion. This approximation is justified as long as the layer thickness is much smaller than the terahertz wavelength (1 THz ≙ 300 µm). Due to this second criterion, the following approximations are called “thin-film approximations”.

For the transmission mode, the measured pump-induced change in the terahertz pulse $\Delta E/E_{un} = \Delta T/T$ is connected in equation (4.12) to the pump-induced sheet photoconductivity $\Delta\sigma_S$ by the vacuum dielectric constant ε_0, by the speed of light c and by the refractive indices of the medium in front of the sample n_0 and of the substrate n_2 [59]. It should be noted, that ΔT is usually negative if defined as in Equation (4.11).

$$\Delta\sigma_S = -\varepsilon_0 c(n_0 + n_2)\frac{\frac{\Delta T}{T}}{1+\frac{\Delta T}{T}} \tag{4.12}$$

Interestingly, the refractive index of the sample cancels out of the approximation. Such behavior is very handy as the refractive indices of novel materials are often unknown. In contrast, the refractive indices of common substrates are well-known as shown in Figure 4.10a.

For the reflection a similar equation can be derived [50] [51] [52] [53]. It should be noted, that ΔR is usually positive if defined as in Equation (4.11).

$$\Delta\sigma_S = \frac{\varepsilon_0 c(n_2^2 - n_0^2)}{2} \frac{\frac{\Delta R}{R}}{1 - \frac{n_2 - n_0}{2}\frac{\Delta R}{R}} \tag{4.13}$$

4.4.5 Separation of Charge Carrier Mobility and Concentration.

The derived photo-induced sheet conductivity $\Delta\sigma_S$ is determined by the photo-excited sheet carrier concentration Δp_S, the sum of the electron mobility and the hole mobility μ_Σ and the elementary charge q.

$$\Delta\sigma_S = q\mu_\Sigma \Delta p_S \tag{4.14}$$

It is prevalent to state equations (4.12) and (4.13) for the conductivity $\Delta\sigma$ and charge carrier concentration p, which are assumed to be homogenously distributed over the layer thickness or over the absorption depth $1/\alpha$. However, within the thin-film approximation, the specific spatial distribution of the charge carrier does not affect the pump-induced signal. Hence, only the integrals of $\Delta\sigma$ and p over depth are of relevance, which are the photo-induced sheet conductivity $\Delta\sigma_S$ and the photo-excited sheet carrier concentration Δp_S .

This concentration is known right after excitation. The initially induced carrier concentration is given by the incident pump photon flux per pulse ϕ_{Ph} and by its reflection R_{pump} at the sample and transmission T_{pump} through the sample.

$$\Delta p_S(t=0) = \int_0^d \Delta p(x)dx \; = \phi_{ph}\left(1 - R_{pump} - T_{pump}\right) \tag{4.15}$$

If the sample is probed shortly after pump-excitation, the induced sheet carrier concentration has not decayed so far and the sum of the electron mobility and the hole mobility μ_Σ is derived by equations (4.13-15).

For later times the photo-conductivity decays and ab initio it is not clear wheatear the charge carrier concentration or the charge carrier mobility decays over time. The former process is usually associated with charge carrier trapping and localization (or a plasmonic resonance discussed in Section 2.4) and the later one with charge carrier recombination, which was introduced in Section 2.3. However this ambiguity is lifted by the frequency-dependence of the photo-conductivity, which originates from the frequency-dependence of the mobility: If the frequency-dependence of the photoconductivity changes over time, then the decay of the photoconductivity is at least partially caused by a changing mobility. If the frequency-dependence of the photoconductivity does not change over time, then the decay is can be assigned to charge carrier recombination.

5 Verifying and Advancing TRTS on Photovoltaic Samples

TRTS is a relatively complex and new method to the photovoltaic community. Therefore, it is often questioned if it yields reliable results on photovoltaic samples. These concerns are addressed throughout this chapter in three aspects.

In Section 5.1 the TRTS measurement modes, transmission and reflection geometry, and the analysis modes, thin-film approximation and transfer matrix method, are experimentally compared on an InP wafer. It will be shown that they yield similar results within a maximum deviation of 15 % and that the derived values are in line with the literature.

In Section 5.2, the TRTS will be tested on thin films that are deposited on conductive substrates, which is the prevalent sample architecture in photovoltaics. It will be shown that the thin-film approximation fails for such samples. However, the transfer matrix method is validated and yields similar results as measured for samples on insulating substrates.

In Section 5.3, the TRTS measurement will be compared to the dynamics in an operating solar cell and to alternative techniques that are more established in the photovoltaic community. The differences between the techniques will be summarized and experimentally demonstrated on a $Cu_2ZnSnSe_4$ thin film.

The theoretical background of this chapter was introduced in Chapter 4.

5.1 Measurement and Analysis Modes

A comparison of the TRTS measurement and analysis modes has been performed sparely in literature. It was shown that the transfer matrix method deviates from the TFA by ~5 % for TRTS measurements in transmission mode [55]. However, a comparison of transmission and reflection measurements is not reported to our knowledge.

To this end, TRTS transients and mobilities were measured in reflection as well as in transmission geometry on an InP wafer. Such a wafer can be viewed as a photo-excited InP thin film on a thick un-excited InP substrate. Hence, the thin-film approximation as well as by the transfer matrix method should be appropriate to analyze the data.

Figure 5.1a shows that the derived mobility spectra are in close agreement, regardless of the measurement or analysis mode. The same agreement is found for the transients in Figure 5.1b. Regardless of the general validation of the TRTS modes on the InP wafer, such a double check is an excellent way to approve that the analysis methods and measurement modes are implemented

correctly in a specific setup or software. Important aspects that are easily missed are the correction of the measured data for double modulation, which was as described in Section 4.3.1, and the conversion of the measured transients *ΔT(t)* and *ΔR(t)* to the photoconductivity *Δσ(t)* by the corresponding TFA. This transformation is non-linear and leads to visible changes in the transients for *ΔT/T > 1 %*.

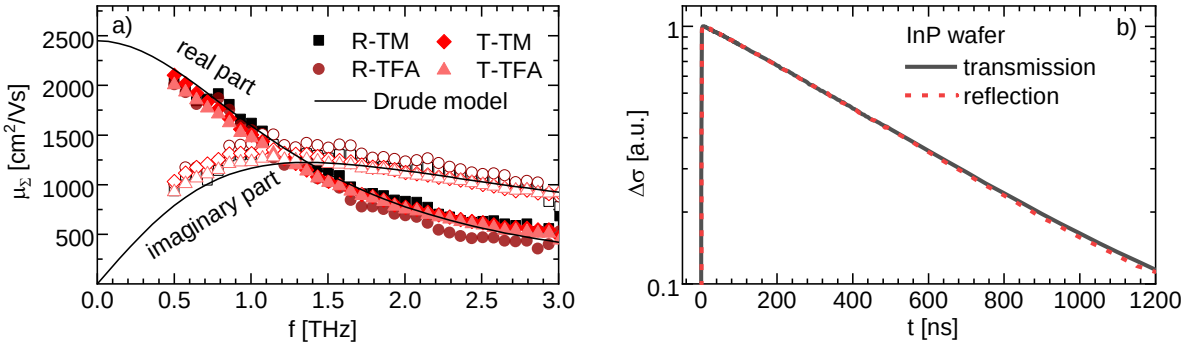

Figure 5.1: Consistency of TRTS. *a) Charge carrier mobility μ_Σ measured by transmission (T) and reflection (R) mode TRTS on an InP wafer and analyzed by the transfer matrix method (TM) and the thin film approximation (TFA). The frequency dependence is modelled by the Drude model which yields an effective mass of 0.084 in close agreement with literature. b) Transient photoconductivity measured by transmission and reflection mode TRTS agree on each other.*

Further, the measured mobilities in Figure 5.1a are modeled by the Drude-model of free charge carrier transport (section 2.4.2). It yields a scattering time of 117 fs, an effective mass of 0.084 and a DC-mobility of 2400 $cm^2/V/s$. The mobilities of the holes in InP are relatively small < 200 cm^2/Vs and contribute less than 10 % to the TRTS-derived sum mobility [60]. Therefore, the sum mobility in Figure 5.1a and the derived effective mass are dominated by the electron. This measured effective mass of 0.084 is in close agreement with literature values of the electron effective mass InP, for which values of ~0.077 are reported at room temperature [60]. This finding further validates the measurement of mobilities by TRTS and estimates an uncertainty of ~ 10 %.

Such a measurement of the effective mass can also be used to calibrate TRTS setups, as the effective mass is characteristic for materials and often known from other techniques. In contrast, the scattering time and the amplitude of the mobility are rather sample-specific, as they depend for example on the ionized impurity scattering and therefore on the defect concentration in the specific sample.

5.2 TRTS of Thin Films on Conductive Substrates

Photovoltaic materials are usually deposited on conductive substrates, which are used as electric back contact in a solar cell. However, no literature was found, that applied TRTS to thin-film samples on conductive substrates. Therefore, the measurement and analysis methods were tested on such

samples and it was found that the common thin-film approximation fails. This finding was published as the first-author in publication [3].

The first challenge in measuring thin films on conductive substrates by TRTS is that they strongly reflect and absorb terahertz radiation, which prohibits transmission TRTS. However, TRTS has been performed recently in several studies in reflection geometry [50] [51] [52] [53]. Such geometry was described in Section 4.2.3 and allows to probe opaque samples.

Here, reflection TRTS was probed on two $Cu_2ZnSnSe_4$ thin films that were grown on a molybdenum coated glass substrate and on a bare glass substrate. The sputtering of the metal precursors and their selenization were preformed by Alex Redinger at the Helmholtz Zentrum Berlin.

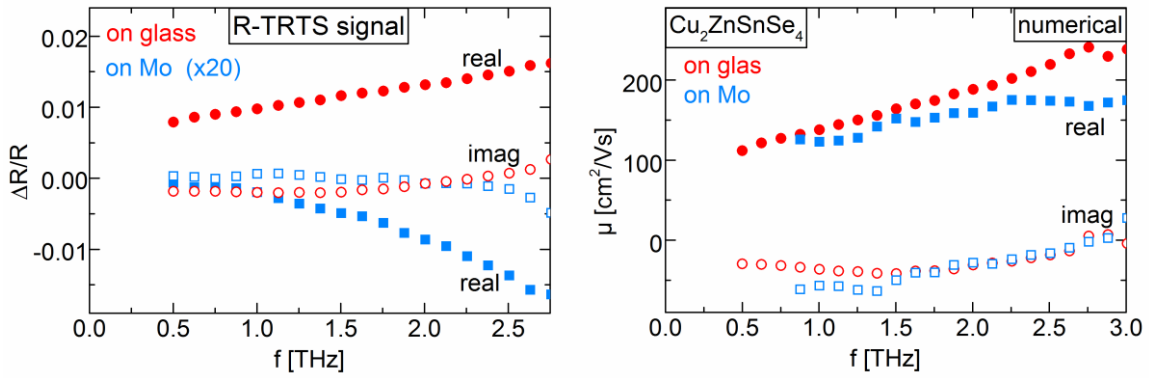

Figure 5.2: Thin films on metal substrates. *a) Pump-induced change in terahertz reflection ΔR/R measured for a $Cu_2ZnSnSe_4$ thin film on glass and on a molybdenum metal substrate. b) The transfer matrix method retrieves similar change carrier mobility from the data in a).*

The measured pump-induced change is shown in Figure 5.2. The amplitude, frequency-dependence, and sign of the pump induced reflection *ΔR/R* changes strongly between the molybdenum and the glass substrate. However, the analysis with the transfer matrix method - as described in Section 4.4.3 - derives similar mobility spectra from both measurements, which are in line with our former transmission TRTS measurements on $Cu_2ZnSnSe_4$ thin films [4]. This finding validates the application of the transfer matrix method and shows the superiority of TRTS over methods, such as Hall measurements, in which the measured transport would be dominated by the highly conductive substrate.

For the analysis of the TRTS data, it is crucial to use the correct refractive index of the metal substrate. Such a refractive index of a metal is governed by its conductivity contribution, which was described by Equation (4.5). It results in a very high and strongly frequency-dependent refractive index that was shown for molybdenum in Figure 4.10a.

To obtain this refractive index a 20 nm thick molybdenum film was deposited onto a quartz substrate, which was measured by time-domain terahertz spectroscopy. Such a time-consuming procedure can be circumvented when the conductivity/resistivity of the substrate is measured by a four-terminal setup. The retrieved conductivity can be used in Equation (4.5) to approximate the terahertz refractive index.

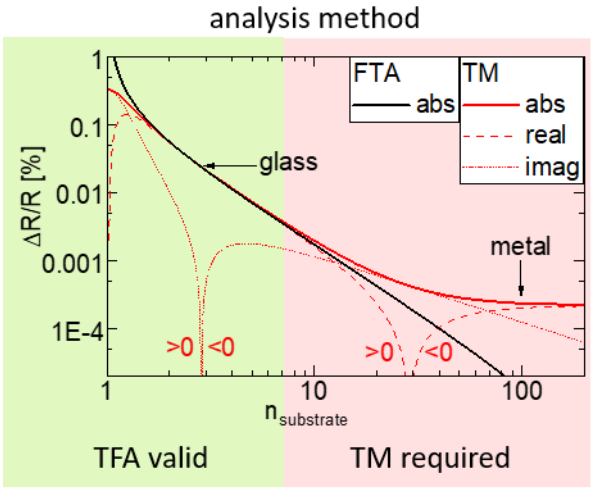

Figure 5.3: Validity of thin-film approximation (TFA). *Pump-induced change in terahertz reflection ΔR/R calculated by the TFA and by the transfer matrix method for a typical $Cu_2ZnSnSe_4$ thin film (d = 1 µm; n = 2.7; f = 1THz; $\phi_{Ph} = 4*10^{12}cm^{-2}$, µ = 100 cm^2/Vs, α = $4.4*10^4cm^{-4}$).*

Further, we found that the analysis with the thin-film approximation fails for reflection TRTS of thin films on conductive substrates. The deviation of the thin-film approximation (TFA) from the transfer matrix method (TM) was modeled in Figure 5.3. For substrates with a large refractive index, the TFA underestimates the amplitude of pump-induced change *IΔR/RI* and also does not reproduce its phase.

Additionally, the signal amplitude decreases strongly with an increasing refractive index of the substrate, which is shown in Figure 5.3. Such a behavior can be explained by the large reflection at the materials with a large refractive index. For a molybdenum substrate with $n \sim 100$, almost the entire terahertz pulse is already reflected on the un-excited sample. Therefore, the photo-excitation of the sample can only cause a minor change in the reflection of the terahertz pulse.

Finally, we estimated the resulting impact on the resolution of TRTS. In Figure 5.4 we model the amplitude of the pump induced reflection *ΔR/R* for a thin film on a metal substrate that is excited with a typical sheet carrier concentration of $4*10^{12}cm^{-2}$. It indicates which samples can be measured by our setup within a measurement time ranging from 1 minute to 1 day. Materials with relatively low mobility can be measured on metal substrates as long as their films are relatively thick. Such behavior is also in stark contrast to the thin-film approximation, in which the signal *ΔR/R* does not depend on the thickness of the thin film.

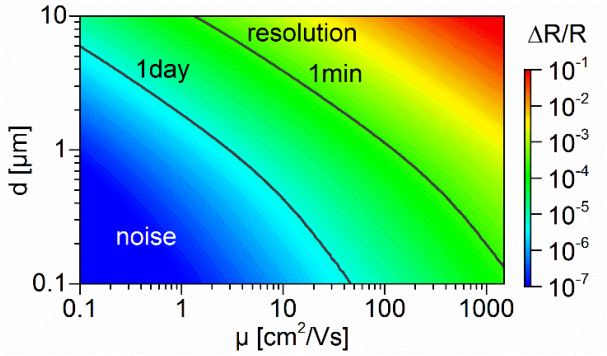

Figure 5.4: Sensitivity of reflection TRTS for thin films on a metal substrate. *Pump-induced change in terahertz reflection ΔR/R modeled by the transfer matrix method for a typical thin-film absorber (n = 2.7; f = 1THz; $\phi_{Ph} = 4*10^{12}cm^{-2}$, $\alpha = 4.4*10^{4}cm^{-4}$). The resolution of our TRTS setup is indicated for measurement times of 1 minute and 1 day.*

In conclusion mobility measurements in thin films on conductive substrates are possible by TRTS. However, they come with significant drawbacks compared to measurements on insulting substrates. These drawbacks include low signal amplitude, the requirement of the transfer matrix analysis and the dependence on the layer thickness of the thin film and on the conductivity of the substrate, which have to be measured additionally. For these reasons, it was more convenient in the following chapters to lift the thin films of their metal substrates and to measure them on an insulting and transparent epoxy substrate.

5.3 Alternative Techniques

The charge carrier transport and recombination can be probed by various methods, which in principle should support and validate each other. However, the charge carrier mobilities that are reported in the literature can differ significantly for different techniques on the same material [61], which causes controversial debates about the “correct” values. Therefore, TRTS will be compared here to such alternative techniques in detail. Their individual advantages and drawbacks will be briefly discussed. It will be shown that the individual techniques measure charge carrier mobility under different conditions, which explains their deviations. Further, it is important to understand the differences compared with the conditions in an operating solar cell if the results are interpreted in the light of application in photovoltaics. It should be noted, that the values given in the comparison of the techniques are typical values and do not correspond to high-end systems.

5.3.1 Transport Measurements

Common techniques to probe charge carrier transport and mobility are the analysis of the voltage-dependent internal quantum efficiency (V-IQE) of a solar cell; the combination of Hall and conductivity measurements (Hall) and time-resolved microwave conductivity (TRMC) measurements, which are

illustrated in Figure 5.5. These techniques will be compared by theory and experimentally throughout this section. TRTS was already introduced in-depth in Chapter 4. Parts of this compassion have been published in publication [4].

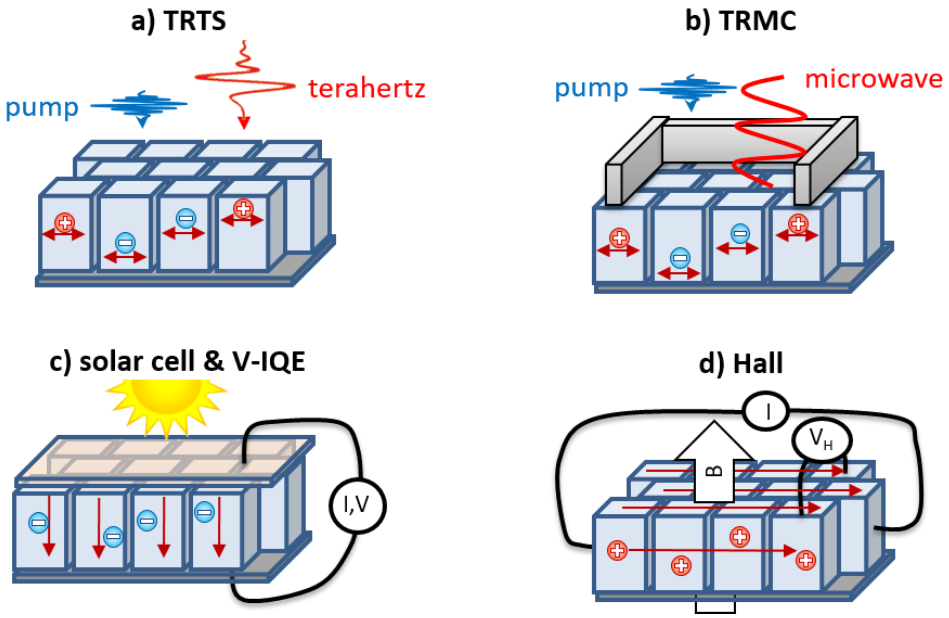

Figure 5.5: Illustration of transport measurements that derive a charge carrier mobility. *a) Time-resolved terahertz spectroscopy (TRTS). b) Time-resolved microwave conductivity (TRMC). c) The voltage-dependent internal quantum efficiency of a solar cell (V-IQE). d) Hall effect and conductivity measurement (Hall)*

Time-resolved microwave conductivity (TRMC) is in principle very similar to TRTS but uses a continuous microwave probe beam, which is guided by a cavity to the sample, instead of the free-space terahertz probe-pulse in TRTS [62] [63]. An optical pump-pulse photo-excites charge carriers, which are accelerated in the electric field of the microwave. Thereby the reflection of the microwave is altered which is measured and can be analyzed for the pump-induced photoconductivity.

The major advantage of TRMC is that it is more sensitive than TRTS, especially when the microwave is in resonance with the cavity length. However, TRMC yields the mobility only at a single frequency and therefore no information on the nature of transport is obtained. Further, no free space propagation feasible, which limits its mapping abilities.

The voltage-dependent internal quantum efficiency of a solar cell (V-IQE) measures the collection of charge carriers in a completed solar cell as illustrated in Figure 5.5c and requires a rather extensive series of supplementing measurements [64]. The solar cell is contacted and illuminated with a background equivalent to one sun. Additionally, monochromatic light photo-excites charge carriers and the external quantum efficiency of their collection is recorded as a function of excitation

wavelength and applied voltage [41]. The voltage-dependence allows distinguishing the carrier collection by drift in the space charged region and by diffusion in the neutral region, which were discussed in Section 3.3.1. Additionally, the reflection of light from the solar cell is measured, which allows deriving the internal quantum efficiency. This internal quantum efficiency can be modeled as a function of diffusion length, space charge region width and absorption coefficient. The absorption coefficient and the space charge region width are determined separately and the diffusion length is combined with a charge carrier lifetime, which is measured for example by TRTS or TRPL to derive the charge carrier mobility.

The main advantage of V-IQE is that it directly interprets the performance of the solar cell and therefore derives the charge carrier mobility under the relevant conditions. However, the main disadvantages of the V-IQE method are the extensive supplementary measurements that are required and that it has to be performed on a completed solar cell. If the solar cell is completed, photovoltaic performance has not to be estimated from the transport properties but could be measured straight away. Therefore, V-IQE is an excellent technique to verify other techniques and to examine if their derived mobility describes the transport in the solar cell correctly.

Hall and conductivity measurements (Hall) are very common combination to derive the charge carrier mobility in a semiconductor [65]. A Hall measurement is illustrated in Figure 5.5d. It detects the Hall voltage V that is generated by an electric current I which is deflected by a magnetic field B. The measured Hall voltage is proportional to the charge carrier concentration p (or n) in the sample and changes sign depending on the doping type. An additional four-terminal measurement of the conductivity $\sigma = qp\mu$ allows deriving the mobility μ of the majority charge carriers and the dark charge carrier concentration.

A major advantage of Hall measurements is that they yield not only the charge carrier mobility but also the doping concentration and the doping type of the samples. On the downside, the method requires the deposition of electrical contacts which opposes the mapping of combinatorial samples and high throughput screening. The technique also cannot measure the mobility in thin films on conductive substrates, which is the common sample geometry in photovoltaics.

Although all these different techniques derive the charge carrier mobility, the properties of the derived mobility and the measurement conditions can be very different as shown in the following table 5.1

	TRTS (terahertz)	solar cell	TRMC (microwave)	Hall
	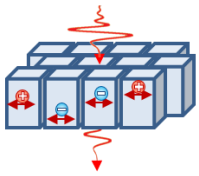	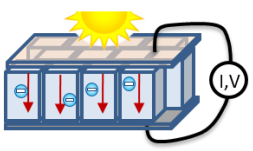	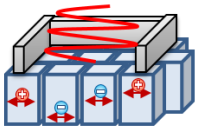	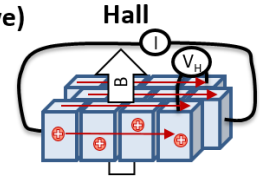
carrier kind	electrons & holes	minority carriers	electrons & holes	majority carriers
transport direction	lateral	vertical	lateral	lateral
requirements	no top contact	contacts	no top contact wave guide	contacts
transport frequency	THz	DC	GHz	DC
transport distance	nm	µm		mm
excitation	pulsed	continuous	pulsed	dark
additional results	localization effective mass scattering time	doping		doping

Table 5.1: Comparison of techniques for measurement of charge carrier mobility in a polycrystalline thin film.

Statements are given for "typical" measurements – no claim of completeness.

The ***kinds of charge carriers*** probed by TRTS are photo-excited electrons and holes. Therefore, the derived mobility is usually the sum of the electron mobility and the hole mobility. TRMC also derives the sum of the electron mobility and of the hole mobility. Hall measurements are preformed usually in the dark and yield the majority charge carrier mobility.

However; in solar cells (and for their V-IQE) the charge transport is limited by the photo-excited minority charge carriers. To overcome these differences to TRTS, the distinction of electron and hole mobility by TRTS will be addressed in this work in Section 6.4. Additionally, Section 7.1 will describe how the pulsed photo-excitation in TRTS can be matched to the continuous excitation in the solar cell.

The ***probed transport direction*** in TRTS and TRMC is given by the polarization of the electric field of the terahertz or microwave radiation. Therefore, the probed transport direction is lateral under the usual vertical incidence of the terahertz pulse or microwave. Hall measurements are usually performed laterally.

In a solar cell (and for their V-IQE) the transport is vertical. However, the charge carrier mobility in a semiconductor usually does depend significantly on the direction.

The ***transport distance*** that is probed by TRTS is usually on the nm-scale, which will be discussed in Section 6.4. Such a distance corresponds in polycrystalline photovoltaic materials usually to intra-grain

transport. Hall measurements are usually probed over distance on the mm-scale and can be limited by inter-grain transport in polycrystalline materials.

In solar cells (and for their V-IQE) the transport distance is given by the thickness of the solar cell which is typical ~1 µm for thin-film solar cells. The TRTS derived transport on the nm-scale will be similar to the transport through the solar cell absorber when no lateral grain boundaries are present between front and back contact.

The ***probed transport frequencies*** for TRTS and TRMC are alternating currents (AC) at terahertz and gigahertz frequencies, respectively. Hall measurements usually apply a direct current (DC).

In solar cells (and their V-IQE measurements) the charge transport is a direct current. Therefore, the AC-mobilities measured by TRTS have to be modeled to derive the DC mobilities. To this end, the mobility models of Section 2.4 can be used. However, such frequency-dependence of the mobility reveals the nature of the transport and properties as localization strength, the transport effective mass and scattering time. Therefore, it can be used to identify the limitations of transport in photovoltaic materials.

Contacts are not required or TRTS. They even oppose the measurement because they are usually opaque for terahertz radiation and at least the front contact should be absent. The detrimental impact of the back contact on TRTS was discussed in Section 5.2. TRMC requires no direct physical contact but a cavity, which guides the microwave to the sample and cannot be probed on a conductive substrate. Hall measurement requires specific electrical contacts and can also not be performed on a thin film that is on a conductive substrate.

Solar cells (and their V-IQE measurements) require front and back contacts. Therefore, TRTS cannot be performed on a finished solar cell. However, this difference also can be a great advantage of TRTS, because the front contact has not to be deposited to studied the mobility in the photovoltaic materials which saves time and allows for high throughput screening of photovoltaic materials.

Regarding all these differences between the measurement techniques, it is not surprising that they yield different mobility values. Figure 5.6 shows the mobilities that were measured by TRTS, Hall and V-IQE in $Cu_2ZnSn(Se,S)_4$ samples with different S/(S+Se) rations, which result in a shift of the bandgap E_G of the material [4].

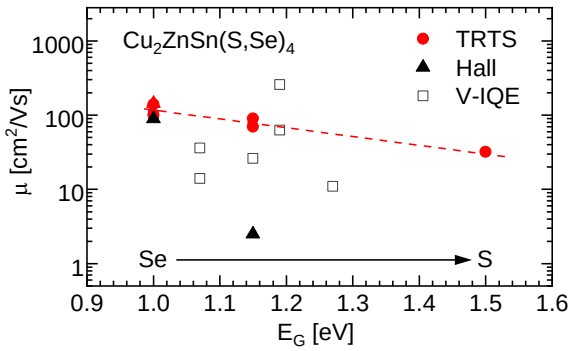

Figure 5.6: Comparison of mobility measurements on $Cu_2ZnSnSe_4$. *Mobilities μ of $Cu_2ZnSn(S,Se)_4$ samples that were derived by time-resolved terahertz spectroscopy (TRTS), a combination of Hall and conductivity measurements (Hall) and voltage-dependent internal quantum efficiency analysis (V-IQE). The V-IQE mobilities are taken from* [41] [64]*. The bandgap E_G of the samples increases with the sulfur content. The observed trend (dotted red line) in the TRTS-derived mobilities is concealed by the large spread of the Hall and V-IQE derived values.*

The TRTS-derived sum mobilities exhibit in Figure 5.6 a clear trend to lower mobilities for the sulfur contacting $Cu_2ZnSn(Se,S)_4$, which we published in [4]. The spread of the TRTS-derived sum mobilities for one composition is relatively low. For a bandgap of 1 eV, four samples from different research groups are shown in Figure 5.6, which will be further discussed in Section 6.4.

The V-IQE derived electron mobilities were taken from the literature [41] [64] and exhibit a large spread, which conceals the dependence on the Se/S ratio. The origin of this spread may be caused by the individual uncertainties of the many supplementary measurements (doping by capacitance-voltage, lifetime by time-resolved photoluminescence (TRPL), absorption and reflection in an Ulbricht's sphere, layer thickness by a profilometer). However, the V-IQE derived mobilities, which were measured on the finished solar cell, agree in average on the TRTS derived mobilities. This agreement shows that TRTS derives the relevant mobility for the photovoltaic application for this particular material. In Section 6.5 an in-depth analysis of TRTS will show that TRTS-derived the sum mobility is indeed governed by the electron mobility that limits the current collection in the V-IQE measurements on the p-type $Cu_2ZnSnSe_4$.

Hall measurements derived hole mobilities of 89 cm^2/Vs and 2.5 cm^2/Vs on the single crystal (E_G = 1 eV) from Delaware [18] and on a polycrystalline thin film (E_G = 1.15 eV) that was produced by a wet-chemical synthesis at IMRA in France [66] [67]. Therefore the Hall mobility is likely limited by the transport across grain boundaries and which also conceals the dependence on the Se/S ratio for polycrystalline samples.

5.3.2 Transient Measurements

Common techniques in the photovoltaic community to probe charge carrier recombination and lifetimes are time-resolved photoluminescence (TRPL), time-resolved microwave conductivity (TRMC) and transient absorption (TA). These techniques are illustrated in Figure 5.7 and will be compared by theory and experimentally in this section. TRTS was already introduced in-depth in Chapter 4.

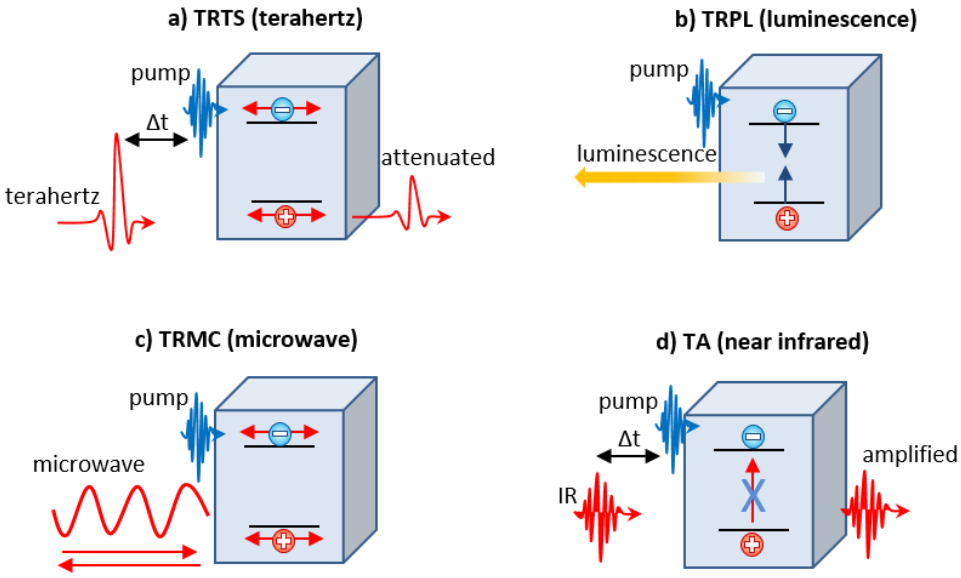

Figure 5.7: Illustration of transient-techniques to derive the charge carrier lifetime. *a) Time-resolved terahertz spectroscopy (TRTS). b) Time-resolved photoluminescence (TRPL). c) Time-resolved microwave conductivity (TRMC). d) Transient absorption (TA)*

Time-resolved photoluminescence (TRPL) is the prevalent transient method in the photovoltaic community and is illustrated in Figure 5.7b. An optical pulse with photon energies larger than the bandgap photo-excites charge carriers. The decay of these excited charge carrier concentration is monitored by the decay of the emitted photoluminescence. This luminescence is recorded by the photomultiplier, which triggers a single-photon counting system. For each pump-pulse, the time between photo-excitation and the first detected luminescence photon is recorded. Over time a histogram of the photon detection times is generated which yields the transients. The measured luminesce is given to the product of electron and hole concentration and their spatial overlap.

Time-resolved microwave conductivity (TRMC) was already introduced in the previous section on the transport properties and is illustrated in Figure 5.7c.

Transient Absorption (TA) is a pump-probe technique that uses optical and near-infrared probe-pulses instead of the terahertz pulses in TRTS. The pump pulse photo-excites the sample and the generated charge carriers occupy states, which are unavailable for further absorption of light as

illustrated in Figure 5.7d. Therefore, the transmission of the probe pulse increases after photo-excitation. A delay between pump-pulse and probe pulse yields the transients.

	TRTS (terahertz)	TRPL (luminescence)	TRMC (microwave)	TA (near infrared)
	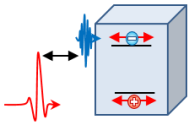	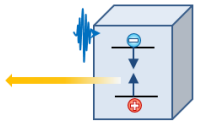	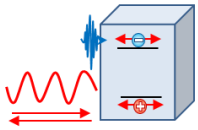	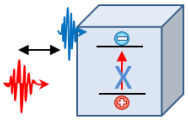
time resolution	~ 100 fs	~ 100 ps	~ 3 ns	~ 100 fs
spatial resolution	~ 1 mm	~ 500 nm	~ 1cm	~ 500 nm
individual dependencies	• trapping • plasmons • phonons • excitons	• electron-hole separation • higher order PL	• trapping • plasmons	• band gap renormalization • carrier cooling • lattice heating

Table 5.2: Comparison of transient-techniques for measurement of charge carrier recombination. *Statements and values are given for "typical" measurements – no claim of completeness.*

The ***time resolution*** of TRTS is given by the temporal width of the optical pump pulse, which is typical ~100 fs. However, for a resolution below ~2 ps, a specific analysis has to be applied that was discussed in Section 4.3.2. TA uses similar pump pulses as TRTS and therefore also has a similar resolution of ~100 fs. The resolution of TRPL is limited by the speed of the electronic readout and is usually ~100 ps. A similar time resolution can be achieved in principle by TRMC. However, in a resonate configuration, the time resolution is typically limited to ~10 ns.

The ***spatial resolution*** of TRTS is limited by the wavelength of terahertz radiation and its diffraction limit to ~300 µm. Such a resolution is, for instance, sufficient for the mapping of combinatorial photovoltaic samples. For the same reason, TRPL and TA have a much higher spatial resolution in the order of ~500 nm. TRMC has a diffraction limit of ~ 1 cm.

The **"individual dependencies"** of the methods are summarized in table 5.2 other dependencies than the direct proportionality to the photo-excited charge carrier concentration. Such dependencies can lead to decays in the measured transients that are not connected to charge carrier recombination. To prevent a misinterpretation as charge carrier recombination a careful assignment of the origin of the measured transient is required. For TRTS a decay of the charge carrier mobility (section 6.2), plasmonic effects or phonons and excitons in the terahertz range can affect the TRTS transient. Additionally, the calibration of the TRTS transients is important, which was shown in Section 4.3.1. TRMC is also sensitive to the decay of the charge carrier mobility and plasmonic localization should be even more pronounced than in TRTS. For TRPL the separation of electrons and holes, as well as the transition from high

injection to low injection, affect the transient behavior [15]. TA is sensitive to the bandgap renormalization, thermalization of charge carriers and lattice heating.

Experimentally, these time-resolved techniques are compared in Figure 5.8a/b. TRTS, TRPL and TA transients were measured on the same $Cu_2ZnSnSe_4$ thin film that was produced in the USA at the national renewable energy lavatory (NREL) in the group of Ingrid Repins [68]. They are shown in Figure 5.8a and are in relatively close agreement with each other. Only, the TA transient deviated slightly at times larger than 1 ns.

Additionally, TRTS, TRPL and TRMC transients were measured on a $Cu_2ZnSnSe_4$ thin film that was produced in France at IMRA [66] [67]. They are shown in Figure 5.8b and again TRTL and TRTS transient are in relatively close agreement to each other. However, the TRMC transient, which was measured by Sönke Müller at the HZB, deviates strongly.

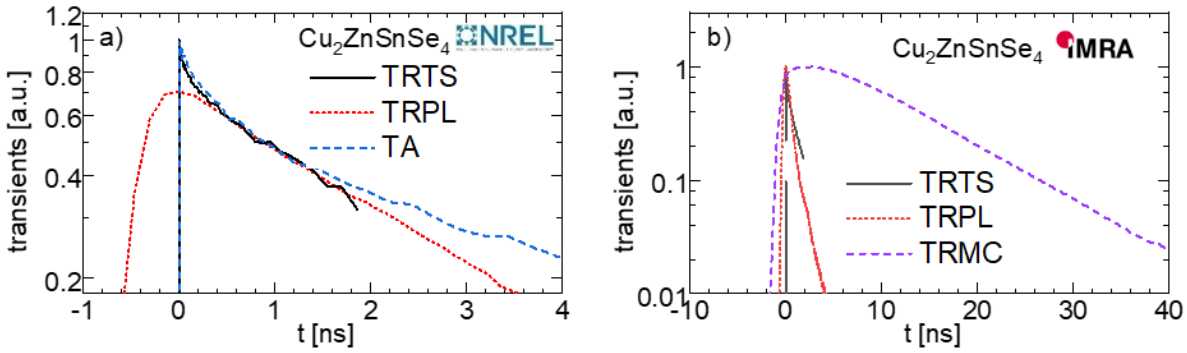

Figure 5.8: Comparison of transient techniques on $Cu_2ZnSnSe_4$. *a) Transients measured by time-resolved terahertz spectroscopy (TRTS), time-resolved photoluminescence (TRPL) and transient absorption (TA) on a $Cu_2ZnSnSe_4$ thin film that was produced at NREL. b) Transients measured by TRTS, TRPL and time-resolved microwave conductivity (TRMC) on a $Cu_2ZnSn(S,Se)_4$ thin film that was produced at IMRA.*

Overall TRTS, TRPL, and TA are in a relatively close agreement with each other. Such an agreement is not self-evident, because the individual techniques are also sensitive to other pump-induced effects than the charge carrier concentration and its recombination. In this case, the agreement of TRPL and TRTS concludes that the TRTS transient is not caused by a decay of the mobility, which would exclusively affect the TRTS transients, and that the TRPL transient is not affected by separation of electron and hole distribution or by higher-order photoluminescence, which would cause a faster TRPL decay. Hence, such a combination of transients can be used to identify the origin of the transient signal, which is in this case indeed the recombination of charge carriers.

The minor deviation of the TA transient in Figure 5.8a may be connected to a contribution from bandgap renormalization or lattice heating, which are not directly proportional to the charge carrier concentration.

The major deviation of the TRMC transient in Figure 5.8b may be connected to the relatively high injection level and photo-induced conductivity. The measured pump-induced change in the microwave power $\Delta P/P$ is only proportional to the photoconductivity in the limit of $\Delta P/P \ll 1$. However, further investigations are required, to definitely attribute the observed deviation.

However, the superior time-resolution of TRTS and TA can be clearly seen in Figure 5.8a. On the other side, our TRTS setup is limited by delay line to 1.8 ns, whereas the TRPL and the TRMC transients could in principle resolve the total timespan between two pump pulses, which are in our case 1 µs and 6.6 µs.

6 In-depth Characterization of Kesterite-type $Cu_2ZnSnSe_4$

The in-depth characterization of a coevaporated $Cu_2ZnSnSe_4$ thin film is the experimental core of this work and resulted in the first author publications [3] [4] [6]. This thin film was produced during my stay in the USA at the National Renewable Energy Laboratory (NREL) in the group of Ingrid Repins, at conditions similar to their record $Cu_2ZnSnSe_4$ solar cells with 9.8 % efficiency. The details of the synthesis on a molybdenum coated glass substrate can be found in [68]. After deposition, the thin film was lifted off the opaque substrate to probe it in transmission by a combination of complementary time-resolved spectroscopy techniques as illustrated in Figure 6.1b.

$Cu_2ZnSnSe_4$ stands exemplary for polycrystalline semiconductors in which band tails affect the optoelectronic properties and possibly limit their commercial applications. This particular kesterite compound was mainly developed as an alternative to the commercially successful $Cu(In_x,Ga_{1-x})Se_2$ solar cells by replacing the rare and expensive In and Ga by abundant Zn and Sn. However, the record efficiency for kesterite-type $Cu_2ZnSn(S,Se)_4$ solar cells, in general, stagnates since 2013 at 12.6 % and stayed far below the record efficiency of 22.9 % for the In and Ga containing counterpart [37] [19].

A major difference between these two materials lies in the absorption and emission tails, which are in general more pronounced for kesterites. Therefore, the inferior efficiencies of kesterite solar cells are often attributed to band tails, although the evidence for such connection is limited [69] [70] [71] [72] [73] [74]. Therefore, a major question of this work is: How much do band tails contribute to the losses in current and voltage of kesterite solar cells compared to their Shockley-Queisser limit [34], which is illustrated in Figure 6.1a. To answer this question the impact of tail states on charge carrier dynamics is probed in this chapter in-depth, which will be used in the next chapter to estimate the limits and loss in $Cu_2ZnSnSe_4$.

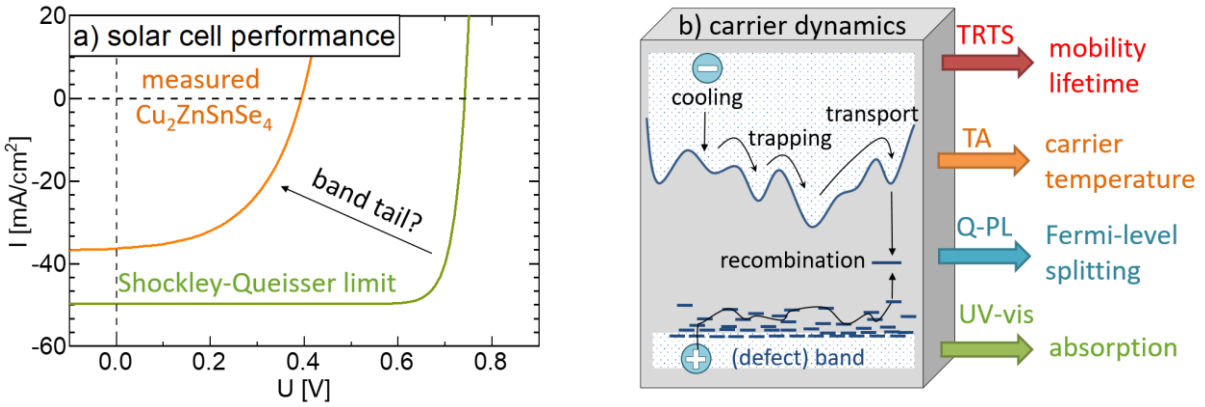

Figure 6.1: The impact of band tails. *a) The current-voltage curve of the finished kesterite solar cells is far below the Shockley-Queisser limit which may be caused by band tails. b) The combination of quantitative photoluminescence (Q-PL), time-resolved terahertz spectroscopy (TRTS) and transient absorption (TA) reveal the full dynamics of photo-excited charge carriers including thermalization, trapping, transport, and recombination. Thus, clarifying the losses in Fermi level splitting, mobility and lifetime.*

However, it remains unclear, whether these tail states are strictly speaking a tail of microscopically localized states due to short-range disorder [75] [76] [77] or whether they are of different nature like defects [78] [79], defect bands [80] [81], classical macroscopic band edge fluctuations [82] [83] [84] or a superposition of them. The common ground for these pictures is a broad distribution of localized states relatively close to the effective band edges which causes the observed absorption and emission tails. Hence, this inclusive definition of band tails will be used here.

The reports on the impact of band tails on charge carrier dynamics in kesterite are rather diverse. Tail states can explain the observed trapping [85] [15], the dispersive and relatively low charge carrier mobility [4] [80], the charge carrier localization [4], the voltage-dependent recombination in kesterite solar cells [86] and their reduced quasi-Fermi level splitting in the radiative limit [35]. However, these individual studies do not assemble into a consistent picture as they use different band tail models and were performed on different samples.

Here, we study the full charge carrier dynamics on the same $Cu_2ZnSnSe_4$ sample to develop a comprehensive model of charge carrier cooling, trapping, transport, and recombination. Thus, the optoelectronic properties and their limitations by band tails are revealed. These properties allow us to predict the performance of kesterite solar cells and to assign the losses to specific origins.

The theoretical background of this chapter was introduced in Chapter 2.

6.1 Absorption Tails

The absorption coefficient *α(E)* of the $Cu_2ZnSnSe_4$ thin film exhibits in Figure 6.2 a significant absorption below the theoretical bandgap of 1 eV [78], which implies the presence of band tails. The shown absorption coefficient was derived by Charles Hages from the analysis of the voltage-dependent internal quantum efficiency, which is detailed in [41]. It was also confirmed by transmission and reflection measurement in an Ulbricht sphere.

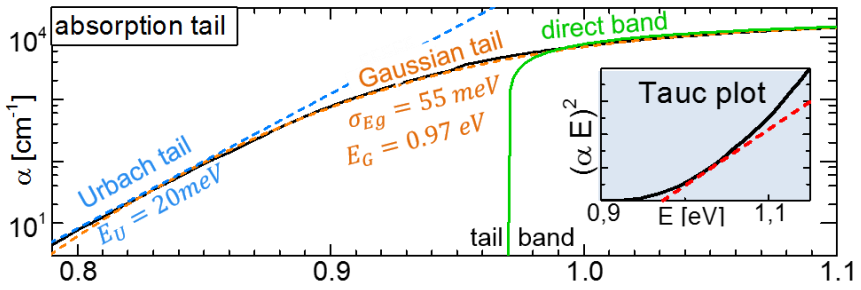

Figure 6.2: Absorption tails. *Absorption coefficient α of $Cu_2ZnSnSe_4$ derived from the quantum efficiency of the finished solar cell. It is modeled by the absorption of a direct semiconductor which is folded with a Gaussian distribution of band gaps. The energy tail is modeled by an Urbach tail. Inset: Tauc-plot of the absorption does not exhibit the usual linear region.*

Usually, the absorption of a direct semiconductor is described by $\alpha = A(E-E_G)^{0.5}/E$. However, the determination of the bandgap energy by the Tauc-method of plotting $(aE)^2$ vs. E (inset of figure 2a) was not possible as no linear region was found [87]. Therefore, the absorption does not follow the usual dependency for a direct bandgap semiconductor. Such behavior was previously discussed for kesterite semiconductors in [88]. It can be explained by disorder, which is known for smearing out the band edges, shifting the bands into the bandgap and localizing the band states close to the band edges [77].

The absorption coefficient in figure 6.2 can be modeled by a Gaussian distribution of direct band gaps in Equation (6.1) [69] with a mean band gap E_G of 0.97 eV and a standard deviation σ_{Eg} of 55 meV.

$$\alpha = \int_0^\infty \frac{1}{\sqrt{2\pi}\sigma_{Eg}} exp\left(-\frac{1}{2}\left[\frac{E_G^* - E_G}{\sigma_{Eg}}\right]^2\right) A\frac{\sqrt{E-E_G^*}}{E}\theta(E-E_G^*)\,dE_G^* \qquad (6.1)$$

This distribution of band gaps likely corresponds to macroscopic potential fluctuations, which are usually assumed to be Gaussian due to their random statistical nature. If these fluctuations are macroscopic, the density of states and the absorption are a classical convolution of the unperturbed quantity and the Gaussian distribution in Equation (6.1).

In contrast, exponential tails can be explained by microscopic potential fluctuations. Microscopic potentials on the atomic level lead to quantum confinement and a Gaussian potential distribution can result in exponential Urbach tails [76]. Such an exponential absorption tail $\alpha \sim exp(-E/E_U)$ [89] is observed in Figure 6.2 for photon energies below 0.85 eV and is modeled with an Urbach energy E_U of 20 meV similar to the values reported in [73]. This Urbach energy is smaller than k_BT and small compared to typical values of semiconductors with strong band tails such as amorphous silicon with ~50 meV [23].

However, in general, such observed absorption tails do not unambiguously quantify the tails in the density of states. The absorption is a convolution of the densities of the conduction and valence band states as well as of a possibly energy-dependent matrix element. Therefore, an absorption tail does not reveal if the conduction band or the valence band or both bands have a tail in the density of states.

6.2 Ultrafast Charge Carrier Dynamics

After the absorption of light, the life of a photo-excited charge carrier starts. In this section, its ultrafast dynamics are probed by the complementary combination of ultrafast time-resolved techniques.

The cooling in the band states and the trapping into the tail states will be probed by transient absorption. Simultaneously, the localization of charge carriers is monitored by time-resolved terahertz spectroscopy (TRTS), which additionally distinguishes these processes from charge carrier recombination. Further, the transition from bipolar to ambipolar transport is derived from terahertz emission spectroscopy.

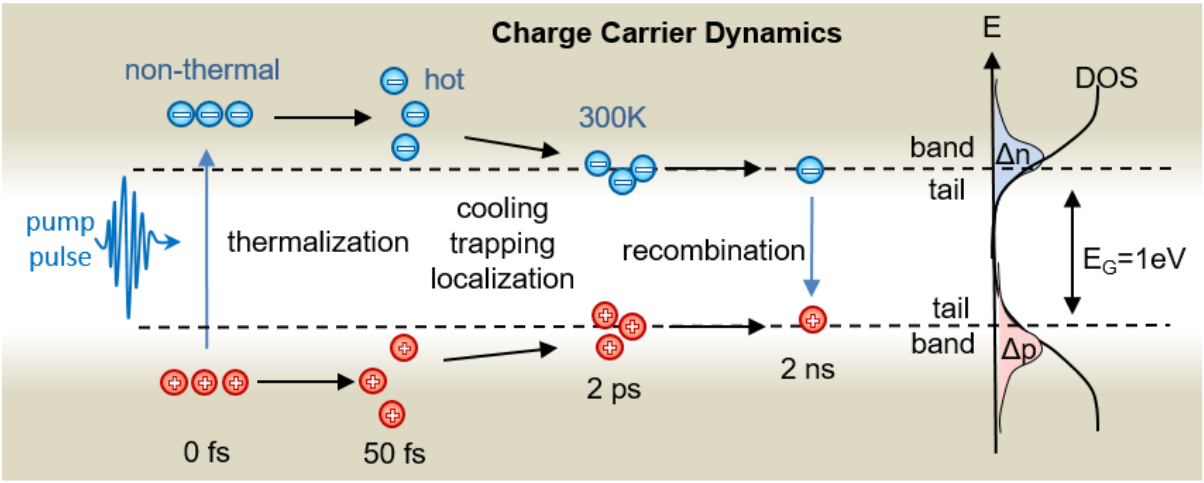

Figure 6.3: Overview of charge carrier dynamics probe in this section. *Initially, charge carriers are excited into the density of states (DOS) with a non-thermal distribution of electrons Δn(E) and holes Δp(E). Afterward, this distribution thermalizes in the bands and forms a hot Fermi-Dirac distribution. Then, it cools to lattice temperature and carriers also trap into tail states and localize there. Finally, the charge carriers recombine.*

Charge Carrier Thermalization in the Band States

Directly after photo-excitation with a ~100 fs laser pulse, the charge carriers are in a non-thermal distribution, which is illustrated in Figure 6.3. Afterward, the charge carriers scatter and exchange energy. Within the effective scattering time τ_{sc} of 50 fs in $Cu_2ZnSnSe_4$, which will be obtained later in this section, the charge carriers thermalize and form a hot Fermi-Dirac distribution, which is described by equations (2.1-3). Initial carrier temperature of this distribution $T_C = E_{ex}/3k_B$ is ca. 3000 K due to the excess energy $E_{ex} = E_{Ph}-E_G$ of the pump photons with an energy E_{Ph} of 1.78 eV.

Charge Carrier Cooling in the Band States

The cooling of the charge carriers to lattice temperature can be monitored by transient absorption (TA), which was briefly introduced in Section 5.3.2 and is illustrated in Figure 6.4a. It measures the photo-induced absorbance $\Delta A(E_{Ph},t)$ spectra as a function of the photon energy E_{Ph} of the probe-pulse and of the delay t between pump-pulse and probe-pulse. The measurements were performed by me during my stay in the group of Matt Beard at NREL in the USA.

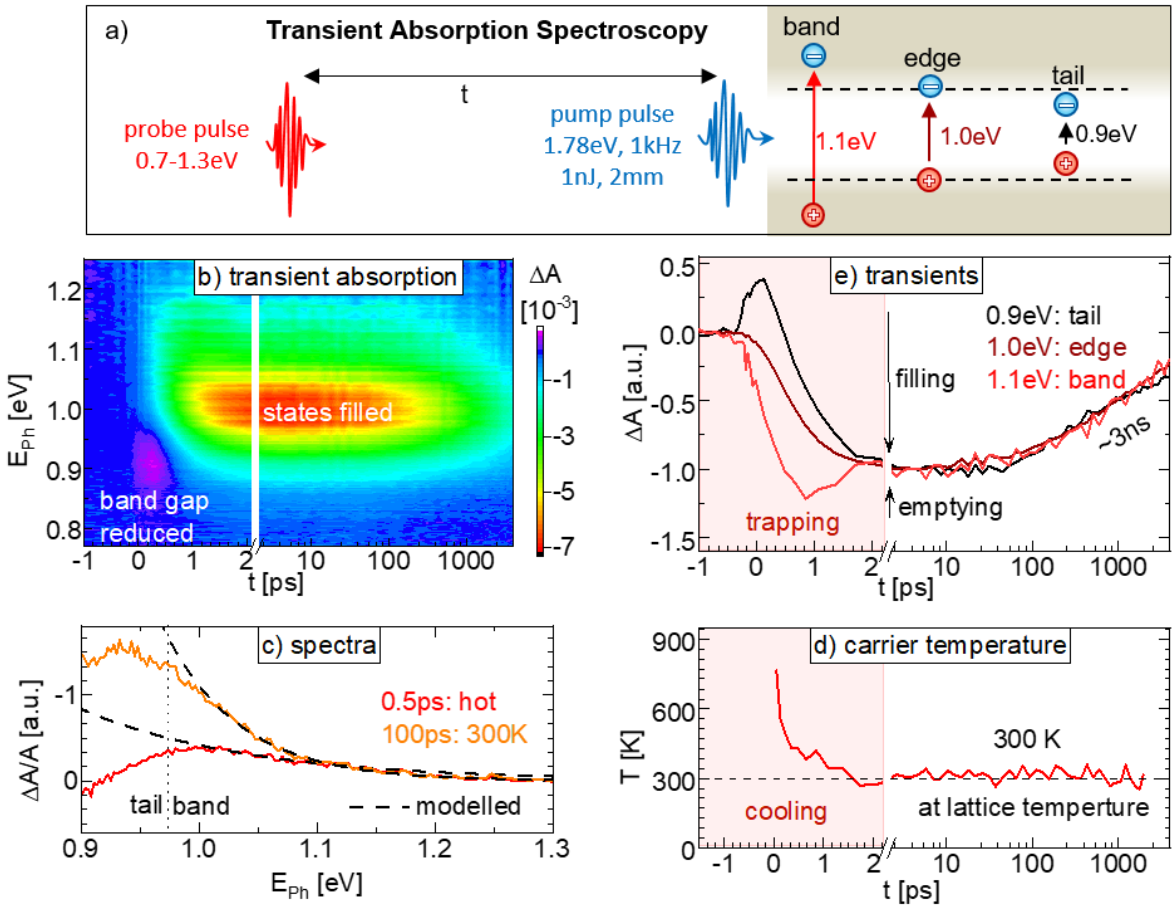

Figure 6.4: Charge carrier cooling and trapping probed by transient absorption (TA). *a) Principle of transient absorption. b) Measured photo-induced absorbance $\Delta A(E_{Ph},t)$ for probe photon energy E_{Ph} and pump-probe delays t. c) Photo-induced absorbance spectra $\Delta A(E_{Ph})$ at 0.5 ps and 100 ps after photo-excitation are modeled by state-filling with a charge carrier temperature T_C. d) Kinetics in T_C derived from modeling of all spectra, which*

are shown in a). e) Transients of the photo-induced absorbance ΔA at three different photon energies which are dominated by band, band edge and tail transients, respectively.

The transient absorption spectra of $Cu_2ZnSnSe_4$ that are shown in Figure 6.4b are similar to what has been reported for crystalline semiconductors as GaAs or MAPbI3 [90]. They were measured under pulsed excitation with a wavelength of 700 nm, a repletion rate of 1 kHz, a pulse energy of 1 nJ and an estimated pump spot FWHM of ~ 2 mm. It exhibits in Figure 6.4b an increased absorbance $\Delta A(E_{Ph},t)$ due to bandgap shrinkage for the first picosecond and for photon energies E_{Ph} below the bandgap energy of ~ 1 eV [91] [90]; and a decreased absorbance due to states filing for higher energies or longer times [90]. In contrast, strongly band-tailed amorphous semiconductors such as a-Si or a-Ge exclusively exhibit an increased intra-band or intra-tail absorption [92] [93].

The change in the band absorbance due to filling of the band states can be modeled by $\Delta A/A \sim exp(-E_{Ph}/ak_BT_C)$ [90], where T_C is the charge carrier temperature and the constant a is determined by the effective masses of the conduction and the valence band. Such modeling is shown in Figure 6.4c for the photo-induced absorbance spectra $\Delta A(E_{Ph})$ recorded 0.5 ps and 100 ps after the photo-excitation of the sample. Assuming that the final carrier temperature equals the lattice temperature of 300 K, the decay of the carrier temperature T_C is derived, which is shown in Figure 6.4d.

In Figure 6.4d the thermalization of photo-excited charge carriers in band states could be resolved from ~ 700 K to room temperature, which takes place within ~2 ps. Such thermalization times are typical for direct semiconductors (0.1-4 ps for GaAs [94] [95] [96]) and are in contrast to long-time thermalization via multiple trapping observed in a-Si or a-Ge [97]. Slower thermalization kinetics of up to ~100 ps were observed at the higher injection levels by transient reflection in single crystals of the related material Cu_2SnZnS_4 [85] and may indicate a hot-phonon bottle-neck at high injection levels [90] [98].

Charge Carrier Trapping into Tail States

Transients of the photo-induced absorbance at three different photon energies E_{Ph} are shown in Figure 6.4e. These three phonon energies E_{Ph} correspond to transitions between band states (E_{Ph} = 1.1 eV), band-edge states (E_{Ph} = 1.0 eV) or tail states (E_{Ph} = 0.9 eV), which is illustrated in Figure 6.4a. After the instantaneous bandgap shrinkage, the photo-induced absorbance ΔA at all three photon energies becomes negative due to the filling of the involved states by the photo-excited charge carriers. Therefore, the kinetics in the photoinduced absorption $\Delta A(t)$ are dominated by the filling and emptying of these states.

The decrease in the photo-induced absorption of all three transitions can be attributed to state filling due to the thermalization of carriers from energetically higher states. The band absorbance at 1.1 eV

increases in Figure 6.4e again after 0.7 ps, which corresponds to the emptying of the band states as the carriers thermalize further into the energetically lower band edge and tail states.

The occupation of edge and tail states increases throughout the initial 2 ps and stays approximately constant for the next tens of picoseconds. Such behavior reveals that band edge and band tail states are only filled and not emptied within that time. In particular, no emptying of the band edge states involved in the 1.0 eV transition by the capture into tail states is observed. Additionally, no significant emptying of the states by recombination seems to have taken place within the initial tens of picoseconds.

In conclusion, the measured kinetics show that photo-excited charge carriers simultaneously thermalize in the band, edge and tails states within the first 2 ps, which implies that no relaxation barrier exists between band and tail states as may be expected for a defect band well separated from the band states.

Charge Carrier Localization

The kinetics of the transport properties of the photo-excited charge carriers can be measured by time-resolved terahertz spectroscopy (TRTS) on the same time scale at which their cooling and trapping were measured by near-infrared transient absorption. TRTS was described extensively in Chapter 4 and derives the photoconductivity $\Delta\sigma(f,t)$ at terahertz frequencies f and as a function of the delay time t between the optical pump-pulse and the terahertz probe-pulse, which is illustrated in Figure 6.5a and shown for the $Cu_2ZnSnSe_4$ thin film in Figure 6.5b.

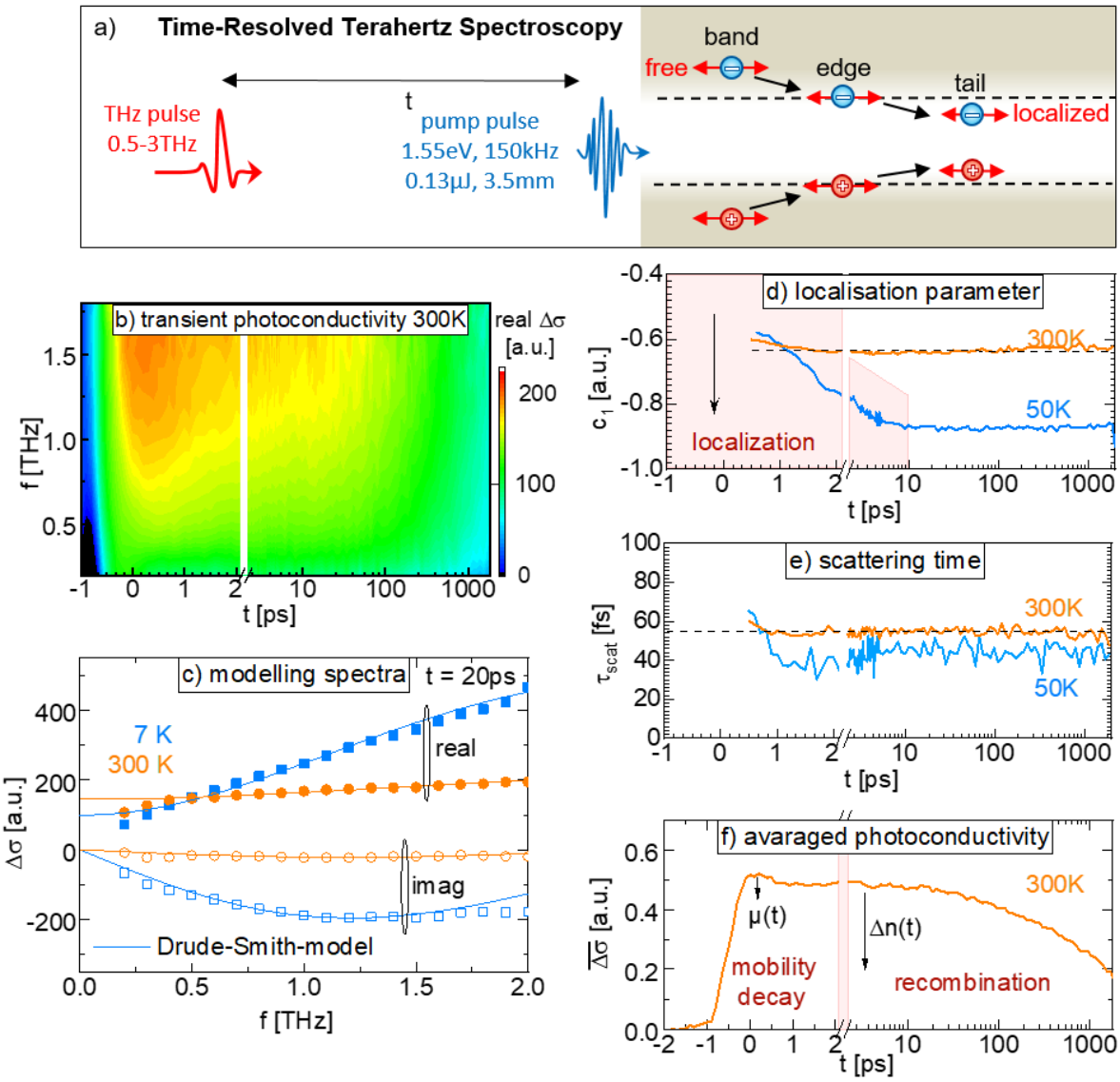

Figure 6.5: Charge carrier localization and recombination probed by TRTS. *a) Principle of TRST which probes the transport of the photo-excited charge carriers. b-c) Measured photoconductivity as a function of time t and frequency f. Modeled by Drude-Smith model. d) Localization parameter c1 of the Drude Smith model is a measure of charge carrier localization e) Scattering time of the Drude-Smith model. f) Charge carrier concentration derived for Drude-Smith fit.*

The conductivity spectra $\Delta\sigma(f)$ at the individual delay times are shown exemplarily in Figure 6.5c at 20 ps after photo-excitation for two different sample temperatures of 300 K and 50 K. They exhibit an increasing real part of the mobility for increasing terahertz frequencies *f,* which is a fingerprint of charge carrier localization. Such frequency-dependence can be modeled in Equation (6.2) phenomenological by the Drude-Smith model [31], which was introduced in Section 2.2.5 and will be analyzed in more detail in the next section. Here, the discussion will be limited to the kinetics in the modeled parameters, which are the localization parameter c_1 and the effective scattering time τ_{scat} and the pre-factor, which is constituted of the photo-excited charge carrier concentration Δn, the elementary charge e and the effective transport mass m_{eff}.

$$\sigma_{DS} = \frac{e^2 \Delta n}{m_{eff}} \frac{\tau_{scat}}{1 - i\omega\tau_{scat}} \left(1 + \frac{c_1}{1 - i\omega\tau_{scat}}\right) \quad (6.2)$$

The Drude-Smith modeling of the individual photo-conductivity spectra for the series of delay times yields the kinetics in the localization parameter and in the scattering time, which are shown in Figure 6.5d/e.

The localization parameter c_1 generally spans from 0 for free transport to -1 for completely localized charge carriers. For the $Cu_2ZnSnSe_4$ thin film, a pronounced localization parameter c_1 below -0.5 is observed in Figure 6.5d already for very short delay times. At such delay times, carriers are still hot and in high energetic band states, which was determined by transient absorption in Figure 6.3d/e.

Looking more closely at Figure 6.5d, a slight change in the localization parameter c_1 is observed within the first 2 ps. This initial ultra-fast localization of carriers matches the thermalization and tail capture times observed in the previous section by transient absorption at 300 K. Therefore, the localization of photo-excited carrier and their loss in mobility can be attributed directly to their thermalization and capture into the tail states, which is illustrated in Figure 5d.

More pronounced localization kinetics with a transition of the localization parameter c_1 from -0.55 to -0.9 is observed in Figure 6.5d for lower sample temperatures of 50 K. Then, charge carriers freeze into the deeper and more localized tail states. There, they lack the thermal energy to be activated back into energetically higher transport states. The localization of charge carriers into deeper tail states continues until all deeper tail states are filled, which is reached for the relatively high induced surface carrier concentration of ca. 2×10^{17} cm^{-3} after 10 ps.

Also, the scattering time exhibits an initial decrease in Figure 6.5e. This behavior may be interpreted as an increasing scatting of the charge carriers when they trap into the tail states.

Despite these insights, one should bear in mind that they are deduced from the Drude-Smith model which is phenomenological and neglects several important aspects. The rigorous modeling of the transport properties during charge carrier cooling and trapping should include an energy-dependent scattering time, which is usually given in band states by Fröhlich optical phonon scattering [24] [24] [20]. Additionally, the charge carrier mobility should be derived from the Boltzmann transport equation, which regards the full band dispersion. Such a dispersion is not described by the effective mass for higher energies [24] [20]. However, the combination of such a model with localized tail states is rather challenging and is beyond the scope of this work. Additionally, a double Fourier analysis of the TRTS data according to [56] should be performed to validate the results at the very initial delay times.

The distinction of Mobility Decay and Recombination

The decay of this photoconductivity $\Delta\sigma(f,t) = e\Delta n(t)\mu(t,f)$ can in principle be caused by a decay of the charge carrier concentration $\Delta n(t)$ or by a decay of the mobility $\mu(t,f)$. However, the frequency-dependence of the photoconductivity originates exclusively from the mobility and therefore distinguishes a decay of the mobility from a decay of the charge carrier concentration. The frequency-dependence in the Drude-Smith model is described by a scattering time τ_{scat} and by a localization parameter c_1. At 300 K, both stay approximately constant after the initial 2 ps and the decay of the photoconductivity can be assigned to the decay of the charge carrier concentration, which is shown in Figure 6.5f.

Such behavior is in line with the observation of a constant charge carrier temperature in Figure 6.4d and with the simultaneous decay of the transient absorption for band, band-edge and tail transitions in Figure 6.4e for times later than 2 ps after charge carrier excitation. It shows that tail states and band states are in a common quasi-equilibrium and that no further relaxation of carriers into deeper tail states occurs. Therefore, at room temperature, we can exclude multiple trapping into deeper tail states in $Cu_2ZnSnSe_4$ which is usually observed for strongly band-tailed semiconductors as a-Si [97]. Instead, the decay of the induced absorption and of the photoconductivity can be assigned to charge carrier recombination.

The transition from the Bipolar to the Ambipolar Transport

Another process that takes place at the first picoseconds after pulsed charge carrier excitation is the transition from bipolar to ambipolar transport.

In general, photo-excited electrons and holes diffuse at their individual speed and have different charge carrier diffusion coefficients and mobilities, which was discussed in the theory section 2.2. However, the individual diffusion is often a self-limiting process because the separation of the distributions of electrons and holes leads to the build-up of a dipole. This dipole between the electron cloud and the hole cloud forces both back together. Then they diffuse together with a common ambipolar diffusion coefficient, which is illustrated in Figure 6.6.

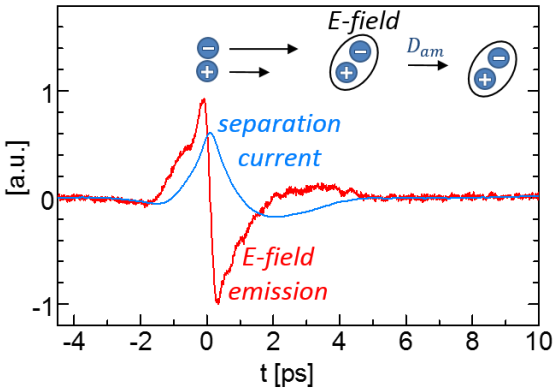

Figure 6.6: Transition of bipolar to ambipolar diffusion derived from terahertz emission. *Photo-excited electrons and holes diffuse apart which emits the measured E-field. The deduced separation current of electrons and holes vanishes after ca. 5 ps indicating common ambipolar diffusion D_{am} of electron and holes for later times. Reproduced from* [5].

$$E_{THz} \propto \frac{d}{dt} I = \frac{d^2}{dt^2} e(n-p) \tag{6.3}$$

The process of the initial individual diffusion, the build-up of the dipole and the following ambipolar diffusion can be monitored by terahertz emission spectroscopy. The build-up of a dipole emits electromagnetic radiation, which is detected by our TRTS setup and shown in Figure 6.6. The amplitude of the emitted electric field is proportional to the derivative of the separation current *I* between the electron and hole distribution. Hence, the integral of the detected terahertz field is proportional to the separation current *I*. Figure 6.6 shows that this separation current vanishes for the $Cu_2ZnSnSe_4$ thin film after ca. 5 ps. Form this explanation follows that electrons and holes diffuse directly after pulsed excitation with their individual mobilities and changes within the ~5 ps to a common ambipolar mobility.

6.3 Recombination Channels

The recombination of charge carriers can be monitored by various time-resolved techniques. For the $Cu_2ZnSnSe_4$ thin-film TRTS, TRPL and TA transients were briefly compared in Section 5.3.2 and it was shown in the previous section that the decay of the TRTS transient is indeed caused by a decay in the charge carrier concentration and recombination after the initial 2 ps. The initial decay was attributed to a decay in the charge carrier mobility which corresponds to trapping.

Here, the dominant recombination channels, which were introduced in Section 2.3, will be identified by wavelength-dependent and intensity-dependent TRTS transients. Such an in-depth analysis of the charge carrier transients may guide further attempts to reduce the recombination in a solar cell absorber. The corresponding publication [5] is attached at the end of this work.

The most common recombination processes in a semiconductor thin film are surface recombination and bulk recombination of first, second and third-order in the excited charge carrier concentration *Δn* as illustrated in Figure 6.7a. Surface recombination depends on the diffusion coefficient *D* and on the surface recombination velocity *S*. The bulk recombination of first-order is characterized by the effective bulk lifetime τ_B. In the following, the presence of surface recombination will be deduced and higher-order recombination process will be ruled out.

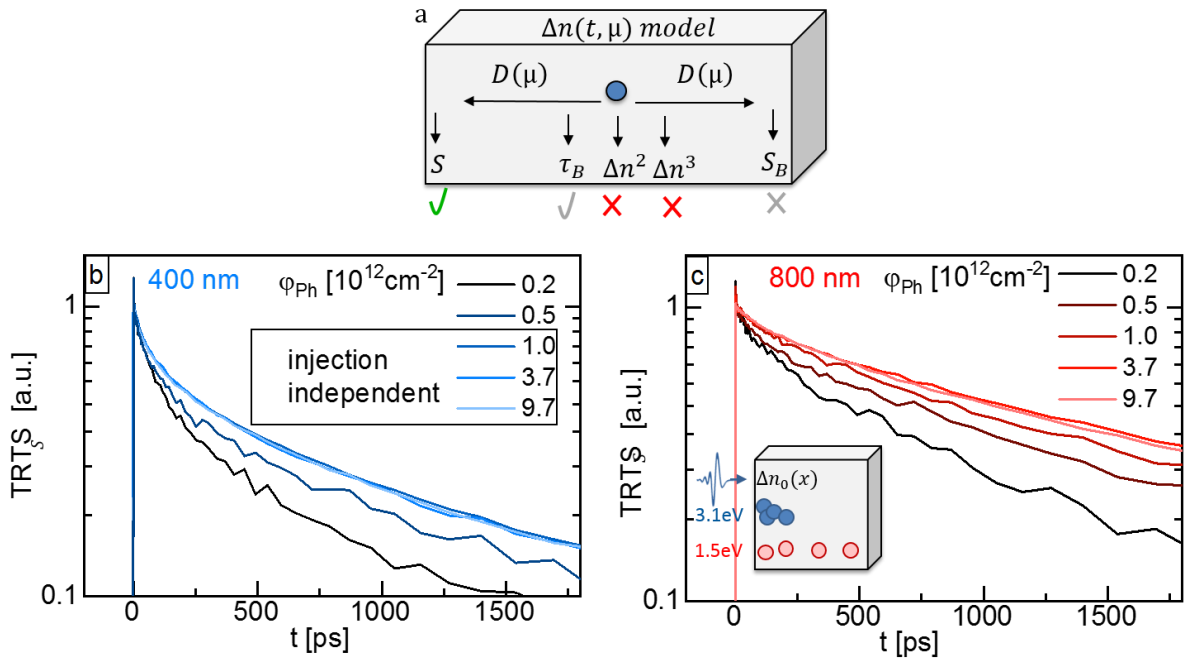

Figure 6.7: Identifying the main recombination processes. *a) Illustration of surface recombination (S), bulk recombination (τ_B), diffusion D and higher-order recombination (Δn^2, Δn^3). b) TRTS transients excited with 400 nm pump light and c) with 800 nm pump light have different penetration depths and reveal surface recombination. Slower TRTS transients with increasing excitation intensity rules out higher-order recombination for the probed $Cu_2ZnSnSe_4$ thin film. c) Reproduced from* [5].

Identifying the Recombination Channels

Figure 6.7b/c shows that the photo-excitation of the $Cu_2ZnSnSe_4$ thin film by pump pulses with a wavelength of 400 nm leads to a faster decay than the excitation by pump pulses with a wavelength of 800 nm. The difference between the 400 nm and the 800 nm excitation is their penetration depths, which are 50 nm and 230 nm, respectively [99]. Therefore, the 400 nm pump light photo-excites the charge carriers closer to the surface and the faster decay indicates a strong contribution from surface recombination [100] [101].

However, also the maximum charge carrier concentration at the surface of the sample is higher for the 400 nm than for the 800nm excitation although the sheet carrier concentration is similar in both cases. Therefore, higher-order recombination, which leads to faster decays at higher injection levels, could

also explain the observed wavelength dependency. Such higher-order recombination is often associated with radiative recombination or Auger recombination.

To examine the influence of higher-order recombination the injection-dependence of the transients is probed in Figure 6.7b/c. They exhibit slower decays for high injection levels, which excludes higher-order recombination.

Instead, the observed behavior is in line with Shockley-Read Hall recombination. At the injection levels with peak charge carrier concentration of between 10^{17} and 10^{18} cm^{-3}, the transients become injection-independent. These injection-independent transients will be modeled in the following by injection-independent bulk recombination and by injection-independent surface recombination.

Modeling the TRTS-Transients

The modeling of the measured transients should include the generation of the charge carriers, their diffusion in the sample and their recombination in the bulk and at the surface of the sample. The theory of such a description was introduced in Section 2.2.

In general, electrons and holes diffuse at their individual speed and have different charge carrier diffusion coefficients and mobilities. However, it was shown in the previous section that they diffuse together with a common ambipolar diffusion coefficient for times later than 5 ps after photo-excitation. Therefore, a common continuity equation (2.14) can be used to describe the transport and recombination of photo-excited electrons and holes for delay times larger than 5 ps. The recombination rate $r = 1/\tau_B$ will be described in the bulk by charge carrier lifetime τ_B. The surface recombination velocity S defines in Equation (2.16) the boundary condition for the charge current in Equation (2.10) [102]. The charge carrier generation g is given in Equation (2.9) by an initial excitation with a pump pulse of characteristic absorption depths ($1/\alpha$) of 230 nm and 50 nm for the 800 nm and 400 nm pump light, respectively [99].

These equations (2.10) (2.13) and (2.16) allow modeling the spatial distribution of the charge carrier concentration $\Delta p(x)$, which is shown in Figure 6.8a.

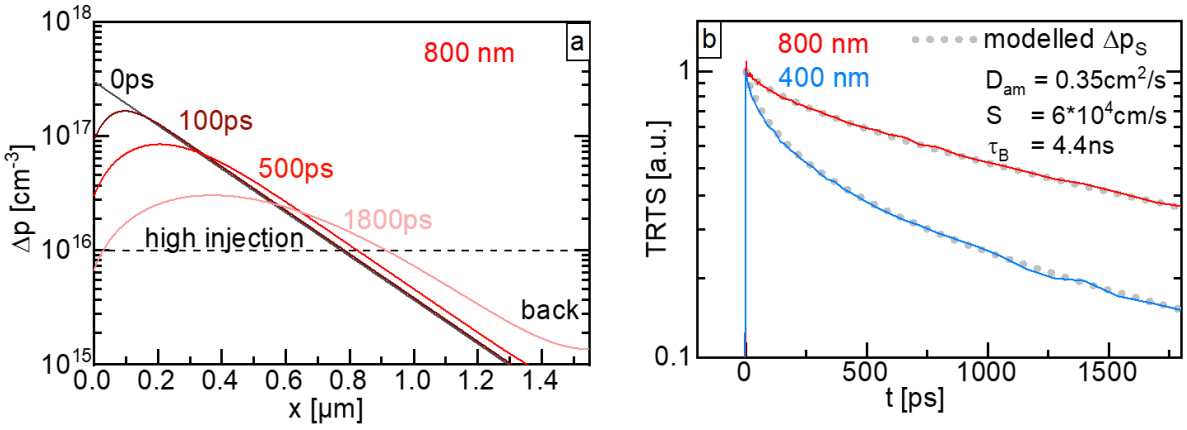

***Figure 6.8: Modeling injection-independent TRTS-transients**. a) Photo-excited charge carrier distribution Δp(x,t) is modeled by the continuity equations, Fick's law and surface recombination with a surface recombination velocity S, an ambipolar diffusion coefficient D_{am}, and an effective bulk lifetime τ_B. It stays in high injection and does not interact with the back surface within the timespan of the TRTS transients. b) The corresponding transient of the sheet carrier concentration Δp_S and the measured TRTS transients. Reproduced from* [5].

Initially, the charge carrier distribution follows the excitation profile. Over time the charge carriers diffuse into the bulk and towards the back surface. Simultaneously they recombine at the front surface and throughout the bulk.

The measured TRTS signal is proportional to the photo-excited sheet carrier concentration $\Delta p_S(t)$. Therefore, the modeled charge carrier concentration $\Delta p(x,t)$ is integrated over the depth of the sample. Numerical minimization of the deviation between measured TRTS transients and modeled decay of the sheet carrier concentration $\Delta p_S(t)$ yields a surface recombination velocity of $6*10^4$cm/s, a bulk lifetime of 4.4 ns and an ambipolar diffusion coefficient 0.35 cm^2/s. This model fits the measured transients in Figure 6.8b very well. Especially, if it is regarded that only three parameters were needed to model two different multi-exponential transients at the same time.

Interestingly, the recombination could be modeled by SRH recombination, which was derived from a discreet trap level within the bandgap. No band tails with a broad distribution of states had to be introduced in the recombination model. Therefore, no clear evidence is found for the impact of the band tails on the charge carrier recombination.

6.4 The Charge Carrier Mobility

The Sum Mobility of Electrons and Holes

The mobility of these charge carriers can be derived from the photoconductivity spectrum, which was shown in Figure 6.5c and was probed 20 ps after photo-excitation. It was shown in Section 6.2 that at

such times, the charge carriers have cooled to lattice temperature and their energetic distribution can be assumed to correspond to the situation in a solar cell. Additionally, it was shown, that at 20 ps no significant fraction of charge carriers has recombined. Therefore, the sum mobility $\mu_\Sigma = \Delta\sigma_S/\Delta n_S/e$ can be derived by dividing the sheet photoconductivity $\Delta\sigma_S$ that was measured by TRTS by the photo-excited sheet charge carrier concentration Δn_S that is calculated from the excitation conditions.

The derived complex-valued mobility μ_Σ of photo-excited charge carrier at terahertz frequencies is shown in Figure 6.9a. It is the sum of electron mobility and the hole mobility and has the same frequency-dependence as the photo-conductivity. Therefore it is also analogously modeled by the Drude-Smith model for localized transport [31], which yields an effective scattering time τ_{sc} of 50 fs, an effective transport mass m_{eff} of 0.215 and the localization parameter c_1 of -0.64. Additionally, a DC-value of 140 cm^2/Vs is retrieved by the Drude-Smith model for the sum of electron mobility and hole mobility. A similar TRTS-derived sum mobility of 70 cm^2/Vs was reported in [103] for a sulfur-containing $Cu_2ZnSn(Se,S)_4$.

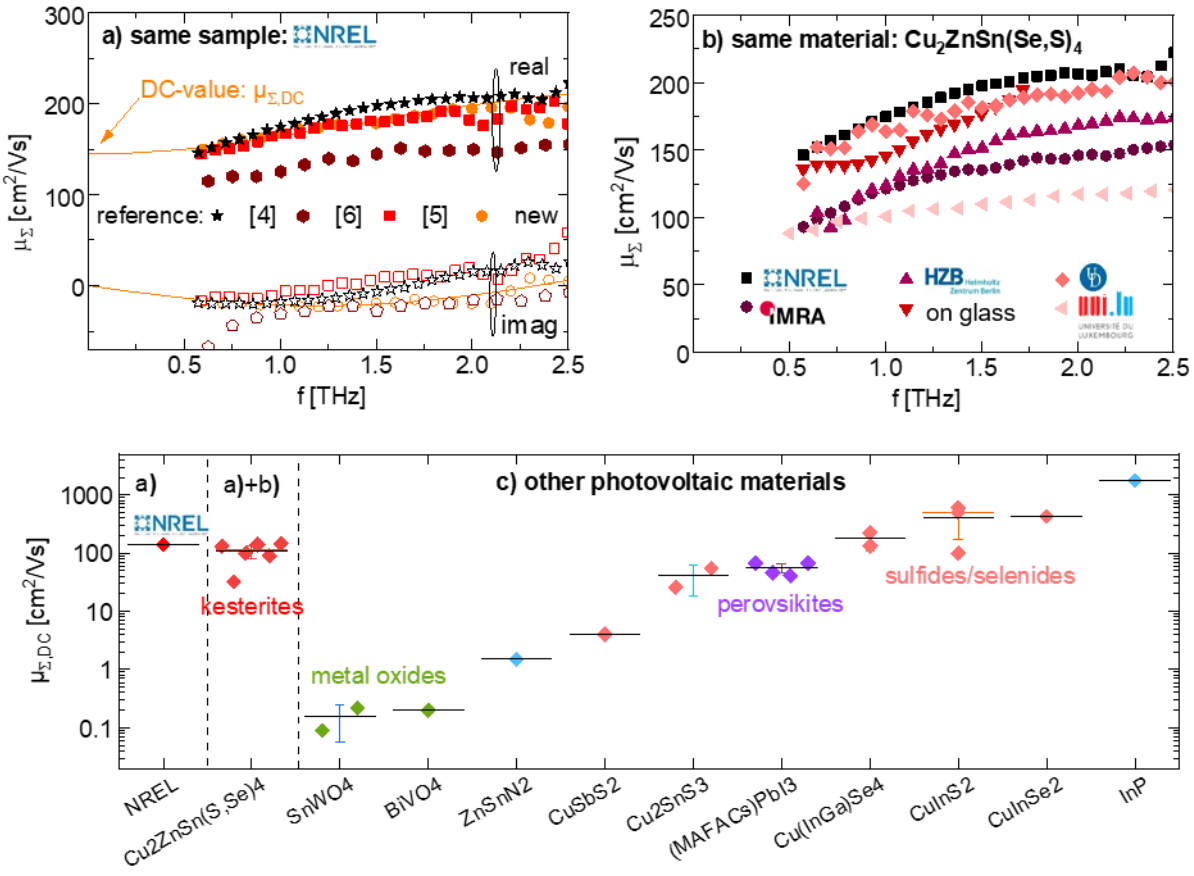

Figure 6.9: DC-value of the sum mobility. *a) Modeling of the sum mobility at terahertz frequencies by the Drude-Smith model to derive a DC-value. b) DC-value of TRTS-derived sum mobilities for different classes of photovoltaic materials.*

To estimate the uncertainty and the reproducibility if the derived mobility, the $Cu_2ZnSnSe_4$ thin film was measured several times in the same TRTS setup. The derived mobilities were published in [4] [5] [6] and are also shown in Figure 6.9a. The reproducibility is relatively good. Only the measurement in my publication [6] deviates stronger by ca. -30 % from the other measurements. However, this measurement was performed in reflection mode on the front side of the $Cu_2ZnSnSe_4$ thin film that was still on the molybdenum coated substrate. The other measurements were performed by transmission mode TRTS on the backside of the $Cu_2ZnSnSe_4$ thin-film after it was lifted off the substrate.

Additionally, $Cu_2ZnSn(Se,Se)_4$ samples that were produced by partners at several research groups were compared to investigate if the charge carrier mobility is specific for $Cu_2ZnSn(Se,S)_4$ or varies from sample to sample. These samples include:

A) The $Cu_2ZnSnSe_4$ thin film that was coevaporated on a molybdenum coated glass substrate at the national renewable energy laboratory (NREL) [68];

B) A $Cu_2ZnSnSe_4$ thin film that was coevaporated on an Al_2O_3 substrate at the University of Luxembourg (uni.lu) [104].

C) A $Cu_2ZnSn(Se,S)_4$ thin film that was produced by the selenization of a metal-salt precursor on a molybdenum coated glass substrate at IMRA [66];

D) A $Cu_2ZnSnSe_4$ thin film that was produced by the selenization of a sputtered metal precursor on a molybdenum coated glass substrate at the Helmholtz Zentrum Berlin (HZB). [105].

E) A $Cu_2ZnSnSe_4$ thin film that was produced by the selenization of a sputtered metal precursor on a glass substrate at the HZB.

F) A $Cu_2ZnSnSe_4$ single crystal that was grown at the University of Delaware (UD) [18]

Despite all the difference in the deposition techniques, in the substrates and in the morphology of the samples, they exhibit mobilities with the fingerprint of charge carrier localization (real part of the mobility increases with frequency) and the DC-mobilities that were modeled by the Drude-Smith model are between 70 cm^2/Vs and 144 cm^2/Vs. Therefore, the charge carrier localization and a sum-mobility of $\approx$ 100 cm^2/Vs are characteristic for $Cu_2ZnSnSe_4$ in general. Only for complete substitution of selenium with sulfur, we found in [4] a lower sum-mobility of 32 cm^2/Vs.

Finally, the sum mobilities in $Cu_2ZnSnSe_4$ are compared in Figure 6.9c to other photovoltaic materials that were probe in with the same TRTS [7-18]. It shows that the sum mobility in $Cu_2ZnSnSe_4$ is relatively high, especially when compared to metal oxides, which have sum mobilities of $\sim$0.1 cm^2/Vs. The sum mobility in $Cu_2ZnSnSe_4$ is also approximately a factor of three higher than in halide-perovskites, which

are the current shooting star in photovoltaics. Therefore, the mobility in $Cu_2ZnSnSe_4$ can be considered relatively high although it is for example significantly below the 2200 cm^2/Vs for InP.

The Distinction of Electron and Hole Mobility

However, charge carrier collection in a solar cell is usually limited by the minority charge carriers. Therefore, it is highly desired to derive the individual mobilities of electrons μ_e and of holes μ_h. Such a distinction was achieved by us in [5] by combining the TRTS-derived sum mobility μ_Σ with the ambipolar mobility μ_{am} that was derived from modeling TRTS transients in the previous section.

The recombination of charge carrier at a surface depends on the transport to the surface, which was discussed in detail in the previous section. Therefore, the modeling of TRTS transients yields the ambipolar diffusion coefficient D_{am} if surface recombination has a significant contribution to the decay of the TRTS transients. Such an ambipolar diffusion coefficient can be translated by the Einstein relation $D_{am} = \mu_{am}(k_BT/e)$ to an ambipolar mobility μ_{am}.

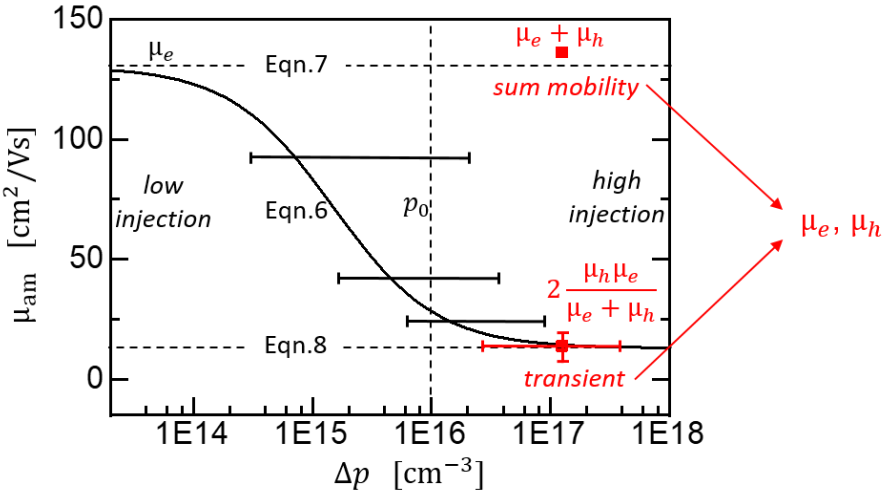

Figure 6.10: Individual mobilities of electrons and holes derived by TRTS. *a) The TRTS amplitude derives the sum mobility μ_{e+h} at terahertz frequencies. The TRTS transients depend on the ambipolar mobility μ_{am} of electrons and holes. The combination of both can yield the individual mobility of electrons and holes. b) The ambipolar charge carrier mobility depends on the photo-excited charge carrier concentration Δp and approaches a constant value for high injection.*

The contributions of electron mobility μ_e and hole mobility μ_h to the common ambipolar mobility $\mu_{am}(\Delta p)$ are determined by Equation (6.4), which depends on the photo-excited charge carrier concentration $\Delta p = \Delta n$ and the doping p_0. Such an injection-dependence of $\mu_{am}(\Delta p)$ is shown in Figure 6.10.

$$\mu_{am} = \frac{2\Delta p + p_0}{\frac{\Delta p}{\mu_p} + \frac{\Delta p + p_0}{\mu_n}} \tag{6.4}$$

This injection-dependence complicates the determination of the individual mobilities of electrons and holes. However, Equation (6.4) becomes independent of the injection in the limits of relatively large or small photo-excited charge carrier concentration Δp.

For low injection, $\Delta p << p_0\mu_p/\mu_n$, Equation (6.4) reduces to Equation (6.5) and the ambipolar charge carrier mobility is dominated by the minority carrier mobility. For high injection $\Delta n >> p_0$, Equation (6.4) reduces to Equation (6.6) and is dominated by the mobility of the carrier type with the smaller mobility. The transition between these two limits can be seen in Figure 6.10.

$$\mu_{am} = \mu_e \qquad for\ \ \Delta n \ll \frac{\mu_h}{\mu_e} p_0 \tag{6.5}$$

$$\mu_{am} = 2\frac{\mu_h \mu_e}{\mu_e + \mu_h} \quad for\ \ \Delta n \gg p_0 \tag{6.6}$$

For the $Cu_2ZnSnSe_4$ thin-film, an ambipolar diffusion coefficient of 0.35 cm^2/s was derived in the previous section from the modeling of the TRTS transients in high injection conditions. In combination with the sum mobility $\mu_\Sigma = \mu_e + \mu_h$ of *135 cm^2/Vs* ±25 %, it yields individual mobilities of 7.3 cm^2/Vs ±50 % and 128 cm^2/Vs ±25 %.

However, Equation (6.6) does not determine which of these two values corresponds to the electron mobility and which corresponds to the hole mobility. To distinguish them, we also modeled pairs of TRTS-transients at lower photo-excitation. This modeling is only a rough estimate as the ambipolar diffusion coefficient becomes injection-dependent and changes while the charge carrier concentration decreases by broadening of the distribution and recombination. However, the trend in Figure 6.10 is clear. It shows that the ambipolar mobility increases towards the lower injection levels where it is dominated by the minority carriers. Therefore, we conclude that larger mobility of 128 cm^2/Vs corresponds to electrons and that the smaller mobility of 7 cm^2/Vs corresponds to holes.

A similar analysis works for transients in the low injection limit where the effective mobility can directly be identified as the minority carrier mobility in Equation (6.5). The proposed method works on wafers as well as thin films. The only major requirement for the samples is relatively high surface recombination. If negligible surface recombination is present a sample may be treated by etching, oxidation, or ion bombardment to induce surface recombination.

Limits for the Intra-grain Transport

An important consequence of inequality if the electron and hole mobility is that the sum mobility is dominated by the electron contribution and that the behavior of the sum mobility allows drawing conclusions on the electron transport. In contrast, hole transport will remain mostly concealed.

The sum mobility is modeled in Figure 6.11a by the phenomenological Drude-Smith model for partially localized transport. However, the origin of this localization remained unknown. In general Drude-Smith-like mobilities can be explained by several physical models including plasmonic resonances (section 2.2.6), backscattering at barriers (section 2.2.5) [30], hopping across grain boundaries (section 2.2.4) [106], and the transport in potential fluctuations.

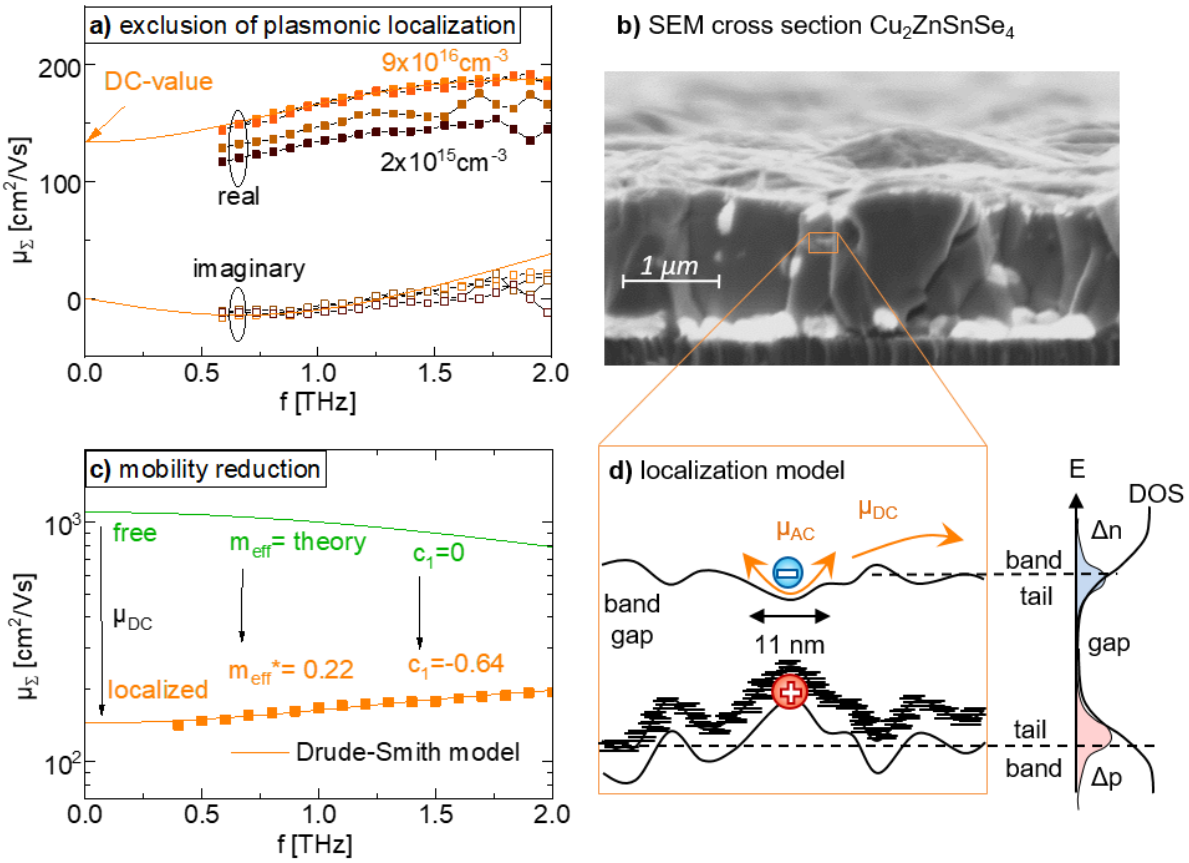

Figure 6.11: Identifying the origin of the carrier localization. *a) Charge carrier mobility at THz frequencies f is modeled by the Drude-Smith equation and its injection dependence excludes a plasmonic localization. b) Secondary electron microscopy (SEM) picture of the $Cu_2ZnSnSe_4$ thin film with grain sizes of ~ 1µm. c) Illustration of the intra-grain localization of charge carriers which favors alternating transport (AC) within the potential fluctuations over direct transport (DC) over the potential barriers. d) Estimating the loss in mobility due to charge carrier localization.*

Plasmonic resonances are an effect of the charge carrier cloud, whereas the other localization effects can be described on the level of individual charge carriers. Plasmonic resonances can occur when charge carriers are confined in a relatively large volume and would be in general in line with confinement of charge carrier in the individual grains of the polycrystalline thin film, which can be seen in the secondary electron microscopy (SEM) picture of the probed $Cu_2ZnSnSe_4$ thin film in Figure 6.11b.

However, the resonance frequency f_0 of the plasmonic localization increases with the square root of charge carrier concentration in Equation (2.29). In Figure 6.11a no such shift of the mobility spectrum

to higher frequencies is observed with increasing carrier concentration. Therefore, a plasmonic localizations can be ruled out and localization on the level of the individual charge carriers has to be present in $Cu_2ZnSnSe_4$.

The next localization model that can be explained is tunneling or hopping between quantum confined states. In such a case, the lower DC-mobilities are typically below 1cm^2/Vs [29] [29] [107] and the increase of the imaginary part of the mobility at higher frequencies cannot be modeled by the equation (2.28) of the tunneling model.

However, the spatial extent of the localization can be approximated by the scattering length of the charge carriers and maybe indicate the nature of the confinement. The scattering time of the charge carrier is caused by scattering at phonon and at the boundaries of the confinement. It can be assumed that the scattering at the boundary dominates when the derived mobility exhibits localization. Under this assumption, the charge carrier travels ballistic with its thermal velocity $v_{th} = (3k_BT/m_{eff})^{0.5}$ until it scatters at the confinement boundary after the scattering time τ_{scat}. This consideration estimates a scatting length l_{scat} in Equation (6.7), which is 11 nm for the scattering time and the effective transport mass that were derived by the Drude-Smith modeling of the measured charge carrier mobility.

$$l_{scat} = \tau_{sc}\sqrt{\frac{3k_BT}{m_{eff}}} \tag{6.7}$$

A spatial extent of the localization of ∼11 nm is far below the grain size of ∼1 µm of the polycrystalline thin film, which is shown in Figure 6.11b. Therefore, grain boundaries cannot be the origin of the observed charge carrier localization and the TRTS-derived mobility of 140 cm^2/Vs is an intra-grain mobility, which we reported in [4]. Additionally, we measured a sum-mobility of 144 cm^2/Vs in the $Cu_2ZnSnSe_4$ single crystal that was grown at the University of Delaware [18]. This value is almost identically with the values that were measured in the polycrystalline thin film and excludes a significant impact of grain boundaries.

Localization Model of Band Edge Fluctuations

These findings are in line with the model of electron transport in band-edge fluctuations [27] [30], which is illustrated in Figure 6.6d. The estimated spatial extent of the localization of ∼11 nm can be attributed to the potential fluctuations. Such a spatial extent fits the observed trapping times of ∼2ps that were revealed by the ultra-fast measurement in Section 6.2. Within 2 ps, electrons with a derived mobility of ∼128 cm^2/Vs diffuse ca. 26 nm by Brownian motion. Such a length $L = (2\mu k_BTt)^{0.5}$ is the standard deviation of the charge carrier from its initial position. This distance is significantly larger than the estimated average localization length of 11 nm and would allow carriers to trap into the extrema of the potential fluctuation.

The slightly higher mobilities for higher injection levels as observed in Figure 6.6a could be explained by filling the potential fluctuations. Alternatively, also heating by the pump beam may cause thermal activation out of the localized states.

The much smaller hole mobility of only ~7 cm^2/Vs ±50 % can be explained by band edge fluctuations that are larger for the valence band than for the conduction band, which is illustrated in Figure 6.7d. Alternatively, hole transport may occur in an acceptor band, which was proposed in [81] and similar hole mobilities of 5 cm^2/Vs were reported for transport in an acceptor band in GaAs [108].

Mobility Reduction

The modeled DC-value of the sum mobility of 144 cm^2/Vs ± 20 % is significantly smaller than the value that is derived for free transport (c_1=0) of charge carriers with the effective mass that is derived by density functional theory for the band-tail free $Cu_2ZnSnSe_4$ in [109]. The effective mass for electrons m_e of 0.08 and for hole mass m_h of 0.2 result in DC-mobilities in a tail-free $Cu_2ZnSnSe_4$ semiconductor of ca. 1100 cm^2/Vs for electrons and of 450 cm^2/Vs for holes, which is shown in Figure 6.7c. These values are based on the scattering time of 50 fs that was derived from the measured mobility. For a localization-free and band-tail-free semiconductor, these scattering time will likely increase further and increase the charge carrier mobilities further. Therefore, we estimate that band tails in $Cu_2ZnSnSe_4$ reduced the mobilities approximately by one order of magnitude.

6.5 Impact of Cu-Zn Disorder

One of the most common explanations for band tails in kesterite semiconductors is the disorder in the Cu-Zn sub-lattice which was reported in [73] [75] [110] and is illustrated in Figure 6.12a. Therefore, we probed the impact of such Cu-Zn disorder on the charge carrier dynamics in $Cu_2ZnSnSe_4$ thin that was produced at NREL.

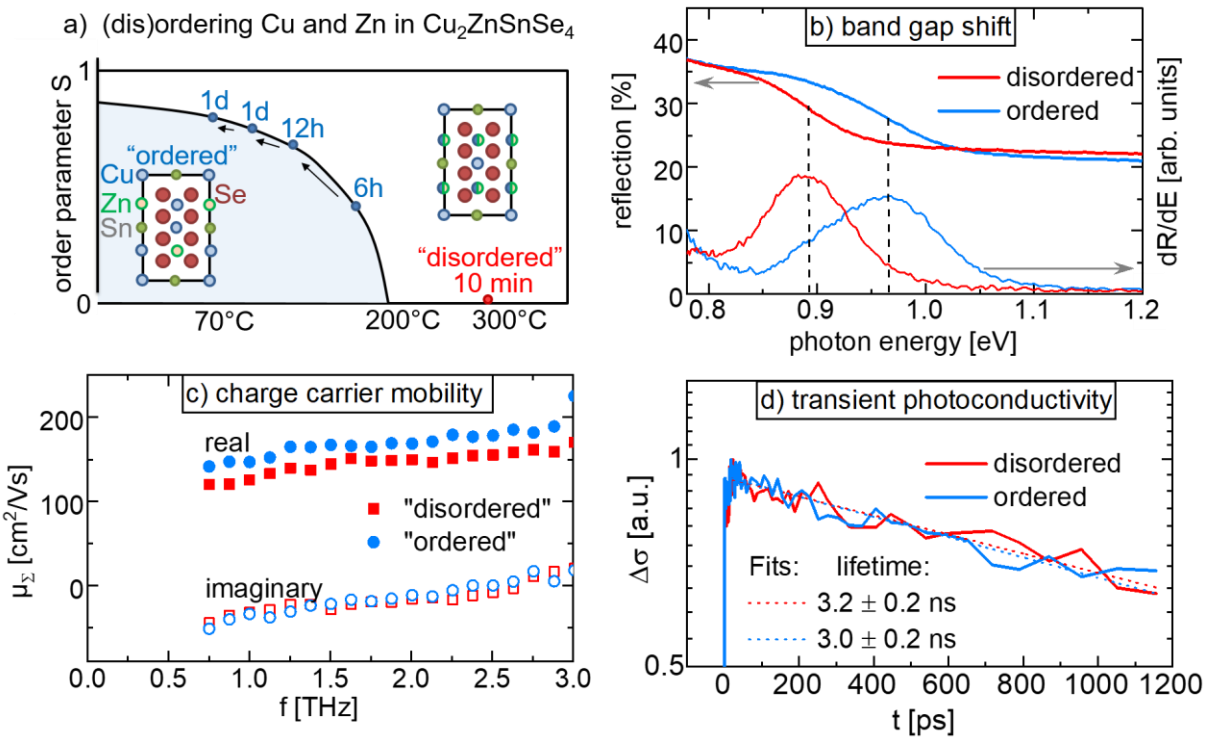

Figure 6.12: Impact of Cu-Zn disorder on charge carrier dynamics. *a) Illustration of the preparation of $Cu_2ZnSnSe_4$ thin films with different degrees of Cu-Zn disorder. The "ordered" sample has more (no complete) order on the Cu and Zn lattice sites than the "disordered" sample. b) The infrared reflection of the thin films shows in its first derivative dR/dE a shift of the bandgap, which is indicative of different degrees of Cu-Zn disorder. c/d) Charge carrier mobilities and the transients of the photoconductivity of "ordered" and "disordered" sample*

The degree of Cu-Zn disorder can be altered by thermal treatments. It was shown that Cu and Zn disorder completely in $Cu_2ZnSnSe_4$ for temperatures above ca. 200°C. Therefore, the sample was annealed in a nitrogen atmosphere for 10 minutes at 300 K. Afterwards it was quickly quenched to room temperature to prevent ordering and to freeze in the disorder. However, the derived "disordered" sample will not be completely disordered, which could correspond to an ordering parameter *S* of 0 and to a random occupation of the Cu-Zn sub-lattice. This "disordered" sample was characterized, transformed it into an "ordered" sample and characterized again. To order the sample, it was annealed at the temperature sequence illustrated in Figure 6.12a at relatively long times. However, the Cu-Zn ordering is a second-order transition and the ordering parameter S does not reach unity at room temperature. Therefore the "ordered sample" is in fact not completely ordered.

It has been reported in [111] that the bandgap changes from such "disordered" to "ordered" $Cu_2ZnSnSe_4$ samples. Therefore the bandgap shift is an ideal tool to verify that our "ordered" and "disordered" sample indeed have different levels of Cu-Zn disorder. To this end, the reflection of both samples was measured in an Ulbricht's sphere, which is shown in Figure 6.12b. These reflections

exhibit an additional contribution at lower photon energies that originates from light that is reflected at the molybdenum back contact of the sample. For higher photon energies this contribution is not observed because this light is absorbed in the thin film and is only reflected at the front interface. Here, the onset of this additional contribution from the back interface is quantified by the derivative of the reflection *dR/dE*, which roughly corresponds to the bandgap energy in Figure 6.12b. The comparison of the reflection of the "ordered" and of the "disordered" sample shows that the bandgap shifted by ~70 meV. This behavior confirms that both samples have a significantly different level of Cu-Zn disorder.

The charge carrier recombination and transport of the $Cu_2ZnSnSe_4$ thin film in the "ordered" and the "disorder" state were probed by reflection TRTS. The transients in Figure 6.12c and the charge carrier mobilities in Figure 6.12d do not differ significantly and the changes are within the typical level of reproducibility of measurements that were performed on different days.

This behavior indicates that the Cu-Zn disorder has no significant impact on the charge carrier recombination and on the sum mobility. The potential fluctuations and the localization of charge carriers are therefore not caused by Cu-Zn disorder, which is in line with other recent publications [73] that report no impact of the Cu-Zn disorder on the band tails in $Cu_2ZnSnSe_4$. The band tails and the charge carrier localization have to be attributed to another origin, such as electrostatic fluctuations from charged defects [82] [83], fluctuations of the stoichiometry, nm-scale inclusions of secondary phases as $Cu_{2-x}Se$, $SnSe_2$, $CuSnSe_3$ or ZnSe [112], $Cu_2ZnSnSe_4$ domains with different type structures [113], micro-strain [114] and thermal lattice vibrations [115].

It should be noted that measurements in this section were performed on the $Cu_2ZnSnSe_4$ thin film on molybdenum and therefore probe the front side of the $Cu_2ZnSnSe_4$ film. In contrast, the transient measurements in Section 6.3 were performed after lift-off and therefore on the backside. The differences in the observed transients indicate that the recombination differs for front and back.

7 Limitations of the Photovoltaic Performance

The charge carrier dynamics in $Cu_2ZnSnSe_4$, which were characterized in the previous sections, can now be interpreted in the light of photovoltaic application.

To this end, we will compress in Section 7.1 the rather complex recombination kinetics into effective charge carrier lifetime. In section 7.2 the effective lifetime will be identified that corresponds to the recombination in an operating solar cell.

The derived charge carrier mobilities and lifetimes will be used in Section 7.3 to estimate the open-circuit voltage and in Section 7.4 to estimate the short circuit current that the $Cu_2ZnSnSe_4$ thin film can supply in a finished solar cell.

These estimations will be compared to the values that are derived in the "Shockley Queisser limit" and that are measured on the finished solar cell. The differences between them indicate the losses in the photovoltaic material.

The theoretical background to this chapter was introduced in Chapter 3.

7.1 Matching Excitation Conditions

TRTS measurements are usually performed at relatively high injection levels to obtain a high signal to noise ratio. However, the recombination and the transport in a material can be injection dependent, which was discussed in theory in Sections 2.3-4 and was shown experimentally in for $Cu_2ZnSnSe_4$ in Figure 7.1. Therefore, the charge carrier concentration that is induced by pulsed excitation during the TRTS measurement has to be matched to the charge carrier concentration that is induced by continuous excitation in an operating solar cell.

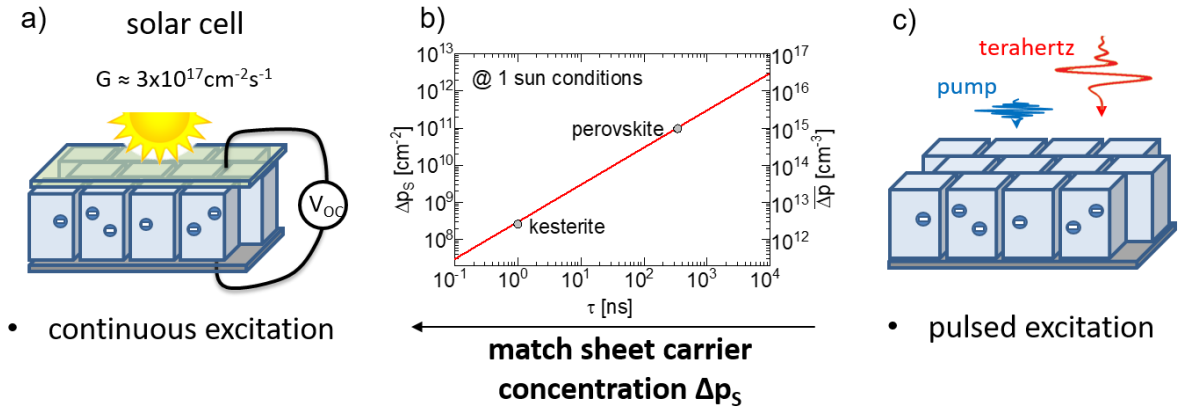

Figure 7.1: Matching excitation of TRTS to an operation solar cell. *a) Illustration of the continuous excitation of a solar cell by the sun with a photon current G. b) Excited sheet charge carrier concentration Δp_S in a solar cell absorber with a charge carrier lifetime τ. The corresponding charge carrier concentration Δp is given for a homogenous excitation of a 1µm thick absorber. c) Illustration of the pulsed excitation during a TRTS measurement.*

Charge carriers in a solar cell are continuously excited by the solar spectrum. The generation current *G* can be calculated by Equation (3.1) from the absorption of the AM1.5G spectrum and is approximately $3.1*10^{17}$ cm^2/s for a bandgap of 1 eV.

A continuous excitation results (for times long after switching the excitation on) in a steady-state, in which the excited charge carrier concentration is spatially and temporally constant. In this steady-state

the generation current G is balanced by a recombination current $R = \Delta p_S/\tau$, which can be described by an effective charge carrier lifetime τ. It yields an excited sheet charge carrier concentration of $\Delta p_S = G\tau$. The corresponding charge carrier concentration for a homogenous distribution throughout the absorber thickness d is given by Equation (7.1). Both concentrations depend on the effective lifetime of the charge carriers in the photovoltaic material and are shown in Figure 7.1 for a typical thickness d of 1 µm.

$$\Delta p = \frac{G\tau}{d} \tag{7.1}$$

A lifetime of 1 ns, which are typical for a kesterite thin film, yields an excited sheet charge carrier concentration of $3*10^8$ cm^{-2}. This value corresponds to the photon flux per pump pulse with which the sample should be excited to be in a comparable excitation as the solar cell under continuous excitation of the solar spectrum. If additionally a typical thickness of 1 µm is assumed, Equation (7.1) yields an excited charge carrier concentration of $3*10^{12}$ cm^{-3} in the solar cell.

Unfortunately, the lowest excited charge carrier concentration that yields detectable TRTS signal on a sample with a mobility of ~100 cm^2/Vs by our setup is $\approx 10^{11}$ cm^{-2} (or $\approx 10^{15}$ cm^{-3}). Hence, it is not possible to measure the kesterite thin film at 1 sun conditions by our TRTS setup and the lifetime estimation has to be conducted at higher injection levels.

However, a sample with a larger effective decay-time of ca. 1 µs has an excited charge carrier concentration of $3*10^{15}$ cm^{-3} under 1 sun conditions. Such long decay-times were found for example in perovskite thin films [9]. Therefore the transients of these samples can be measured at 1 sun conditions.

This matching of the excitation can be performed in practice by an iterative approach: Initially, the lifetime is measured at a certain injection level. This lifetime yields in Equation (7.1) the charge carrier concentration at 1 sun conditions and the lifetime is measured again at this injection level. This circle is repeated until the lifetime yields the same excitation level in Equation (7.1) at which it was measured.

7.2 Effective Lifetime

The recombination of charge carriers in a solar cell can be described by an effective charge carrier lifetime, which was discussed in the previous section. However, the decays of transient measurements such as TRTS can seldom be described by a single lifetime. Therefore, a method is required to derive an effective lifetime from the measured transients even if they exhibit a non-exponential decay.

An exponential decay is described in Equation (7.2) by a single lifetime τ. It corresponds to a recombination rate that depends in first-order (linear) on the excited charge carrier density Δp.

$$\Delta p(t) = \Delta p_0 exp\left(-\frac{t}{\tau}\right) \quad \leftrightarrow \quad \frac{d\Delta p(t)}{dt} = -\frac{1}{\tau}\Delta p(t) \tag{7.2}$$

However, the transients that were measured by TRTS on $Cu_2ZnSnSe_4$ are not single exponential. This behavior is shown in Figure 7.2, in which the logarithmic plot would yield a straight line for a single exponential decay. In such cases, the decay can be described by Equation (7.2), but with a time-dependent lifetime $\tau(t)$, which is given by:

$$\tau(t) = -\Delta p(t)\left[\frac{d\Delta p(t)}{dt}\right]^{-1} \tag{7.3}$$

Multi-exponential decays can be caused by various recombination processes that cannot be described by a single lifetime. In the theory Section 2.3 it was shown that the recombination processes as surface recombination, radiative recombination and Auger recombination are usually no first-order process and even the Shockley-Read-Hall recombination can have an injection-dependent charge carrier lifetime.

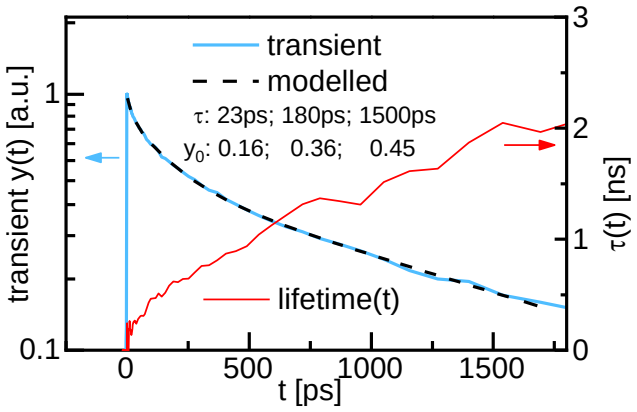

Figure 7.2: Defining a lifetime for multi-exponential decays. *a) A TRTS transient of $Cu_2ZnSnSe_4$ is modeled with the sum of three exponential decays. Such multi-exponential decays can also be described by a single exponential decay and a time-dependent lifetime τ(t).*

Additionally, non-exponential transients may be linked to kinetics that are not connected to charge carrier recombination. Such examples were discussed in Section 5.3.2 and include the decay of the charge carrier mobility for TRTS and TRMC or the spatial separation of electron and hole distribution or TRPL.

The issue of non-exponential decays can be solved by the in-depth characterization of the underlying recombination processes or by a relatively simple phenomenological approach.

An ***in-depth characterization*** of the charge carrier recombination was performed in the previous Section 6.3 and derived a bulk-lifetime of 4.4 ns and a surface recombination velocity of $6*10^4$. Therefore, surface recombination is the origin of the multi-exponential decay that is observed in Figure 7.2. The influence of a mobility decay was excluded in Section 6.2 for times that are later than 2 ps after excitation.

It was shown in [101] that the combination of bulk and surface recombination yields an effective lifetime that is described by Equation (7.4). It contains the bulk lifetime τ_B, the diffusion time to the surface $\tau_D = \pi^2 D_{am}/L^2$ and the capture time at the surface $\tau_S = L/(2S)$.

$$\frac{1}{\tau(t)} \approx \frac{1}{\tau_B} + \frac{1}{\frac{L(t)}{2S} + \frac{L(t)^2 1}{\pi^2 D_{am}}} \tag{7.4}$$

The length *L* is characteristic for the depth of the charge carrier distribution. Right after pulsed excitation, the characteristic depth *L* corresponds to the penetration depth 1/α. Over time, charge carriers diffuse into the bulk (as was exemplary modeled in Figure 6.8a) and their characteristic depth increases towards the layer thickness $L(t) \rightarrow d$. This behavior explains the time-dependent decay-times for the probed $Cu_2ZnSnSe_4$ thin film.

In a solar cell, the charge carriers are in approximation distributed throughout the thickness of the absorber. Therefore, the average distance to the surface can be assumed to be of half the layer thickness. Taken this value for L and the ambipolar diffusion coefficient given by Equation (6.4) at an injection level of $\sim 10^{12}$ cm^{-3}, a lifetime of 0.67 ns is derived.

Alternatively, a ***phenomenological effective lifetime*** can be estimated. This approach has the advantage that it does not require extensive analysis and is especially suited for the relative comparison of samples, where no absolute numbers are required.

To derive such an effective lifetime, transients are often modeled by a sum of single-exponential decays according to Equation (4.4).

$$y(t) = \sum_{i=1}^{k} y_{0i} \exp\left(-\frac{t}{\tau_i}\right) \tag{7.5}$$

This model can be imagined as several populations of charge carriers that do not interact and that recombine with individual lifetimes τ_i. A physical example would be a polycrystalline thin film with different lifetimes in the individual grains. If these grains are isolated from each other by large potential barriers at their boundaries a multi-exponential decay would be derived on average. However, this

model can also be generalized as a phenomenological model which describes decays where the recombination process is unknown.

The effective decay-time of such a multi-exponential decay can be defined in Equation (7.6) by the average of the individual decay-times τ_i which are weighted with their individual amplitudes y_{0i}.

$$\tau_{eff} = \frac{\sum_{i=1}^{k} y_{0i}\tau_i}{\sum_{i=1}^{k} y_{0i}} \tag{7.6}$$

The example transient in Figure 7.2 can be model by a sum of three exponential decays with amplitudes of 0.15; 0.36 and 0.46 and decay-times of 23 ps, 179 ps, and 1500 ps, respectively. They yield an effective decay-time of 0.78 ns.

Such a charge carrier lifetime is relatively low compared to halide-perovskites, which exhibit lifetimes up to ~1 µs [9].

7.3 Limits for the Open Circuit Voltage

The quasi-Fermi level splitting (QFLS) and the corresponding open-circuit voltage of a photovoltaic material can be estimated by different approaches, namely from the internal properties, from quantitative photoluminescence measurements, from the open-circuit voltages of the finished $Cu_2ZnSnSe_4$ solar cell and from the so-called Shockley-Queisser limit. The difference between these estimations will reveal the losses by band tail occupation and non-radiative recombination.

The ***internal properties*** of the $Cu_2ZnSnSe_4$ thin-film allow estimating the voltage of a finished solar cell by Equation (2.11), which for convenience is stated in Equation (7.7) again. It contains the bandgap E_G, the absorbed photocurrent G, the thickness of the absorber layer d, the doping p_0, the charge carrier lifetime τ and the effective density of states for the conduction band N_C and for the valence band N_C.

$$qV_{OC} \approx \Delta E_F = E_G + k_B T * ln\left(\frac{\frac{G\tau}{d}\left[\frac{G\tau}{d} + p_0\right]}{N_C N_V}\right) \tag{7.7}$$

For the probed $Cu_2ZnSnSe_4$ thin film, an effective bandgap of 0.97 eV was estimated, in Section 6.1. The absorbed photon current G is calculated from the absorption of the $Cu_2ZnSnSe_4$ thin film and the AM1.5G sun spectrum and amounts to $3.17*10^{17}$ photons/cm^2/s. The thickness of the $Cu_2ZnSnSe_4$ thin film is 1.55 µm, which was measured by a profilometer. To this end, the thin film was scratched down to the molybdenum substrate and the depth of the scratch was measured. The effective charge carrier lifetime was estimated in the previous section with 0.78 ns. The values yield an excited charge carrier

concentration $\Delta n = G\tau/d$ of 1.6*10^{12}cm^2/Vs, which dominates the electron concentration in the p-type $Cu_2ZnSnSe_4$ thin film. The hole concentration is dominated by the doping of 10^{16}cm^{-3}, which was measured for the thin film by capacitance-voltage measurement by coworkers at NREL [4]. The effective density of states can be calculated by equations (2.5-6) from the effective mass of electrons in the conduction band of 0.08 and of holes in the valence band of 0.2, which are taken from the literature [109]. The derived effective density of conduction band states is 5.7*10^{17}cm^{-3} and the effective density of the valence band states is 2.2*10^{18}cm^{-3}. These values derive a quasi-Fermi level for the electrons of 330 meV below the conduction band edge and a quasi-Fermi level for the holes of 140 meV above the valence band edge. Finally, they combine in Equation (7.7) to a QFLS of 500 meV and a corresponding open-circuit voltage of 500 mV.

It should be noted that band tails are not explicitly included in the estimation of the open-circuit voltage that is stated above. In particular, the effective density of band tail states was not included and therefore, the derived QFLS can be attributed to a $Cu_2ZnSnSe_4$ sample without an occupation of band tails, which will be discussed further below.

The ***quantitative photoluminescence*** (Q-PL) was measured on the bare $Cu_2ZnSnSe_4$ thin film for excitation with a 660 nm laser at a photon current of 3.2*10^{17} photons/cm^2/s, which is equivalent to the conditions at 1 sun. The Q-PL yields the absolute emitted photon current in units of photons/cm^2/s/eV, which is shown in Figure 7.3a. This spectrum is modeled by Plank's generalized law (3.3), which yields a quasi-Fermi level splitting of 395 meV.

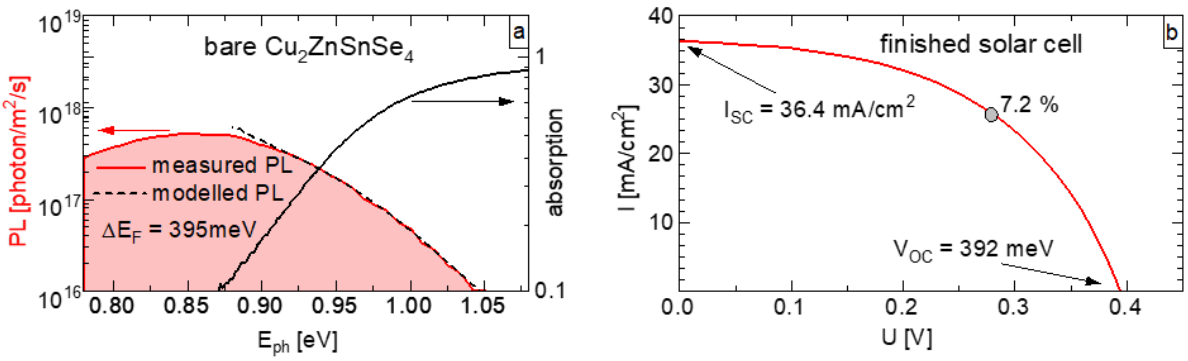

Figure 7.3: Alternative measurements of the quasi-Fermi level splitting at 1 sun. *a) Quantitative photoluminescence of the $Cu_2ZnSnSe_4$ thin film that was measured under 1 sun equivalent excitation and that was modeled by Plank's generalized law with a quasi-Fermi level splitting ΔE_F of 395 meV. b) The current I – voltage U curve of the finished $Cu_2ZnSnSe_4$ measured in a sun simulator.*

The ***current-voltage curve*** of the finished $Cu_2ZnSnSe_4$ solar cell was measured in a sun simulator. It exhibits an open circuit voltage of 392 meV in figure 7.3b. The processing of the solar cell was processed at NREL, which is described in detail in [68]. The open-circuit voltage of the finished solar cell of 392 meV is in close agreement with the QFLS of 395 meV that was measured by Q-PL on the

bare $Cu_2ZnSnSe_4$ thin film. This agreement shows that the QFLS inside the absorber layer is the limitation of the open-circuit voltage of the finished solar cell and that the processing of the bare absorber into a finished solar cell does not affect the QFLS significantly.

Finally, the ***Shockley-Queisser limit*** yields a QFLS of 739 meV for a bandgap of 0.97 eV, which was derived in the theory Section 3.2.2.

The comparison of these different estimations of the QFLS will in the following reveal the losses by non-radiative recombination and by band tail occupation, which is illustrated in Figure 7.4

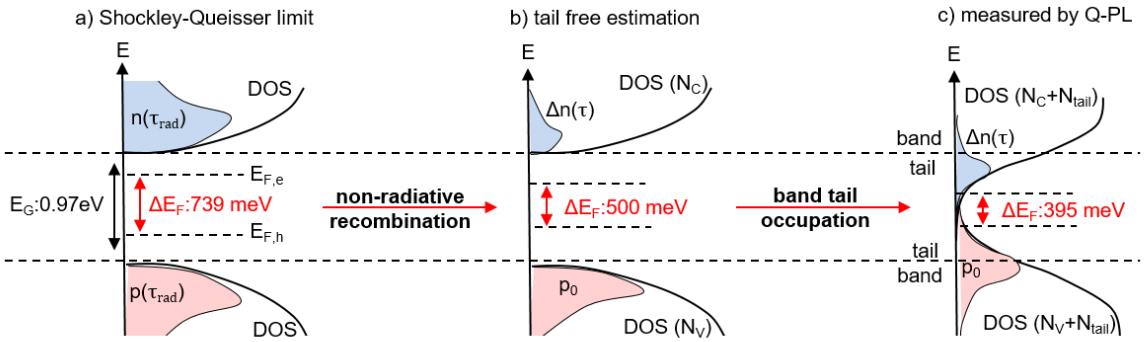

Figure 7.4: The impact of non-radiative recombination and band tail occupation on the quasi-Fermi level splitting (ΔE_F). *Illustrations of the distributions of electrons (n) and holes (p) over the density of states (DOS). The corresponding Fermi levels of electrons $E_{F,e}$ and of the holes $E_{F,h}$ define the quasi-Fermi level splitting ΔE_F. a) The Shockley-Queisser limit assumes the absence of band tails and exclusive radiative recombination with a radiative charge carrier lifetime τ_{rad}. b) The estimation from internal properties with the measured (non-radiative) lifetime τ but with the tail-free effective density of states for the conduction band N_C and for the valence band N_V. c) The QFLS measured by quantitative photoluminescence (Q-PL) corresponds to the real situation with the band tail present. The effective density of states of the band tails N_{tail} has to be included.*

Loss due to non-radiative recombination is derived by comparing the QFLS of the Shockley-Queisser limit and the estimation from the tail-free internal properties, which are illustrated in Figure 7.4a/b.

The Shockley-Queisser limit assumes the absence of band tails because its absorption is zero below the bandgap energy. The excited charge carrier concentration Δn is determined exclusively by radiative recombination and by the corresponding radiative lifetime τ_{rad}.

The tail-free estimation from the internal properties also assumes that no band tail states are occupied but the excited charge carrier concentration Δn is determined by the measured charge carrier lifetime τ, which is usually dominated by non-radiative recombination.

Therefore, the difference in their QFLS of 239 meV can be attributed to non-radiative recombination. In Section 6.3 it was shown that the observed transients are in line with Shockley-Read-Hall

recombination at a discreet deep trap state. Therefore, no proof is found that the band tails contribute to this recombination.

Loss due to the occupation of band tails is derived by comparing the QFLS of the tail-free estimation from the internal properties to QFLS that was measured by Q-PL.

The Q-PL measures the QFLS that is present in the photovoltaic sample and contains no assumptions on the presence or absence of a band tail.

The difference of 105 meV between the tail-free estimation and the measurement can be attributed to the occupation of band tails, which is illustrated in Figure 7.4b/c. A similar deviation was found between simulations of the open-circuit voltage of a solar cell in the software SCAPS and the open-circuit voltage that was measured on a similar $Cu_2ZnSnSe_4$ solar cell [15].

Such an impact of band tails on the estimation of the QFLS can be described in three ways, which differ in their definition of the charge carrier concentrations p and n, but yield the same result.

The first approach regards all electrons and holes in the concentrations n and p regardless of whether they are in the band tail or in the band states. In this case, the effective density of states $N_{eff} = N_{band} + N_{tail}$ should include the contribution of the band tails N_{tail} as well as the contribution of the bands N_{band}.

The second approach only regards the electrons and holes in charge carrier concentrations n_{band} and p_{band} that are in the band states. Charge carriers that are trapped in the tail states are excluded. In this case, the effective density of states should only include band states. However, the excited charge carrier concentration Δn and the doping p_0 have to be reduced to the faction x of charge carriers that are in the band states by $\Delta n_{band} = x\Delta n$ and $p_{0\text{-}band} = xp_0$. The charge carriers that are in the tail states have to be excluded. The reduction of the excited charge carrier concentration $\Delta n = G\tau/d$ can be modeled by a reduction of the charge carrier lifetime τ, which was discussed in Section 2.3.3. Such a reduced lifetime $\tau_{band} = x\tau$ corresponds to the time the charge carriers actually spend in the band states. The time that they are trapped in the tail states is excluded.

In our earlier publication, a third phenomenological approach was followed. Usually, the photoluminescence in a tail-free semiconductor peaks a few meV above the bandgap energy. However, in Figure 7.3a it peaks at 0.85 meV, which is 120 meV below the estimated bandgap. Therefore, this behavior may be interpreted phenomenologically as a reduction of the effective bandgap and the photoluminescence maximum may be used instead of the bandgap to estimate the quasi-Fermi level splitting in Equation (7.7). In [15] we combined this reduced bandgap with a reduced

lifetime to derive a quasi-Fermi level splitting from the internal properties that is in line with the measured value.

All of these three approaches explain the difference between the estimation of the QFLS from the tail-free internal properties and the measured QFLS by band tails.

However, a further difference between the methods is that the Q-PL analysis is based only on two measured quantities: namely the measurement of the light absorption and the measurement of the Q-PL, which both can be determined relatively precisely. In contrast, the estimation from the internal properties requires seven properties, which partially contain a rather large uncertainty. For example, in Section 7.2 it was shown that the lifetime of 0.78 ns was measured at higher carrier concentrations that are much higher than in an operating solar cell.

7.4 Limits for the Short Circuit Current

The short circuit current of a solar cell can be derived with different approaches, namely with the so-called Shockley-Queisser limit from the bandgap energy of the absorber; or from the absorption of the absorber; or from internal properties of the absorber or from the current of the finished $Cu_2ZnSnSe_4$ solar cell. The difference between the limits can be attributed to optical losses and charge carrier recombination.

The ***Shockley-Queisser limit*** derives the short circuit current from the absorbed photon current ϕ_{abs} of the solar spectrum and assumes a step-like absorption onset at the bandgap energy, which was shown in Figure 3.2. For the $Cu_2ZnSnSe_4$ thin film with a bandgap of 0.97 eV yields an absorbed photon current ϕ_{abs} of $3.1*10^{17}$ cm^2/s, which translates into a short circuit current $I_{SC} = e\phi_{abs}$ of 49.8 mA/cm^2.

Optical losses in a solar cell reduce the photon current that is absorbed in the absorber layer of the solar and subsequently short circuit current. Such optical losses included the incomplete absorption in the absorber material, the reflection of sun slight the front contact and the parasitic absorption in the front contact.

The absorption $\alpha = 1-exp(-\alpha d)$ that was measured on the $Cu_2ZnSnSe_4$ thin film is not a step-like absorption onset at the bandgap energy, which was assumed in the Shockley-Queisser limit. In comparison, it exhibits an incomplete absorption above the bandgap energy and an additional absorption below the bandgap energy due to the absorption tail. This measured absorption yields a short circuit current of 48.8 mA/cm^2, which differs from the value in the Shockley-Queisser limit by -1.0 mA/cm^2. Such a minor difference between both estimations shows that the absorption of the $Cu_2ZnSnSe_4$ thin film is sufficient. Therefore, the layer thickness d of 1.55 µm of the thin film is

adequate for the absorption coefficient α of the $Cu_2ZnSnSe_4$ thin-film, which shows that $Cu_2ZnSnSe_4$ is in principle suited for thin-film photovoltaics.

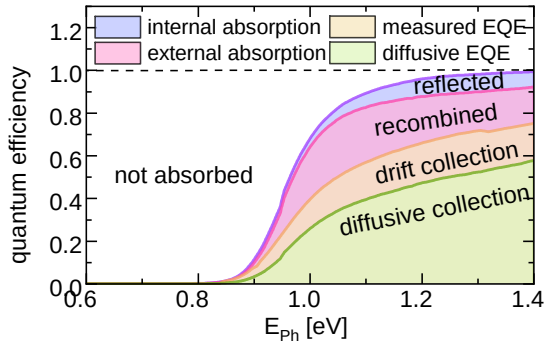

Figure 7.5: Limits and loss in the quantum efficiency (QE) of charge carrier collection. *The QE is fundamentally limited by the internal absorption of the photovoltaic material. The measured external quantum efficiency (EQE) on the finished solar cell is further reduced by the reflection on and absorption in the front contact and by the charge carrier recombination. The diffusive EQE was derived from the internal properties of the absorber layer.*

The loss of sunlight by the reflection from the finished solar cell was measured in an Ulbricht's sphere and is subtracted in Figure 7.5. This reflection reduces the current that is generated in the absorber layer and yields a short circuit current of 44.7 mA/cm^2, which differs from the short circuit current in the Shockley-Queisser limit by -4.1 mA/cm^2. Such a reflection loss can usually be minimized by an antireflection coating on top of the front contact of the solar cell.

The parasitic absorption in the front contact of a $Cu_2ZnSnSe_4$ solar cell is usually caused by a CdS buffer layer. The absorption of this layer sets in above its bandgap energy of ~2.4 eV and depends on its thickness. As this work focuses on the absorber properties, this loss was not modeled here.

The ***current-voltage characteristic*** of the finished solar cell exhibits in Figure 7.3 a short-circuit current of 36.2 mA/cm^2. It differs from the circuit current that is generated in the absorber by -8.5 mA/cm^2. This difference is caused mainly by the recombination of charge carriers before they can be collected at the contact layers and to a minor degree by the absorption in the CdS buffer layer. Such recombination of charge carriers is in competition with the collection of charge carriers by drift in the space charged region and by diffusion in the neutral region in the solar cell.

The corresponding external quantum efficiency (EQE) was measured by Charles J. Hages on the finished solar cell and is shown in Figure 7.5. It consists of the contribution of charge carrier collection by drift in the space charged region of the p-n junction of the solar cell and of the contribution of the diffusion in the neutral region.

The ***diffusive estimation*** of the short circuit current regards only the diffusive collection of the minority charge carriers, which was detailed in Section 3.3.1. Such a diffusive collection is described by the

diffusive EQE and can be calculated by Equation (3.4) from the thickness of the absorber layer d, from the absorption coefficient α and from the diffusion length L_{diff}. This diffusion length $L_{diff} = (\mu\tau k_B T/e)^{0.5}$ of the minority charge carriers is given by their mobility μ and their lifetime τ. For the $Cu_2ZnSnSe_4$ thin film, a minority carrier mobility of 128 cm^2/Vs and a lifetime of 0.78 ns were derived in Section 6.4 and Section 7.2 and yield a diffusion length of 0.51 µm. The estimated diffusive EQE is shown in Figure 7.5.

This diffusive EQE yields in Equation (3.4) a diffusive short circuit current of 31.5 mA/cm^2, which differs by -4.7 mA/cm^2 from the measured short circuit current.

The difference between the measured EQE and the diffusive EQE, and between the corresponding short circuit currents, can be attributed to the additional collection of charge carriers by drift in the space charged region.

8 Summary and Outlook

The presented work contributed to the photovoltaic research in three ways. First, it advanced and validated the application of time-resolved terahertz spectroscopy for the characterization of charge carrier lifetime and mobility in photovoltaic materials. Second, it integrated all aspects of charge carrier dynamics and optoelectronic properties for the band-tailed $Cu_2ZnSnSe_4$ into one narrative. Third, it reveals the limits and losses of $Cu_2ZnSnSe_4$ solar cells.

First, we address some concerns about the ***time-resolved terahertz spectroscopy (TRTS)*** with regard to its application on photovoltaic samples. To this end, its measurement modes (reflection vs. transmission) and analysis methods (thin-film approximation vs. transfer matrix method) were compared and approved on an InP wafer. Then, TRTS was theoretically and experimentally compared to alternative techniques. The TRTS-derived transients were compared to transients that were measured by time-resolved photoluminescence, time-resolved microwave conductivity and transient absorption. Its mobility was compared to Hall measurements and an analysis of the voltage-dependent internal quantum efficiency. Additionally, the excitation conditions of the TRTS measurement were compared and matched to the conditions in the operating solar cell.

TRTS was also advanced for the application on photovoltaic samples. It was shown in this work and the corresponding publication [3] that it can measure charge carrier mobilities in thin films on metal substrates, which are the prevalent architecture of photovoltaic thin-film samples. Further, it was shown here and in the corresponding publication [5] that the individual mobilities of electrons and holes are derived by combining TRTS transients and the usual TRTS-derived sum mobility. Such

distinction is especially important in photovoltaics because the charge transport in solar cells is usually limited by the minority charge carriers.

The ***charge carrier dynamics in $Cu_2ZnSnSe_4$*** were probed in-depth on a coevaporated thin film that was produced by the group of Ingrid Repins during my stay at the National Renewable Energy Laboratory (NREL) at conditions similar to the production of their record $Cu_2ZnSnSe_4$ solar cell. Thereby a comprehensive model of the full charge carrier dynamics was developed, which is shown in Figure 8.1.

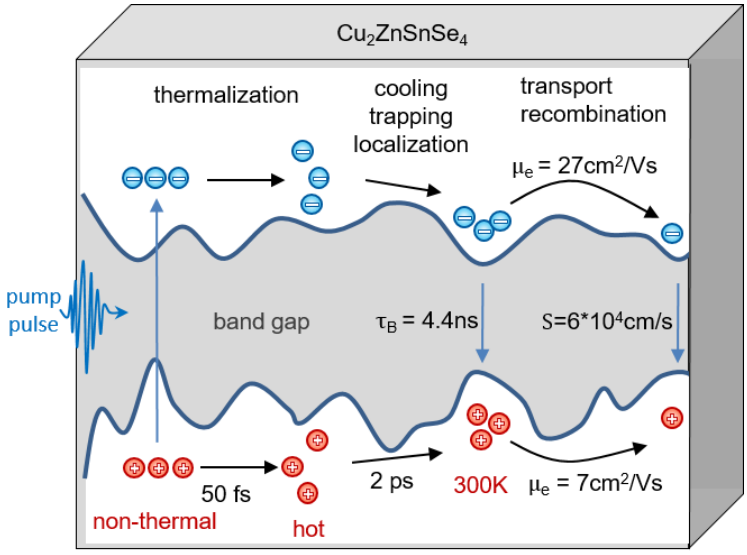

Figure 8.1: Charge carrier dynamics in $Cu_2ZnSnSe_4$. Illustration of the kinetic and optoelectronic properties of the $Cu_2ZnSnSe_4$ thin film that was probed throughout this work.

The ***ultra-fast dynamics*** start with the charge carrier scattering with a momentum relaxation time of 50 fs. This scattering is followed by the cooling of the hot charge carriers, their trapping into the tail states, their localization and the corresponding mobility decay, which are observed within the initial ~2 ps. The transition from bipolar to ambipolar transport of the photoexcited electron and hole distributions takes place within ~5 ps. After the initial few ps, the charge carriers are distributed in a common quasi-equilibrium over band and tail states.

The ***recombination*** of the photo-excited charge carrier in $Cu_2ZnSnSe_4$ can be characterized by a bulk charge carrier lifetime of 4.4 ns and by a surface recombination velocity of $6*10^4$ cm/s at high injection levels. At lower injection levels, which correspond to the conditions in a solar cell, the recombination increases. The recombination of higher-order has no impact at relevant injection levels.

The ***transport*** in the $Cu_2ZnSnSe_4$ thin film is characterized by an electron mobility of 127 cm^2/Vs and a hole mobility of 7 cm^2/Vs, which do not decrease further after the trapping in the initial 2 ps. These mobilities correspond to an intra-grain mobility in the ~1 µm sized grains the polycrystalline $Cu_2ZnSnSe_4$ thin film. However, the frequency-dependence indicates that the electrons are localized on ~11 nm and can be modeled in the phenomenological Drude-smith model with a localization

parameter of -0.65. The smaller mobility of the holes indicates that they may be even more localized. A comparison with 15 other photovoltaic materials that I probed throughout my time as a doctoral researcher shows that the sum mobility of $Cu_2ZnSnSe_4$ is relatively high. The these mobilities ranged from 0.1 cm^2/Vs for $SnWO_4$ to 2200 cm^2/Vs for InP and were published as co-author in [7] [8] [9] [10] [11] [12] [13] [14] [15] [4] [16] [17].

The impact of ***band tails*** in $Cu_2ZnSnSe_4$ and in kesterite type photovoltaic materials, in general, is a large debate in the community and was further clarified throughout this work. It was found in this work that the band tails lead to absorption tails that are in line with Gaussian bandgap fluctuations with a standard deviation of 55 meV.

Such band tails also explain the observe localization on the charge carriers and the mobility reduction by a factor of ∼10 compared to free charge carrier transport. The frequency-dependence indicates that the charge carriers are localized on average on ∼11 nm, which can be associated with the spatial extent of the band edge fluctuation. The smaller hole mobility indicates that the fluctuations in the valence band are larger than in the conduction band or that the holes transport in a defect band.

Further, the occupation of the band tails increases the effective density of states. Subsequently, the quasi-Fermi-level splitting in the material and the corresponding open-circuit voltage of the finished solar cell are reduced by ∼105 meV.

However, we found no unambiguous sign of the impact of the band tails on recombination, which is the major limitation of the photovoltaic performance of $Cu_2ZnSnSe_4$. The recombination could still be modeled by Shockley-Read-Hall recombination at a discrete trap level and no recombination kinetics that are typical for a distribution of band tails such as multiple trapping were observed.

Additionally, no impact of the Cu-Zn disorder that is often associated with the band tail was observed on the charge carrier mobility and lifetime in $Cu_2ZnSnSe_4$. Therefore, the Cu-Zn disorder could be excluded as the origin of the band tails.

The ***photovoltaic performance*** of the finished $Cu_2ZnSnSe_4$ thin-film solar cell is insufficient to compete with the established technologies as silicon (Si) and gallium arsenide (GaAs) as well as with the emerging halide-perovskite (MAPbI3) solar cells. In principle, $Cu_2ZnSnSe_4$ has a Shockley-Queisser limit of 31.4 %, which is only 2.2 % lower than the maximum value of 33.6 % at a bandgap of 1.15 eV. However, the certified record efficiency of 9.8 %, as well as the efficiency of 7.2 % that was measured in this work are much lower than the efficiencies that have been achieved by Si, GaAs and MAPbI3, which is shown in Figure 8.2a. This inferiority of $Cu_2ZnSnSe_4$ was attributed in this work to specific losses in the current and in the voltage, which are shown in Figure 8.2 b/c.

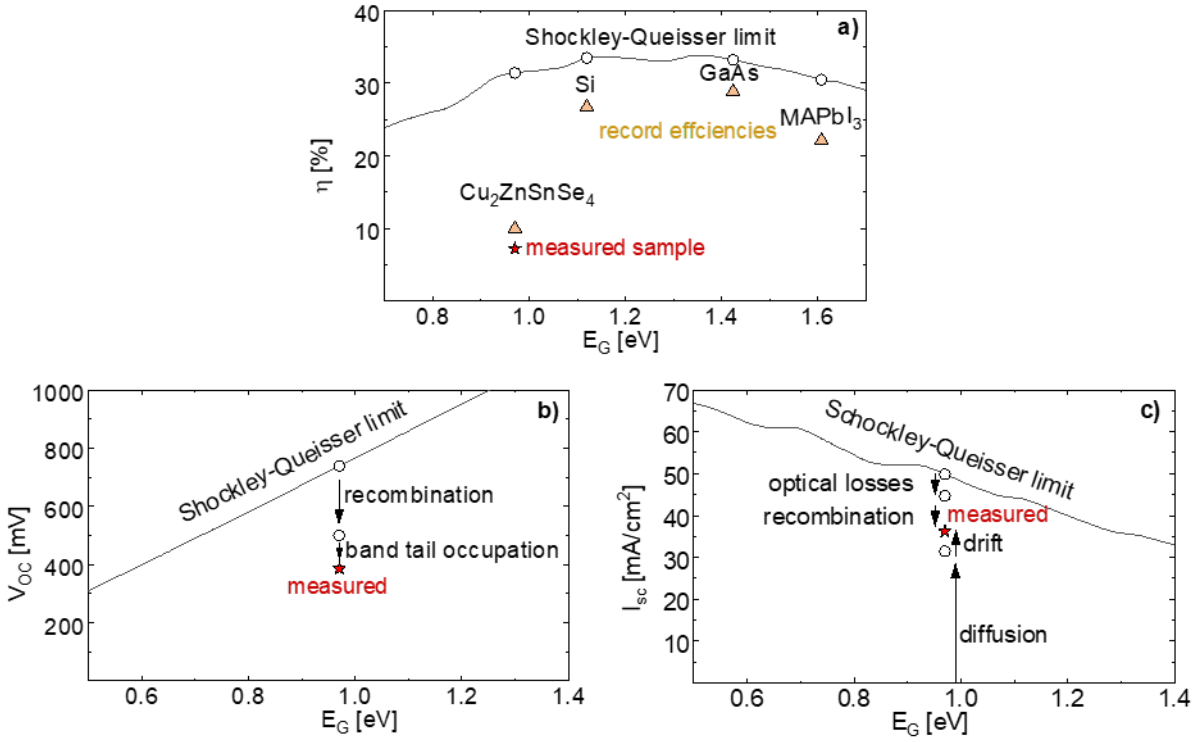

Figure 8.2: Photovoltaic limits and loss in $Cu_2ZnSnSe_4$ *a) The efficiencies of the finished $Cu_2ZnSnSe_4$ solar cell compared to the record efficiencies of more advanced materials and the Shockley-Queisser limit. b) The open-circuit voltage of the finished $Cu_2ZnSnSe_4$ solar cell and the losses compared to its Shockley-Queisser limit. c) The short circuit current of the finished $Cu_2ZnSnSe_4$ solar cell and the losses compared to its Shockley-Queisser limit.*

The loss in the open-circuit voltage of ~239 meV between the SQ limit and a band-tail-free estimation from the internal properties was attributed to charge carrier recombination and a low charge carrier lifetime. The loss of ~105 meV between the band tail free estimation of the open-circuit voltage and the measured open-circuit voltage was attributed to the occupation of band tails.

The short circuit current of the finished solar cell of 36.2 mA/cm^2 suffers losses of -13.6 mA/cm^2 compared to its Shockley-Queisser limit of 49.8 mA/cm^2. The incomplete absorption above the bandgap contributes -1 mA/cm^2 and the reflection of the sunlight at the solar cell -4.1 mA/cm^2. The remaining -8.5 mA/cm^2 are lost mainly due to charge carrier combination and to a minor fraction to parasitic absorption in the CdS buffer.

The measured short circuit current consists of contributions of diffusive collection of charge carrier and of the drift of charge carrier in the space charged region. An estimation of the short circuit current of 31.5 mA/cm^2 exclusively by diffusive collection indicates that the space charged region increases the short circuit current by ~4.7 mA/cm^2.

The ***outlook on $Cu_2ZnSnSe_4$ solar cells*** is rather challenging. The largest improvements in its current as well as in its voltage can be achieved by decreasing the charge carrier recombination and increasing

the corresponding lifetime. Therefore the observed surface recombination should be reduced by passivation of the surface. For this purpose band gap gradients by Ge or Ag alloying have been tested recently. Additionally, the bulk recombination has to be reduced to get into the region of the competing photovoltaic materials as $Cu(In,Ga)(S,Se)_2$ and MAPbI3, which exhibit lifetimes of up to ~1 µs [9]. However, recently no major improvement of the lifetimes in $Cu_2ZnSnSe_4$ was reported and it is unclear which defect causes the recombination.

A moderate increase in the voltage can be accomplished by a reduction of the effective density of tail states. The alloying of $Cu_2ZnSnSe_4$ with silver showed some promising results [116].

An increase in the mobility does not seem to be required to boast the current collection because the lifetime has to be increased anyway to enhance the voltage. With such an increased lifetime the measured minority carrier mobility of 127 cm^2/Vs in $Cu_2ZnSnSe_4$ should be sufficient [4]. For example, highly efficient perovskite solar cells have even lower sum mobilities of ~50 cm^2/Vs [9].

The ***outlook on TRTS*** for the characterization of photovoltaic samples is rather promising. Its abilities to contact-less measure charge carrier lifetime and mobility make it an ideal tool for screening large amounts of energy materials and to generate experimental material libraries. The compounds probed and published as a co-author in [7-18] represent the start of such an endeavor and can be used as a reference for the judgment on other novel photovoltaic materials.

Further, TRTS allows in combination with other spectroscopic techniques as the quantitative photoluminescence to estimate the achievable power conversion efficiency and the implied losses of novel photovoltaic materials. Such a framework should be extended by further work to measure the doping concentration and the absorption of the sample by contact-less mapping techniques. Terahertz spectroscopy offers a solution to these challenges. The doping concentration could be accessed by optical Hall-effect measurements, which are also a kind of terahertz spectroscopy and the absorption could be derived from TRTS with wavelength-dependent excitation in a similar way as in photoluminescence spectroscopy with wavelength dependent-excitation.

9 Appendices

9.1 References

[1] K. P. Bhandari, J. M. Collier, R. J. Ellingson and D. S. Apul, "Energy payback time (EPBT) and energy return on energy invested (EROI) of solar photovoltaic systems: A systematic review and meta-analysis," *Renewable and Sustainable Energy Reviews,* vol. 47, pp. 133-141, 7 2015.

[2] T. Kirchartz and U. Rau, "What Makes a Good Solar Cell?," *Advanced Energy Materials,* vol. 8, p. 1703385, 3 2018.

[3] H. Hempel, T. Unold and R. Eichberger, "Measurement of charge carrier mobilities in thin films on metal substrates by reflection time resolved terahertz spectroscopy," *Optics Express,* vol. 25, pp. 17227-17236, 2017.

[4] H. Hempel, A. Redinger, I. Repins, C. Moisan, G. Larramona, G. Dennler, M. Handwerg, S. F. Fischer, R. Eichberger and T. Unold, "Intragrain charge transport in kesterite thin films - Limits arising from carrier localization," *Journal of Applied Physics,* vol. 120, p. 175302, 11 2016.

[5] H. Hempel, C. J. Hages, R. Eichberger, I. Repins and T. Unold, "Minority and Majority Charge Carrier Mobility in Cu2ZnSnSe4 revealed by Terahertz Spectroscopy," *Scientific Reports,* vol. 8, p. 14476, 9 2018.

[6] H. Hempel, R. Eichberger, I. Repins and T. Unold, "The effect of Cu-Zn disorder on charge carrier mobility and lifetime in Cu2ZnSnSe4," *Thin Solid Films,* vol. 666, pp. 40-43, 11 2018.

[7] L. L. Baranowski, K. McLaughlin, P. Zawadzki, S. Lany, A. Norman, H. Hempel, R. Eichberger, T. Unold, E. S. Toberer and A. Zakutayev, "Effects of Disorder on Carrier Transport in Cu2SnS 3," *Physical Review Applied,* vol. 4, 10 2015.

[8] J. A. Marquez Prieto, S. Levcenko, J. Just, H. Hempel, I. Forbes, N. M. Pearsall and T. Unold, "Earth abundant thin film solar cells from co-evaporated Cu2SnS3 absorber layers," *Journal of Alloys and Compounds,* vol. 689, pp. 182-186, 12 2016.

[9] F. Staub, H. Hempel, J.-C. Hebig, J. Mock, U. W. Paetzold, U. Rau, T. Unold and T. Kirchartz, "Beyond bulk lifetimes: Insights into lead halide perovskite films from time-resolved photoluminescence," *Physical Review Applied,* vol. 6, p. 044017, 10 2016.

[10] M. Ziwritsch, S. Müller, H. Hempel, T. Unold, F. F. Abdi, R. Krol, D. Friedrich and R. Eichberger, "Direct Time-Resolved Observation of Carrier Trapping and Polaron Conductivity in BiVO4," *ACS Energy Letters,* vol. 1, pp. 888-894, 11 2016.

[11] J.-W. Jang, D. Friedrich, S. Müller, M. Lamers, H. Hempel, S. Lardhi, Z. Cao, M. Harb, L. Cavallo, R. Heller and others, "Enhancing Charge Carrier Lifetime in Metal Oxide Photoelectrodes through Mild Hydrogen Treatment," *Advanced Energy Materials,* vol. 7, p. 1701536, 8 2017.

[12] F. W. Souza Lucas, A. W. Welch, L. L. Baranowski, P. C. Dippo, H. Hempel, T. Unold, R. Eichberger, B. Blank, U. Rau, L. H. Mascaro and et al., "Effects of Thermochemical Treatment

on CuSbS2 Photovoltaic Absorber Quality and Solar Cell Reproducibility," *The Journal of Physical Chemistry C,* vol. 120, p. 18377-18385, 8 2016.

[13] H. Stange, S. Brunken, H. Hempel, H. Rodriguez-Alvarez, N. Schäer, D. Greiner, A. Scheu, J. Lauche, C. A. Kaufmann, T. Unold and et al., "Effect of Na presence during CuInSe2 growth on stacking fault annihilation and electronic properties," *Applied Physics Letters,* vol. 107, p. 152103, 10 2015.

[14] T. Unold, H. Hempel, C. Strothkamper, C. A. Kaufmann, R. Eichberger and A. Bartelt, "Charge carrier mobilities and dynamics in thin film compound semiconductor materials from transient Thz absorption," *2014 IEEE 40th Photovoltaic Specialist Conference (PVSC),* 6 2014.

[15] C. J. Hages, A. Redinger, S. Levcenko, H. Hempel, M. J. Koeper, R. Agrawal, D. Greiner, C. A. Kaufmann and T. Unold, "Identifying the Real Minority Carrier Lifetime in Nonideal Semiconductors: A Case Study of Kesterite Materials," *Advanced Energy Materials,* p. 1700167, 2017.

[16] H. Hempel, G. Dennler, S. Müller, G. Larramona, R. Eichberger and T. Unold, "Charge carrier dynamics in Cu 2 ZnSn (S/Se) 4 thin film solar cells measured by time resolved terahertz and microwave spectroscopy," in *Infrared, Millimeter, and Terahertz waves (IRMMW-THz), 2016 41st International Conference on*, 2016.

[17] A. W. Welch, L. L. Baranowski, H. Peng, H. Hempel, R. Eichberger, T. Unold, S. Lany, C. Wolden and A. Zakutayev, "Trade-Offs in Thin Film Solar Cells with Layered Chalcostibite Photovoltaic Absorbers," *Advanced Energy Materials,* vol. 7, p. 1601935, 1 2017.

[18] S. Li, M. A. Lloyd, H. Hempel, C. J. Hages, J. A. Márquez, T. Unold, R. Eichberger, B. E. McCandless and J. B. Baxter, "Relating Carrier Dynamics and Photovoltaic Device Performance of Single-Crystalline Cu2ZnSnSe4," *Physical Review Applied,* vol. 11, p. 034005, 3 2019.

[19] M. A. Green, Y. Hishikawa, E. D. Dunlop, D. H. Levi, J. Hohl-Ebinger and A. W. Y. Ho-Baillie, "Solar cell efficiency tables (version 52)," *Progress in Photovoltaics: Research and Applications,* vol. 26, pp. 427-436, 6 2018.

[20] B. V. Emmanuel Rosencher, Optoelectronics, Cambridge University Press, 2011.

[21] S. M. Sze and K. K. Ng, Physics of semiconductor devices, John wiley & sons, 2006.

[22] W. Shockley and W. T. Read Jr, "Statistics of the recombinations of holes and electrons," *Physical review,* vol. 87, p. 835, 1952.

[23] R. A. Street, Hydrogenated amorphous silicon, Cambridge University Press, 2005.

[24] C. Jacoboni, Theory of electron transport in semiconductors: a pathway from elementary physics to nonequilibrium Green functions, vol. 165, Springer Science & Business Media, 2010.

[25] J. Lloyd-Hughes and T.-I. Jeon, "A Review of the Terahertz Conductivity of Bulk and Nano-Materials," *J Infrared Milli Terahz Waves,* vol. 33, pp. 871-925, 5 2012.

[26] R. Ulbricht, E. Hendry, J. Shan, T. F. Heinz and M. Bonn, "Carrier dynamics in semiconductors studied with time-resolved terahertz spectroscopy," *Rev. Mod. Phys.,* vol. 83, pp. 543-586, 6 2011.

[27] H. Nemec, P. Kuzel and V. Sundström, "Charge transport in nanostructured materials for solar energy conversion studied by time-resolved terahertz spectroscopy," *Journal of Photochemistry and Photobiology A: Chemistry,* vol. 215, pp. 123-139, 9 2010.

[28] J. C. Dyre, "The random free-energy barrier model for ac conduction in disordered solids," *Journal of Applied Physics,* vol. 64, pp. 2456-2468, 1988.

[29] J. C. Dyre and T. B. Schröder, "Universality of ac conduction in disordered solids," *Rev. Mod. Phys.,* vol. 72, pp. 873-892, 7 2000.

[30] H. Nemec, P. Kuzel and V. Sundström, "Far-infrared response of free charge carriers localized in semiconductor nanoparticles," *Phys. Rev. B,* vol. 79, 3 2009.

[31] N. Smith, "Classical generalization of the Drude formula for the optical conductivity," *Physical Review B,* vol. 64, p. 155106, 9 2001.

[32] H.-K. Nienhuys and V. Sundstrol̀ˆm, "Influence of plasmons on terahertz conductivity measurements," *Applied Physics Letters,* vol. 87, p. 012101, 2005.

[33] U. W. Peter Würfel, Physics of Solar Cells, Wiley VCH Verlag GmbH, 2016.

[34] W. Shockley and H. J. Queisser, "Detailed Balance Limit of Efficiency of p-n Junction Solar Cells," *Journal of Applied Physics,* vol. 32, pp. 510-519, 3 1961.

[35] U. Rau, B. Blank, T. C. Müller and T. Kirchartz, "Efficiency Potential of Photovoltaic Materials and Devices Unveiled by Detailed-Balance Analysis," *Physical Review Applied,* vol. 7, p. 044016, 4 2017.

[36] A. S. T. M. G173-03, "Tables for Reference Solar Spectral Irradiances: Direct Normal and Hemispherical on 37 Tilted Surface," 2012.

[37] M. A. Green, Y. Hishikawa, E. D. Dunlop, D. H. Levi, J. Hohl-Ebinger and A. W. Y. Ho-Baillie, "Solar cell efficiency tables (version 51)," *Progress in Photovoltaics,* vol. 26, pp. 3-12, 2018.

[38] P. Wurfel, "The chemical potential of radiation," *Journal of Physics C: Solid State Physics,* vol. 15, p. 3967, 1982.

[39] M. Burgelman, P. Nollet and S. Degrave, "Modelling polycrystalline semiconductor solar cells," *Thin Solid Films,* vol. 361, pp. 527-532, 2 2000.

[40] R. E. Brandt, V. Stevanovic, D. S. Ginley and T. Buonassisi, "Identifying defect-tolerant semiconductors with high minority-carrier lifetimes: beyond hybrid lead halide perovskites," *MRS Communications,* vol. 5, pp. 265-275, 5 2015.

[41] C. J. Hages, N. J. Carter and R. Agrawal, "Generalized quantum efficiency analysis for non-ideal solar cells: Case of Cu2ZnSnSe4," *Journal of Applied Physics,* vol. 119, p. 014505, 1 2016.

[42] W. J. Yang, Z. Q. Ma, X. Tang, C. B. Feng, W. G. Zhao and P. P. Shi, "Internal quantum efficiency for solar cells," *Solar Energy,* vol. 82, pp. 106-110, 2 2008.

[43] J. H. Reynolds and A. Meulenberg, "Measurement of diffusion length in solar cells," *Journal of Applied Physics,* vol. 45, pp. 2582-2592, 6 1974.

[44] P. U. Jepsen, D. G. Cooke and M. Koch, "Terahertz spectroscopy and imaging - Modern techniques and applications," *Laser & Photon. Rev.,* vol. 5, pp. 124-166, 10 2010.

[45] H. J. Joyce, J. L. Boland, C. L. Davies, S. A. Baig and M. B. Johnston, "A review of the electrical properties of semiconductor nanowires: insights gained from terahertz conductivity spectroscopy," *Semiconductor Science and Technology,* vol. 31, p. 103003, 9 2016.

[46] C. A. Schmuttenmaer, "Exploring Dynamics in the Far-Infrared with Terahertz Spectroscopy," *Chemical Reviews,* vol. 104, pp. 1759-1780, 4 2004.

[47] R. A. Kaindl, D. Hägele, M. A. Carnahan and D. S. Chemla, "Transient terahertz spectroscopy of excitons and unbound carriers in quasi-two-dimensional electron-hole gases," *Physical Review B,* vol. 79, p. 045320, 1 2009.

[48] J. F. OHara, W. Withayachumnankul and I. Al-Naib, "A Review on Thin-film Sensing with Terahertz Waves," *J Infrared Milli Terahz Waves,* vol. 33, pp. 245-291, 3 2012.

[49] T. Seifert, S. Jaiswal, U. Martens, J. Hannegan, L. Braun, P. Maldonado, F. Freimuth, A. Kronenberg, J. Henrizi, I. Radu, E. Beaurepaire, Y. Mokrousov, P. M. Oppeneer, M. Jourdan, G. Jakob, D. Turchinovich, L. M. Hayden, M. Wolf, M. Münzenberg, M. Kläui and T. Kampfrath, "Efficient metallic spintronic emitters of ultrabroadband terahertz radiation," *Nature Photonics,* vol. 10, pp. 483-488, 5 2016.

[50] F. D' Angelo, H. Nemec, S. H. Parekh, P. Kuzel, M. Bonn and D. Turchinovich, "Self-referenced ultra-broadband transient terahertz spectroscopy using air-photonics," *Optics Express,* vol. 24, p. 10157, 4 2016.

[51] D. G. Cooke, F. C. Krebs and P. U. Jepsen, "Direct Observation of Sub-100 fs Mobile Charge Generation in a Polymer-Fullerene Film," *Physical Review Letters,* vol. 108, p. 056603, 1 2012.

[52] D. G. Cooke, A. Meldrum and P. Uhd Jepsen, "Ultrabroadband terahertz conductivity of Si nanocrystal films," *Applied Physics Letters,* vol. 101, p. 211107, 2012.

[53] D. A. Valverde-Chavez, C. S. Ponseca, C. C. Stoumpos, A. Yartsev, M. G. Kanatzidis, V. Sundström and D. G. Cooke, "Intrinsic femtosecond charge generation dynamics in single crystal CH3NH3PbI3," *Energy Environ. Sci.,* vol. 8, pp. 3700-3707, 2015.

[54] K. Iwaszczuk, D. G. Cooke, M. Fujiwara, H. Hashimoto and P. U. Jepsen, "Simultaneous reference and differential waveform acquisition in time-resolved terahertz spectroscopy," *Optics Express,* vol. 17, pp. 21969-21976, 11 2009.

[55] M. C. Beard, G. M. Turner and C. A. Schmuttenmaer, "Transient photoconductivity in GaAs as measured by time-resolved terahertz spectroscopy," *Physical Review B,* vol. 62, pp. 15764-15777, Dec 2000.

[56] H. Nemec, F. Kadlec and P. Kuzel, "Methodology of an optical pump-terahertz probe experiment: An analytical frequency-domain approach," *J. Chem. Phys.,* vol. 117, p. 8454, 2002.

[57] M. B. Johnston, D. M. Whittaker, A. Corchia, A. G. Davies and E. H. Linfield, "Simulation of terahertz generation at semiconductor surfaces," *Physical Review B,* vol. 65, p. 165301, 3 2002.

[58] M. C. T. Bahaa E.A. Saleh, Fundamentals of Photonics, Wiley John + Sons, 2001.

[59] P. Kuzel, F. Kadlec and H. Nemec, "Propagation of terahertz pulses in photoexcited media: Analytical theory for layered systems," *The Journal of Chemical Physics,* vol. 127, p. 024506, 2007.

[60] D. Schneider, D. Rürup, B. Schönfelder and A. Schlachetzki, "Effective mass and energy-band parameters in InP by magnetophonon effect," *Zeitschrift für Physik B Condensed Matter,* vol. 100, pp. 33-38, 3 1996.

[61] L. M. Herz, "Charge-carrier mobilities in metal halide perovskites: fundamental mechanisms and limits," *ACS Energy Letters,* vol. 2, pp. 1539-1548, 6 2017.

[62] T. J. Savenije, A. J. Ferguson, N. Kopidakis and G. Rumbles, "Revealing the Dynamics of Charge Carriers in Polymer:Fullerene Blends Using Photoinduced Time-Resolved Microwave Conductivity," *The Journal of Physical Chemistry C,* vol. 117, pp. 24085-24103, 10 2013.

[63] M. Kunst and G. Beck, "The study of charge carrier kinetics in semiconductors by microwave conductivity measurements," *Journal of Applied Physics,* vol. 60, pp. 3558-3566, 11 1986.

[64] T. Gokmen, O. Gunawan and D. B. Mitzi, "Minority carrier diffusion length extraction in Cu2ZnSn(Se,S)4 solar cells," *Journal of Applied Physics,* vol. 114, no. 11, p. 114511, 2013.

[65] A. C. Beer, "The Hall effect and related phenomena," *Solid-State Electronics,* vol. 9, pp. 339-351, 5 1966.

[66] G. Larramona, S. Bourdais, A. Jacob, C. Chone, T. Muto, Y. Cuccaro, B. Delatouche, C. Moisan, D. Pere and G. Dennler, "8.6% Efficient CZTSSe Solar Cells Sprayed from Water-Ethanol CZTS Colloidal Solutions," *The Journal of Physical Chemistry Letters,* vol. 5, no. 21, pp. 3763-3767, Nov 2014.

[67] G. Larramona, S. Levcenko, S. Bourdais, A. Jacob, C. Chone, B. Delatouche, C. Moisan, J. Just, T. Unold and G. Dennler, "Fine-Tuning the Sn Content in CZTSSe Thin Films to Achieve 10.8% Solar Cell Efficiency from Spray-Deposited Water-Ethanol-Based Colloidal Inks," *Adv. Energy Mater.,* vol. 5, no. 24, Oct 2015.

[68] I. L. Repins, J. V. Li, A. Kanevce, C. L. Perkins, K. X. Steirer, J. Pankow, G. Teeter, D. Kuciauskas, C. Beall, C. Dehart and e. al., "Effects of deposition termination on Cu2ZnSnSe4 device characteristics," *Thin Solid Films,* vol. 582, pp. 184-187, May 2015.

[69] T. Gokmen, O. Gunawan, T. K. Todorov and D. B. Mitzi, "Band tailing and efficiency limitation in kesterite solar cells," *Appl. Phys. Lett.,* vol. 103, p. 103506, 2013.

[70] S. Bourdais, C. Chone, B. Delatouche, A. Jacob, G. Larramona, C. Moisan, A. Lafond, F. Donatini, G. Rey, S. Siebentritt and others, "Is the Cu/Zn disorder the main culprit for the voltage deficit in kesterite solar cells?," *Advanced Energy Materials,* vol. 6, 2016.

[71] O. Gunawan, T. Gokmen and D. B. Mitzi, "Suns-VOC characteristics of high performance kesterite solar cells," *Journal of Applied Physics,* vol. 116, p. 084504, aug 2014.

[72] J. K. Katahara and H. W. Hillhouse, "Quasi-Fermi level splitting and sub-bandgap absorptivity from semiconductor photoluminescence," *Journal of Applied Physics,* vol. 116, p. 173504, 11 2014.

[73] G. Rey, G. Larramona, S. Bourdais, C. Chone, B. Delatouche, A. Jacob, G. Dennler and S. Siebentritt, "On the origin of band-tails in kesterite," *Solar Energy Materials and Solar Cells,* vol. 179, pp. 142-151, 6 2017.

[74] S. K. Wallace, D. B. Mitzi and A. Walsh, "The Steady Rise of Kesterite Solar Cells," *ACS Energy Letters,* vol. 2, pp. 776-779, 2017.

[75] J. J. S. Scragg, J. K. Larsen, M. Kumar, C. Persson, J. Sendler, S. Siebentritt and C. Platzer Björkman, "Cu-Zn disorder and band gap fluctuations in Cu 2 ZnSn(S,Se)4: Theoretical and experimental investigations," *physica status solidi (b),* vol. 253, no. 2, pp. 247-254, Sep 2015.

[76] S. John, C. Soukoulis, M. H. Cohen and E. N. Economou, "Theory of electron band tails and the Urbach optical-absorption edge," *Physical review letters,* vol. 57, p. 1777, 12 1986.

[77] C. M. Soukoulis and E. N. Economou, "Electronic localization in disordered systems," *Waves in Random Media,* vol. 9, pp. 255-270, 4 1999.

[78] S. Chen, A. Walsh, X.-G. Gong and S.-H. Wei, "Classification of lattice defects in the kesterite Cu2ZnSnS4 and Cu2ZnSnSe4 earth-abundant solar cell absorbers," *Advanced materials,* vol. 25, pp. 1522-1539, 2 2013.

[79] S. Levcenko, J. Just, A. Redinger, G. Larramona, S. Bourdais, G. Dennler, A. Jacob and T. Unold, "Deep Defects in Cu2ZnSn(S,Se)4 Solar Cells with Varying Se Content," *Physical Review Applied,* vol. 5, no. 2, Feb 2016.

[80] M. Guc, R. Caballero, K. Lisunov, N. Lopez, E. Arushanov, J. Merino and M. Leon, "Disorder and variable-range hopping conductivity in Cu2ZnSnS4 thin films prepared by flash evaporation and post-thermal treatment," *Journal of Alloys and Compounds,* vol. 596, pp. 140-144, May 2014.

[81] A. Nagaoka, H. Miyake, T. Taniyama, K. Kakimoto and K. Yoshino, "Correlation between intrinsic defects and electrical properties in the high-quality Cu2ZnSnS4 single crystal," *Appl. Phys. Lett.,* vol. 103, no. 11, p. 112107, 2013.

[82] D. P. Halliday, R. Claridge, M. C. J. Goodman, B. G. Mendis, K. Durose and J. D. Major, "Luminescence of Cu2ZnSnS4 polycrystals described by the fluctuating potential model," *Journal of Applied Physics,* vol. 113, no. 22, p. 223503, 2013.

[83] J. P. Leitao, N. M. Santos, P. A. Fernandes, P. M. P. Salome, F. da Cunha and A., J. C. Gonzalez, G. M. Ribeiro and F. M. Matinaga, "Photoluminescence and electrical study of fluctuating potentials in Cu_2ZnSnS_4-based thin films," *Phys. Rev. B,* vol. 84, pp. 1-8, Jul 2011.

[84] U. Rau and J. H. Werner, "Radiative efficiency limits of solar cells with lateral band-gap fluctuations," *Applied Physics Letters,* vol. 84, pp. 3735-3737, 5 2004.

[85] L. Quang Phuong, M. Okano, Y. Yamada, A. Nagaoka, K. Yoshino and Y. Kanemitsu, "Photocarrier localization and recombination dynamics in Cu2ZnSnS4 single crystals," *Appl. Phys. Lett.,* vol. 103, no. 19, p. 191902, 2013.

[86] J. E. Moore, C. J. Hages, R. Agrawal, M. S. Lundstrom and J. L. Gray, "The importance of band tail recombination on current collection and open-circuit voltage in CZTSSe solar cells," *Applied Physics Letters,* vol. 109, p. 021102, 7 2016.

[87] J. Tauc, "Optical Properties of Solids ed F Abeles," *North-Holland Publ. Co,* vol. 277, p. 153, 1972.

[88] S. Siebentritt, G. Rey, A. Finger, D. Regesch, J. Sendler, T. P. Weiss and T. Bertram, "What is the bandgap of kesterite?," *Solar Energy Materials and Solar Cells,* vol. 158, pp. 126-129, 12 2016.

[89] F. Urbach, "The long-wavelength edge of photographic sensitivity and of the electronic absorption of solids," *Physical Review,* vol. 92, p. 1324, 12 1953.

[90] Y. Yang, D. P. Ostrowski, R. M. France, K. Zhu, J. van de Lagemaat, J. M. Luther and M. C. Beard, "Observation of a hot-phonon bottleneck in lead-iodide perovskites," *Nature Photon,* Oct 2015.

[91] E. Burstein, "Anomalous optical absorption limit in InSb," *Physical Review,* vol. 93, p. 632, 1954.

[92] A. Esser, H. Heesel, H. Kurz, C. Wang, G. N. Parsons and G. Lucovsky, "Transport properties of optically generated free carriers in hydrogenated amorphous silicon in the femtosecond time regime," *Physical Review B,* vol. 47, p. 3593, 1993.

[93] J. A. Moon, J. Tauc, J.-K. Lee, E. A. Schiff, P. Wickboldt and W. Paul, "Femtosecond photomodulation spectroscopy of a-Si: H and a-Si: Ge: H alloys in the midinfrared," *Physical Review B,* vol. 50, p. 10608, oct 1994.

[94] T. Elsaesser, J. Shah, L. Rota and P. Lugli, "Initial thermalization of photoexcited carriers in GaAs studied by femtosecond luminescence spectroscopy," *Physical review letters,* vol. 66, p. 1757, 1991.

[95] R. W. Schoenlein, W. Z. Lin, E. P. Ippen and J. G. Fujimoto, "Femtosecond hot-carrier energy relaxation in GaAs," *Applied physics letters,* vol. 51, pp. 1442-1444, 1987.

[96] J. L. Oudar, D. Hulin, A. Migus, A. Antonetti and F. Alexandre, "Subpicosecond spectral hole burning due to nonthermalized photoexcited carriers in GaAs," *Physical review letters,* vol. 55, p. 2074, 1985.

[97] J. Orenstein, M. A. Kastner and V. Vaninov, "Transient photoconductivity and photo-induced optical absorption in amorphous semiconductors," *Philosophical Magazine B,* vol. 46, pp. 23-62, jul 1982.

[98] C. Strothkämper, A. Bartelt, R. Eichberger, C. Kaufmann and T. Unold, "Microscopic mobilities and cooling dynamics of photoexcited carriers in polycrystalline CuInSe2," *Phys. Rev. B,* vol. 89, pp. 115204-1 115204-4, 3 2014.

[99] S. G. Choi, H. Y. Zhao, C. Persson, C. L. Perkins, A. L. Donohue, B. To, A. G. Norman, J. Li and I. L. Repins, "Dielectric function spectra and critical-point energies of Cu2ZnSnSe4 from 0.5 to 9.0 eV," *Journal of Applied Physics,* vol. 111, p. 033506, 2012.

[100] Y. Yang, Y. Yan, M. Yang, S. Choi, K. Zhu, J. M. Luther and M. C. Beard, "Low surface recombination velocity in solution-grown CH3NH3PbBr3 perovskite single crystal," *Nat Comms,* vol. 6, p. 7961, 8 2015.

[101] R. K. Ahrenkiel and S. W. Johnston, "An optical technique for measuring surface recombination velocity," *Solar Energy Materials and Solar Cells,* vol. 93, pp. 645-649, 2009.

[102] W. Van Roosbroeck, "Injected Current Carrier Transport in a Semi-Infinite Semiconductor and the Determination of Lifetimes and Surface Recombination Velocities," *Journal of Applied Physics,* vol. 26, pp. 380-391, 4 1955.

[103] G. W. Guglietta, K. R. Choudhury, J. V. Caspar and J. B. Baxter, "Employing time-resolved terahertz spectroscopy to analyze carrier dynamics in thin-film Cu2ZnSn(S,Se)4 absorber layers," *Appl. Phys. Lett.,* vol. 104, no. 25, p. 253901, Jun 2014.

[104] A. Redinger, M. Mousel, R. Djemour, L. Gütay, N. Valle and S. Siebentritt, "Cu2ZnSnSe4thin film solar cells produced via co-evaporation and annealing including a SnSe2capping layer," *Progress in Photovoltaics: Research and Applications,* vol. 22, pp. 51-57, 2 2013.

[105] A. Redinger and T. Unold, "High surface recombination velocity limits Quasi-Fermi level splitting in kesterite absorbers," *Scientific reports,* vol. 8, p. 1874, 1 2018.

[106] K. Shimakawa, T. Itoh, H. Naito and S. O. Kasap, "The origin of non-Drude terahertz conductivity in nanomaterials," *Appl. Phys. Lett.,* vol. 100, p. 132102, 2012.

[107] J. Dong and D. A. Drabold, "Atomistic structure of band-tail states in amorphous silicon," *Physical review letters,* vol. 80, p. 1928, 3 1998.

[108] F. Huth, "Hall Coefficient and Impurity Band Mobility in Cd-Doped GaAs," *physica status solidi (b),* vol. 34, pp. 87-90, 1969.

[109] C. Persson, "Electronic and optical properties of Cu 2 ZnSnS 4 and Cu 2 ZnSnSe 4," *Journal of Applied Physics,* vol. 107, p. 053710, 3 2010.

[110] S. Schorr, "The crystal structure of kesterite type compounds: A neutron and X-ray diffraction study," *Solar Energy Materials and Solar Cells,* vol. 95, no. 6, pp. 1482-1488, Jun 2011.

[111] G. Rey, A. Redinger, J. Sendler, T. P. Weiss, M. Thevenin, M. Guennou, B. E. Adib and S. Siebentritt, "The band gap of Cu2ZnSnSe4: Effect of order-disorder," *Applied Physics Letters,* vol. 105, p. 112106, 9 2014.

[112] T. Schwarz, O. Cojocaru-Mirédin, P. Choi, M. Mousel, A. Redinger, S. Siebentritt and D. Raabe, "Atom probe study of Cu2ZnSnSe4 thin-films prepared by co-evaporation and post-deposition annealing," *Applied Physics Letters,* vol. 102, p. 042101, 1 2013.

[113] S. Schorr, H.-J. Hoebler and M. Tovar, "A neutron diffraction study of the stannite-kesterite solid solution series," *European Journal of Mineralogy,* vol. 19, pp. 65-73, 2 2007.

[114] J. Marquez-Prieto, Y. Ren, R. W. Miles, N. Pearsall and I. Forbes, "The influence of precursor Cu content and two-stage processing conditions on the microstructure of Cu2ZnSnSe4," *Thin Solid Films,* vol. 582, pp. 220-223, 5 2015.

[115] G. D. Cody, T. Tiedje, B. Abeles, B. Brooks and Y. Goldstein, "Disorder and the optical-absorption edge of hydrogenated amorphous silicon," *Physical Review Letters,* vol. 47, p. 1480, 10 1981.

[116] T. Gershon, K. Sardashti, O. Gunawan, R. Mankad, S. Singh, Y. S. Lee, J. A. Ott, A. Kummel and R. Haight, "Photovoltaic Device with over 5 % Efficiency Based on an n-Type Ag2ZnSnSe4 Absorber," *Advanced Energy Materials,* vol. 6, p. 1601182, 8 2016.

9.2 Danksagung / Acknowledgement

Als erstes möchte ich meiner Familie danken, ohne die diese Arbeit nicht möglich gewesen wäre. Im besonderen Claudia, welche mir oft den Rücken freigehalten hat und die Verantwortung für unsere kleine Familie übernommen hat, als ich am NREL war. Ich möchte meiner Mutter danken, die mich zur Eigenständigkeit erzogen hat und dazu meine eigenen Ideen zu folgen. Auch Elke bin ich dankbar, für den freien Montagabend und die regelmäßige Kinderbetreuung.

Im Besonderen danke ich auch Thomas Unold, meinem Gruppenleiter, für seine Unterstützung, seinen Rat und sein Wissen im Bereich der Photovoltaik und Spektroskopie, das er mit mir geteilt hat. Er hat mir nicht nur die anfänglichen Fragestellungen dieser Doktorarbeit aufgezeigt, sondern ich konnte unter ihm auch eigene Ideen entwickeln. Ich danke ihm daher für die Freiheiten die er mir gewährt hat, wenn ich sie wollte, und für die Unterstützung die er mir zukommen lassen hat, wenn ich sie brauchte.

Außerdem möchte ich Klaus Lips und Tobias Kampfrath danken, die mir mit Ratschlägen zur Seite standen und die sich bereit erklärt haben, diese Arbeit zu begutachten.

Meinen Kollegen: Jose Marquez Prieto, Alex Redinger, Charles Hages, Pascal Becker, Klaus Schwarzburg, Matin Kärgell und Sergej Levcenco danke ich für die vielen anregenden Diskussionen und erhellenden Gespräche.

Außerdem danke ich Christian Strothkämper, Phillip Sippel, Sönke Müller und Rainer Eichberger für ihre Unterstützung und Einführung am Terahertz-Aufbau. Ebenso Steffen Kretzschmar, Alex Redinger und Jose Marquez Prieto für den exzellenten Q-PL-Aufbau und die von ihnen durchgeführten Messungen.

Für finanzielle Unterstützung bedanke ich mich bei der MatSEC Doktoranden-Schule und im Besonderen bei Susann Schorr und Gabi Lampert, als auch bei dem HNSEI-Projekt.

Meinen Töchtern, Tabea und Flora, bin ich dankbar für die Ausgleich am Feierabend den sie mir verschafft haben. Zu diesem haben im selben Maße meine Impro-Gruppe und mein Mitbewohner in den USA beigetragen.

Danke euch allen.

9.3 Abstract

Novel photovoltaic materials have to be developed at an increasing pace to keep up with the progress of established solar cell technologies and to fit into the limited funding periods of science. Such a speed-up can be realized by the characterization of photovoltaic materials with time-resolved terahertz spectroscopy (TRTS) which can reveal the limits and losses of photovoltaic materials and thereby guides their further development.

First, ***TRTS was advanced and validated*** in this work for the characterization of charge carrier lifetime and mobility in photovoltaic materials. Publication [3] shows that TRTS can measure charge carrier mobilities in thin films on metal substrates, which are the prevalent architecture of photovoltaic thin-film samples. Further, publication [5] shows that the individual mobilities of electrons and holes are derived by combining TRTS transients and the usually derived TRTS sum mobility. Such distinction is especially important for photovoltaics because the charge transport in solar cells is usually limited by the minority charge carriers.

Second, an ***in-depth characterization of a $Cu_2ZnSnSe_4$*** thin film was conducted. This thin film was deposited during my stay at the national renewable energy laboratory (NREL) at similar conditions as their record $Cu_2ZnSnSe_4$ solar cell. The charge carrier dynamics, including cooling, trapping, localization, recombination, and transport, were probed and integrated into one narrative. The recombination of the photo-excited charge carriers is characterized by a bulk charge carrier lifetime of 4.4 ns and by a surface recombination velocity of $6*10^4$ cm/s [5]. The transport is described by an electron mobility of 127 cm^2/Vs ±25 % and a hole mobility of 7 cm^2/Vs ±50 % [5]. These mobilities are limited by localization on a length scale of ∼11nm and correspond to the transport within the ∼1 µm sized grains the polycrystalline $Cu_2ZnSnSe_4$ [4]. However, the mobility in $Cu_2ZnSnSe_4$ is relatively high in comparison to 15 other photovoltaic materials that I probed [7-17]. The Cu-Zn disorder has no impact on mobility and lifetime in $Cu_2ZnSnSe_4$ [6].

Third, the relatively low **efficiency of the $Cu_2ZnSnSe_4$ solar cell** of 7.2 % compared to its Shockley-Queisser limit of 31.4 % and to competing photovoltaic materials, was mostly attributed to charge carrier recombination, which reduces the voltage by ∼239 meV and the current by ∼8.5 mA/cm^2. Band tails, which are often regarded as the main limitation, affect the performance only to a minor degree. We found a tenfold reduction of the mobility and a loss in the voltage by ∼105 meV. An impact on the lifetime and recombination could not be proven. The charge carrier mobility, absorption and bandgap energy of $Cu_2ZnSnSe_4$ are in principle suited for high efficiencies.

9.4 Kurzzusammenfassung

Die Entwicklung neuer Materialien für die Photovoltaik bedurfte in der Vergangenheit mehrerer Jahrzehnte. Um jedoch mit dem Fortschritt der etablierten Solarzellentechnologien mitzuhalten und die Entwicklung innerhalb der kurzen Finanzierungszeiträume in der Wissenschaft umzusetzen, muss die Forschungszeit deutlich verkürzt werden. Dieses Ziel kann durch zeitaufgelöste Terahertzspektroskopie (TRTS) realisiert werden, welche die Verluste in photovoltaischen Materialien aufzeigt und damit deren Weiterentwicklung steuern kann.

Zuerst werden in dieser Arbeit die ***Weiterentwicklung von TRTS*** und deren Anpassung auf die Anforderungen der Photovoltaik beschrieben. In der Veröffentlichung [3] wurde gezeigt, dass TRTS die Ladungsträgermobiltäten und Lebenszeiten in Dünnschichten auf Metallsubstraten messen kann, was der Standardaufbau einer Dünnschicht-Solarzelle ist. Des Weiteren wird in Veröffentlichung [5] gezeigt, dass die Elektronmobilität und die Lochmobilität separat mit TRTS gemessen werden können, wenn die Summe der beiden Mobilitäten, welche standardmäßig mit TRTS gemessen wird, mit einer Analyse der TRTS-Transienten kombiniert wird.

Dann werden die ***Ladungsträgerdynamiken in einer $Cu_2ZnSnSe_4$-Dünnschicht*** im Detail untersucht, welche während meines Aufenthaltes am National Renewable Energy Laboratory (NREL) in den USA hergestellt wurde und welche deren Weltrekord-$Cu_2ZnSnSe_4$-Solarzelle entspricht. Dabei werden die Ladungsträgerabkühlung, deren Trapping, Lokalisation, Rekombination und Transport untersucht und in ein Gesamtbild integriert. Die Rekombination der photoinduzierten Ladungsträger ist charakterisiert von einer Lebenszeit von 4.4 ns und von einer Oberflächenrekombinationsgeschwindigkeit von $6*10^4$ cm/s [5]. Der Ladungsträgertransort wird von einer Elektronmobilität von 127 cm^2/Vs ±25 %, und einer Lochmobilität von $7cm^2/Vs$ ±50 %, beherrscht. Diese Mobilitäten sind durch Ladungsträgerlokalisation auf einem Bereich von ca. 11 nm begrenzt und entsprechen dem Transport innerhalb der ca. 1 µm großen Körner in dem polykristallinen $Cu_2ZnSnSe_4$ [4]. Im Vergleich zu 15 weiteren photovoltaischen Materialien, welche ich als Ko-autor untersucht habe [7-17], ist die Mobilität in $Cu_2ZnSnSe_4$ jedoch relativ hoch.

Die ***Effizienz der $Cu_2ZnSnSe_4$ Solarzelle*** von 7.2 % ist relativ niedrig im Vergleich zu ihrem „Shockley-Queisser-Limit“ und zu anderen weiter entwickelten Materialien. Diese Unterlegenheit wird zum Großteil durch Ladungsträgerrekombination hervorgerufen, welche die Spannung um ca. 239 meV und den Strom um 8.5 mA/cm^2 reduziert. Bandtails, welche oft als hauptsächliche Limitation aufgeführt werden, tragen nur zu einem geringeren Verlust in der Spannung von ca. ∼105 meV bei und reduzieren die Ladungsträgermobilität auf ein Zehntel. Einen Einfluss auf die Ladungsträgerrekombination konnte jedoch nicht zweifelsfrei nachgewiesen werden. Die Ladungsträgermobilität, die Absorption und die Bandlückenenergie von $Cu_2ZnSnSe_4$ sind für Solarzellen bestens geeignet.

9.5 Selbstständigkeitserklärung

Hiermit versichere ich alle Hilfsmittel und Hilfen angegeben zu haben und auf dieser Grundlage die Arbeit selbstständig verfasst zu haben.

Des Weiteren versichere ich, dass die Arbeit nicht schon einmal in einem früheren Promotionsverfahren angenommen oder als ungenügend beurteilt worden ist.

_____

Hannes Hempel

9.6 Publications

Parts of this work have been published in peer-reviewed journals. In the following 4 first author and 11 co-author publications are listed. My contributions to the first author publications will be stated and preprints of these first author publications are attached at the end.

9.6.1 List of Publications

First Author:

1 H. Hempel, T. Unold and R. Eichberger, "Measurement of charge carrier mobilities in thin films on metal substrates by reflection time resolved terahertz spectroscopy," *Optics Express,* vol. 25, p. 17227, 2017.

2 H. Hempel, A. Redinger, I. Repins, C. Moisan, G. Larramona, G. Dennler, M. Handwerg, S. F. Fischer, R. Eichberger and T. Unold, "Intragrain charge transport in kesterite thin films—Limits arising from carrier localization," *Journal of Applied Physics,* vol. 120, p. 175302, 11 2016.

3 H. Hempel, C. J. Hages, R. Eichberger, I. Repins und T. Unold, „Minority and Majority Charge Carrier Mobility in Cu2ZnSnSe4 revealed by Terahertz Spectroscopy," *Scientific Reports*, vol. 8, p. 14476, 9 2018

4 H. Hempel, R. Eichberger, I. Repins and T. Unold, "The effect of Cu-Zn disorder on charge carrier mobility and lifetime in Cu2ZnSnSe4," *Thin Solid Films,* vol. 666, pp. 40, 11 2018.

Co-Author:

6 L. L. Baranowski, K. McLaughlin, P. Zawadzki, S. Lany, A. Norman, H. Hempel, R. Eichberger, T. Unold, E. S. Toberer and A. Zakutayev, "Effects of Disorder on Carrier Transport in Cu2SnS 3," *Physical Review Applied,* vol. 4, 10 2015.

6 J. A. Marquez Prieto, S. Levcenko, J. Just, H. Hempel, I. Forbes, N. M. Pearsall and T. Unold, "Earth abundant thin film solar cells from co-evaporated Cu2SnS3 absorber layers," *Journal of Alloys and Compounds,* vol. 689, pp. 182-186, 12 2016.

8 F. Staub, H. Hempel, J.-C. Hebig, J. Mock, U. W. Paetzold, U. Rau, T. Unold and T. Kirchartz, "Beyond bulk lifetimes: Insights into lead halide perovskite films from time-resolved photoluminescence," *Physical Review Applied,* vol. 6, p. 044017, 10 2016.

9 M. Ziwritsch, S. Müller, H. Hempel, T. Unold, F. F. Abdi, R. Krol, D. Friedrich and R. Eichberger, "Direct Time-Resolved Observation of Carrier Trapping and Polaron Conductivity in BiVO4," *{ACS} Energy Letters,* vol. 1, pp. 888-894, 11 2016.

10 J.-W. Jang, D. Friedrich, S. Müller, M. Lamers, H. Hempel, S. Lardhi, Z. Cao, M. Harb, L. Cavallo, R. Heller and others, "Enhancing Charge Carrier Lifetime in Metal Oxide Photoelectrodes through Mild Hydrogen Treatment," *Advanced Energy Materials,* vol. 7, p. 1701536, 8 2017.

11 F. W. Souza Lucas, A. W. Welch, L. L. Baranowski, P. C. Dippo, H. Hempel, T. Unold, R. Eichberger, B. Blank, U. Rau, L. H. Mascaro and et al., "Effects of Thermochemical Treatment on CuSbS2 Photovoltaic Absorber Quality and Solar Cell Reproducibility," *The Journal of Physical Chemistry C,* vol. 120, p. 18377?18385, 8 2016.

12 H. Stange, S. Brunken, H. Hempel, H. Rodriguez-Alvarez, N. Schäer, D. Greiner, A. Scheu, J. Lauche, C. A. Kaufmann, T. Unold and et al., "Effect of Na presence during CuInSe2 growth on stacking fault annihilation and electronic properties," *Applied Physics Letters,* vol. 107, p. 152103, 10 2015.

13 T. Unold, H. Hempel, C. Strothkamper, C. A. Kaufmann, R. Eichberger and A. Bartelt, "Charge carrier mobilities and dynamics in thin film compound semiconductor materials from transient Thz absorption," *2014 IEEE 40th Photovoltaic Specialist Conference (PVSC),* 6 2014.

14 C. J. Hages, A. Redinger, S. Levcenko, H. Hempel, M. J. Koeper, R. Agrawal, D. Greiner, C. A. Kaufmann and T. Unold, "Identifying the Real Minority Carrier Lifetime in Nonideal Semiconductors: A Case Study of Kesterite Materials," *Advanced Energy Materials,* p. 1700167, 2017.

15 A. W. Welch, L. L. Baranowski, H. Peng, H. Hempel, R. Eichberger, T. Unold, S. Lany, C. Wolden and A. Zakutayev, "Trade-Offs in Thin Film Solar Cells with Layered Chalcostibite Photovoltaic Absorbers," *Advanced Energy Materials,* vol. 7, p. 1601935, 1 2017.

16 S. Li, M. A. Lloyd, H. Hempel, C. J. Hages, J. A. Márquez, T. Unold, R. Eichberger, B. E. McCandless and J. B. Baxter, "Relating Carrier Dynamics and Photovoltaic Device Performance of Single-Crystalline Cu2ZnSnSe4," *Physical Review Applied,* vol. 11, p. 034005, 3 2019.

9.6.2 Author Contributions

"Intra-grain Charge Transport in Kesterite Thin Films - Limits Arising from Carrier Localization" was published in the Journal of Applied Physics with the DOI: 10.1063/1.4965868.

Hannes Hempel conducted the terahertz measurements, wrote the initial draft and implemented the revisions. Alex Redinger, Ingrid Repins and Camille Moisan deposited the samples. Gerardo Larramona and Gilles Dennler supervised Camille Moisan. Martin Handwerg conducted the Hall measurements and was supervised by Saskia F. Fischer. Rainer Eichberger provided the terahertz laboratory. Thomas Unold supervised Hannes Hempel, conceived the idea and communicated with the editors and reviewers. Thomas Unold, Alex Redinger and Rainer Eichberger contribute by discussing the results and commenting on the draft.

"Measurement of charge carrier mobilities in thin films on metal substrates by reflection time resolved terahertz spectroscopy" was published in Optics Express with the DOI: 10.1364/oe.25.017227.

Hannes Hempel set up the reflection mode, conducted the terahertz measurements, modeled the data, wrote the initial draft and implemented the revisions. Thomas Unold conceived the idea, supervised Hannes Hempel and communicated with the editors and reviewers. Rainer Eichberger provided the terahertz laboratory. All authors contributed to discussing the results and commenting on the draft.

"The Effect of Cu-Zn Disorder on Charge Carrier Mobility and Lifetime in $Cu_2ZnSnSe_4$" was published in Thin Solid Films with the DOI: 10.1016/j.tsf.2018.09.027

Hannes Hempel conceived the idea, conducted the terahertz measurements and the sample treatments, wrote the initial draft, implemented the revisions and communicated with the editors and reviewers. Rainer Eichberger provided the terahertz laboratory. Ingrid Repins provided the sample. Thomas Unold supervised Hannes Hempel. All authors contributed to discussing the results and revising the draft.

"Minority and Majority Charge Carrier Mobility in $Cu_2ZnSnSe_4$ revealed by Terahertz Spectroscopy" was published in Scientific Reports with the DOI: 10.1038/s41598-018-32695-6.

Hannes Hempel conceived the idea, conducted the experiment and modeled the data. Ingrid Repins provided the sample. All authors discussed the results and contributed to writing to the paper.